Departamento de Ingeniería Química y Ambiental
Escuela Técnica Superior de Ingeniería
Universidad de Sevilla

X-ray Computed Tomography as a method of cryoprotectant concentration measurement and ice detection. Application to organ cryopreservation

PhD Thesis

Ariadna Corral Sousa

Director: Ramón Risco Delgado
Tutor: Carlos Leiva Fernández

Sevilla, enero 2014

Index

Acknowledgements

To my PhD supervisor Ramón Risco, for introducing me such an exciting world as Cryobiology. For showing me different ways of working and to deal with many different situations.

To my PhD advisor Carlos Leiva and to the Chemical and Enviromental Engineering Department, for trusting me.

To my lovely friend Antonio, because we always have thought in each other. And he just thought about me at the right moment.

To the Applied Physics Department colleagues, because I have learnt so much about Physics and they have made me feel like one among them. My special thanks to Paco, Enrique and Pedro.

To all the colleagues that have worked at the lab since I started, because all of them made a little contribution to my thesis: Javi Yuste, M.Angeles, Antonio, Montse, Laura, Jose Antonio, Javi Puyou, Aaron, Julia, Dani, Eva, María, Fadi, Antonio, Jesús, Sergio and especially to Reyes and Dr. Alberto Olmo.

To the CNA team, Dr. Cobos in the beginning, Ángel, Isabel, Dr. Laura Maza and especially to Dr. Marcin Balcerbyk, for the good work atmosphere, their helpful knowledge and their availability for make experiments possible.

To Dr. Tonner, for allowing me to collaborate with the Center for Engineering in Medicine, at the Massachusetts General Hospital, Boston. Especial thanks to Dr. Önel, for sharing their experiments with me.

To Dr. Fahy and the whole 21CM team, for giving me the opportunity of working with 21 Century Medicine and for teaching me so many things about organ cryopreservation. Special thanks to Dr. Wowk.

To my ISF friends, because they contribute to my personal development every day. Thanks to Marita, Celia and David, for sharing also their PhD experiences with me. Thanks to Bego for sharing her IT knowledge with me.

To my friends, because they are my family, they are always there, and everything makes sense after a day in their company: Izbor, Juanjo, Andrea, Isa, Eli, Juan, Rafa, Elena … and my old friends Tato, C. Angel, Patri, Nazaret, Maria, Ana, Pepe, Alfonso, Dani, Manuel ... , for such good moments spent and the moments to arrive. Special thanks to Pedro and Juanjo for their help with the thesis format and style.

To David Regalado, for so numerous things, I could write another thesis to enumerate the reasons. Because since we met at the lab he has been always by my side, he has taught me so many things and supported me as nobody has ever done.

To my parents, for their unconditional love and support and for being such special persons. To my sister, brother, sister- and brother-in-law, because of their love and support too. To my aunt Pepi, because she is a very important person in my life. To the rest of this big *gypsy family* and to all of them who have already passed away, especially to my grandma Covadonga. To my two little nephews, Julia and Ariadna, because it is just amazing to see them grow up and a pleasure to be a part of it.

1. Introduction, objectives and structure of the thesis

Cryobiology is the branch of biology that studies life at temperatures below their normal range. The technique used for conservation of biological material and storage at low temperature is called Cryopreservation. The cryopreservation techniques must allow the posterior recovery of the samples avoiding damages during the process. These processes are very diverse depending on the material to preserve. Cryobiology has multiple applications in many areas, such as Medicine or Biology among others. The medical applications have an important relevance, consisting of the storage of cells, tissues and organs for its posterior use in repairing those parts with no longer function due to disease, injury or aging.

Cryopreservation is based on a very basic principle: the aging process in cells is due to chemical reactions, and these chemical reactions can be dramatically slowed by lowering the temperature. Cryobiology studies processes in a vast temperature range, from hypothermia to cryogenics temperatures (normally -196 ^{o}C, the boiling point of nitrogen). However when we refer to low temperatures normally consider only phenomena that occur below the normal freezing point of pure water, which is defined as 0°C.

On the other hand, cells can be considered as sacs of water surrounded by a permeable oil membrane, under isotonic conditions. The low temperatures favor the freezing of the water, and this water ice phase transition is very critical in cryopreservation. Ice causes damages *per se* in cells, mainly

mechanical damages. However other damages are also derived from ice formation, such as an increase of the solute concentration in the unfrozen phase and its subsequent increase in toxicity. We are going to see some of these negative effects of ice formation in Chapter 2.

There is another possible state at low temperatures, which is very important in cryopreservation processes: the vitreous state. As we have said, at very low temperatures the motion of molecules slows, and therefore chemical reactions rates are slower. There is a certain temperature where the energy is insufficient for the mobility of most molecules in the fluid. This temperature is known as the glass transition temperature, and the system becomes a non crystalline solid, called “glass”. This process is also called vitrification, and it only occurs under certain conditions. For instance, water normally solidifies as a crystalline structure, but some chemical compounds in high concentrations can make it happen. These substances are called cryoprotective agents (CPAs) or just cryoprotectants. CPAs are of special interest in Cryobiology and very used in cryopreservation processes, due to their ability to avoid ice formation.

So far, cryopreservation has been applied successfully to almost all kind of cells in suspension and several relative simple tissues systems. Although there is a big interest on the creation of a biobank, especially applied to organ transplantation, the cryopreservation of complex tissues and bulky organs is still a challenge nowadays. Most constraints are due to the macroscopic dimensions of organs comparing to cells. The difference cryopreservation techniques require a good knowledge of the concentration and distribution of the CPA inside the organ and a control of the temperature. A review of cryopreservation of organs will be found in Chapter 2. In this thesis we propose some techniques that contribute to an improvement on tissues and organs cryopreservation processes. We have developed a method of measurement of CPA concentration distribution inside a tissue or an organ by means of X-ray computed tomography (CT). Moreover, we applied this CT technology to the detection of ice formation, either in vitrified samples or in samples during the cryopreservation processes.

Thanks to the collaboration of the Centro Nacional de Aceleradores of Sevilla, we have been provided with a NanoCT. The particular energy used in our CT device made possible the visualization of a particular CPA: dimethyl sulfoxide (Me_2SO). Me_2SO is one of the most commonly CPAs used in cryopreservation, and the sulfur atom of this molecule plays an important role in the X-ray attenuation, as we will see in Chapter 3. Moreover, we have developed a cooling system that allows us to control the temperature of the samples and maintain them at temperatures under the glass transition temperatures, being able to detect ice in vitrified samples. These techniques have an important application in complex tissues and bulky organ cryopreservation, and would permit to modify and adjust cryopreservation protocols in order to achieve a successful cryopreservation avoiding the ice formation.

The structure of this thesis is as follows:

Chapter 2 is a review of organ cryopreservation. The main issues of complex tissues and organs cryopreservation are exposed. A review of the first organ cryopreservation attempts is presented, as well as the most important discoveries which make it possible to develop the present techniques. Also some of the successful cryopreservation cases of tissues and organs are mentioned. Moreover, the different methods of CPA concentration measurements are numerated, also the methods for detecting the ice formation and for assess ice damages in tissues and organs. Chapter 3 introduces the theoretical basic principles of X-rays and their application to Computed Tomography. Furthermore, the effects taking place in our device and the comparison of them for different CPAs are explained. In Chapter 4, the materials and methods of the experiments are described. The results of these experiments are showed in Chapter 5, including CT images, graphs, tables and a brief discussion of these results. Finally, the conclusions are summarized in Chapter 6.

2. Organ cryopreservation: state of art.

Before starting with the review of organ cryopreservation, it is necessary to understand the traditional method of cryopreservation applied to cells in suspensions, known as slow freezing. As we said, cells are basically made of water, with a semi-permeable membrane which allows them to stay in equilibrium with the extracellular medium. Imagine that we have a group of cells in suspension in an isotonic solution. During the cooling process, extracellular ice is formed a few degrees below the freezing point of water (either spontaneously or induced by seeding the solution with an ice crystal), with a consequent increase in the solute concentration in the medium. Cells then loose water by osmosis, until they reach the same concentration than the unfrozen solution. As a result, a freezing point depressing occurs and the solution inside the cells cannot freeze. There is an optimal cooling rate to make it happens, the velocity has to be slow enough to let cells dehydrate. If the cooling process is too fast, cells will not have time to lose the water required to maintain the equilibrium, and intracellular ice will be formed (80). On the contrary, if the velocity is too slow, cells are exposed to a high solute concentration for too long, causing toxicity damages, and mechanical damages can be produced due to an excessive shrinking of cells (55). This process is normally facilitated by the addition of CPAs at higher concentrations than isotonic solutions inside cells. This optimal cooling rate depends on the parameters of the cells (ratio surface/volume, solutes…) and of the CPA concentration. A higher CPA concentration will allow for a higher cooling rate. If the cooling

process continues until temperatures below the glass transition temperature, cells will vitrify and long-term stability will be attained (131). Fig.2.1 shows the optimum cooling rates for three different cells: mouse oocytes, human lympocythes and human red blood cells, frozen to -196 ^{o}C in 0.7 to 1M Me_2SO. Curves show the usual shape of inverted "U".

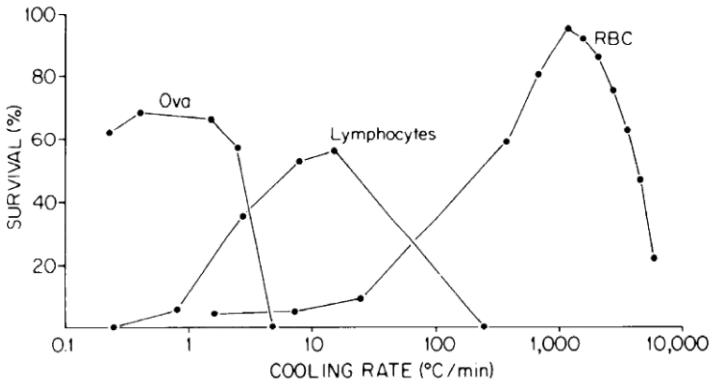

Figure 2.1. Optimum cooling rates for three different kinds of cells. From ref (80)

Nowadays, most cells in suspension are cryopreserved successfully either by slow freezing or other methods. However, when we apply these methods to complex tissues or organs results are not so good. We are going to explain the main reasons of why these processes do not work in organs.

2.1. Issues of organ cryopreservation.

Cryopreservation techniques of cells in suspension have been applied to multicellular tissues, obtaining good viability after recovery only in a few cases, such as skin or cornea, (11, 118). No recovery was obtained when applying those techniques to organs. The reason is because there are too many differences between cells and tissues, and especially between cells and organs. The main one is the lack of an extracellular medium to be frozen without damages in the tissues. Tissues and organs are made of different types of cells, vessels, connective tissue and extracellular components which make a complex architecture to produce functional units. Moreover, cells in tissues are densely packed compared to cells in suspension. It seems there is a "cell packing effect", which has been

demonstrated in erythrocytes (81, 91). According to those experiments, cells that are more concentrated in a solution suffer more damages than the same cells less densely packed. Other inconvenience is the addition of the CPA. In organs, CPAs solutions have to be added by perfusion through the vascular system, since it is the only way to reach all the cells. The process of perfusion might be harmful for organs, not only for the toxicity of the CPA but for issues with the osmosis processes. Thus, complicated perfusion techniques combined with the use of buffer solutions are required. On the other hand, cells in suspension have a high surface-volume ratio and are in contact with the extracellular medium, which allow for rapid and uniform changes of temperature. In organs, the bulk makes a low surface-volume ratio. Moreover interior cells are not in contact with the surroundings, making the changes of temperatures non uniform (51).

It is all these features that make cryopreservation of organs and complex tissues so complicated, and the consequences can be summarized in two issues: mass transport and heat transfer limitations. These issues merit to be explained in a deeper way in order to understand the magnitude of this complicated task which means organ cryopreservation. The following explanation is based on an analysis of cryopreservation of issues by Karlsson and Toner (55).

Regarding mass transport limitations in cryopreservation, there are two important processes of mass transport during freezing and thawing: the addition and removal of CPAs, and the distribution of biological water. In cells in suspension, those effects are governed mainly by membrane-limited water transport, however, in tissues and organs diffusive processes and cell-cell interactions must be considered. In tissues or organs, water diffuses sequentially from one cell to its neighborhood. It means, that while cells in the surface layer respond to osmotic changes in the extracellular medium, interior cells respond only to osmotic changes in cells of surfaces, having slow rates of dehydration (67). Moreover, water diffusion depends also on the tissue composition. For instance, in highly vascularized tissues, such as liver, interior cells can exchange water with ice in the vasculature. On the contrary, in multilayer tissues, such as skin, intracellular cells depend only on the cells of the surface layer, being more likely to freeze. On the other hand, we need to consider the CPA diffusion in tissues during

the addition and removal of these CPAs. Specific diffusion times depend on both, composition and geometry of the tissues, and these times can vary from minutes to hours. Longer exposition times to CPAs are associated with a higher risk of toxicity, but can reduce the osmosis stress (111). Therefore, these mass transport limitations in large tissues and especially in organs will produce spatial concentration gradients. Thus, better models of CPAs diffusion are necessary as well as improved techniques to measure CPA distribution in tissues.

An analogous effect occurs with heat transfer limitations in tissue cryopreservation. Due to the macroscopic size of organs and their finite thermal conductivity, achieving rapid cooling/warming rates it is more difficult that in the case of cells in suspension. And therefore thermal gradients will appear in the tissues (25). On the other hand, it is needed to remark that if interior cells had slower rates of water transport, they would need slower cooling rates than those of the cells on the surface, in order to dehydrate sufficiently to avoid intracellular ice formation (73). Thus, those slower cooling rates in the interior cells could compensate the slower rates of water transport. Nevertheless, heat transfer limitations might be more critical on the rewarming more than on the cooling process, due to an increase of possibility of devitrification and recrystallization. These two effects refer to the ice formation during the rewarming process, due to the high likelihood of growth of ice nuclei formed during cooling. But we will further explain them at the end of this section.

These limitations have negative consequences and increase the likelihood of producing damages on the samples during the cooling processes. The inefficient mass transport produces an uneven distribution of CPA in tissues as result: some regions are not protected, being more likely to freeze, while other regions are overexposed to toxicity. In a similar way, the non-uniform rates of temperature changes makes it impossible to achieve an optimal cooling or warming rate in large sections of tissues. Moreover, thermal gradients can induce thermal stress due to uneven expansions or contractions in the sample (25, 107). A very high level of thermal stress could produce fractures and consequent damages (33, 35). The heterogeneous composition might have several negative consequences too, since different elements of the tissue would have different physical

properties (e.g. thermal expansion conductivity). On the other hand, different types of cells required different optimal cooling/warming rates (52, 77). Nevertheless, it seems that the addition of CPAs makes the region of the optimal rate wider, increasing the likelihood of an optimal cooling rate involving all different types of cells. Moreover, it has been demonstrated that structural damages in vascularized samples are due to the formation of ice mostly in the intravascular space (108). As result, dehydration of surroundings makes water to accumulate and freeze in the vascular system, with the consequent rupture of blood vessels.

Besides all these freezing damage mechanisms, the warming process deserves special attention because of the high risk of ice formation during this process. The phenomenon of ice formation during warming is known as devitrification. When a clean solution cools below the melting point temperature during the cooling process, an ice nucleus can form spontaneously. This ice nucleus is not thermodynamically stable until it reaches a minimum size, since some interfacial energy is needed (72). Nonetheless, even if the growth of the ice nucleus is avoided during the cooling process, these nuclei can find the energy needed during warming to grow to ice crystals (also known as recrystallization (41)). Furthermore, devitrification can also happen from the growth of new ice nuclei formed during warming. Numerous experiments have been performed to study devitrification and the relation with warming rates (71, 76, 15, 114). Moreover mathematical models have been developed (56). All results indicate that a rapid warming rate might be the solution to avoid devitrification, since there is no sufficient time for growth to occur before the melting point is reached. However, it has been found a few cases where rapid warming rates cause more damages than slower rates (81). It appears that rapid warming rates are favorable in cases where samples have been cooled also rapidly (79), and rapid warming process have been developed to that effect such as electromagnetic warming, described in section 2.4.

2.2. First attempts of organ cryopreservation: the role of the cryoprotectants discovery.

In 1949, the discovery of cryoprotective properties of glycerol by Polge, Smith and Parkes (100) marked a new era in cryopreservation, and it has been essential in organ cryopreservation. These Scientists were attempting the sperm cryopreservation by adding a saline solution and varying its composition. One day, accidentally, they added glycerol instead, which had a different use in the laboratory. They were surprised by a recovery of motility higher than 50%, while the usual was 5%.

The discovery of the protective action of some compounds encouraged cryobiologists to perform the first attempts of cryopreserving organs. In 1957, the first mammalian organ is perfused by Audrey Smith (119). In her experiments, hamster's hearts were perfused with 2M glycerol, cooling to -20 ^{o}C with a slow cooling rate (1 ^{o}C/min) and rewarming at ten times the cooling rate. After hearts were thawed and washed of glycerol, some weak contractions were showed, while no functional recovery was showed while cooling them with no glycerol. However, when hearts were cooled to -79 ^{o}C and rewarmed at 100 ^{o}C/min, no functionality was observed. Some years later, Smith and Lovelock perfused guinea pig uterine horns with 20% glycerol and cooled them to -79 ^{o}C (120). After thawing they recovered some of the contractile ability. In the decades of 60 and 70, a great number of experiments were performed to attempt tissue or organ cryopreservation, with not very good result. Some exception were dog small intestine segments which were successfully stored in liquid nitrogen during 7 days (46). The intestine segments were perfused with 10% Me_2SO and cooled to -70 ^{o}C in dry ice before being introduced in liquid nitrogen. Segments were pre-warmed in dry ice before a rapid warming in a warm saline solution. The intestine segments showed a good structure and a perfect functional recovery after their implantation into the animals. Another case of successful storage was reported in 1976 (78). Fetal rat pancreases were storage to -78 and -186 ^{o}C with post-thaw survival, although no case of adult pancreas has been reported.

Among all this attempts to cryopreserve organs in those decades, most experiments were performed with hearts and kidneys, however no fully

recovery was obtained. Some of the different heart experiments were: frog hearts perfused with glycerol and cooled to liquid nitrogen (1), rabbit hearts with 10% glycerol perfusion cooled to -21 ^{o}C (20), dog hearts perfused with Me_2SO cooled to -12 ^{o}C or rat hearts perfused with Me_2SO and cooled to -15 ^{o}C or -20 ^{o}C (6, 58). However, after thawing them only some beating was showed in most cases. Regarding kidneys, some of the experiments with better results were: rabbit kidneys perfused with Me_2SO and cooled to -22 ^{o}C (23, 64), with survival but limited function after transplantation, dog kidneys perfused with glycerol and cooled to -50 ^{o}C (45) and the most promising experiments were performed by Guttman with dog kidneys (43). Kidneys were permeated with Me_2SO and cooled during perfusion with cold helium and most warming processes were carried out in a microwave. The result was more of 50% survival, good morphology and an excellent functional recovery after transplantation. However, those results were never obtained again even by Guttman himself (44).

Fortunately, the numerous studies and advances until today have made it possible to obtain better results in cryopreservation of tissues and organs. Nowadays, several tissues are able to be successfully cryopreserved. Moreover there have been great advances in organ cryopreservation, mainly in kidneys. They will be mentioned at the end of the section 2.3. In the following, we are going to describe two of these important events that have marked a new hopeful era in organ cryopreservation.

2.3. Methodology of tissues and organs cryopreservation.

As we have mentioned, there are two breakthroughs in cryopreservation of tissues and organs: the method of Farrant in 1965 (40), and the vitrification of embryos by Rall and Fahy in 1985 (101). These two events have originated two different methodologies of tissue and organ preservation.

Farrant's method consisted of adding the CPA solution in steps, increasing the concentration while decreasing temperature, in order to stay above the melting point of the phase diagram. Increasing concentrations of Me_2SO solution were added to guinea pig uteri while cooling in steps to -79 ^{o}C. Not only freezing was avoided in uteri but it showed a normal contractile ability while testing it as response to histamine. The addition of Me_2SO protected

not only of ice formation, but decreasing the salt concentration of electrolytes, as it can be seen in Fig.2.2. Fig.2.2.A shows the phase diagram of the three components system Me_2SO (DMSO)-NaCl-water. The eutectic temperature of the system DMSO-water is -139 ^{o}C (X), while the eutectic temperature of NaCl-water is -21 ^{o}C (Y). Fig.2.2.B shows a zoomed in view of the ice liquid interface. The curve *abcd* represents the three components system DMSO-NaCl-water, the curve *efgh* the two components system NaCl-water and the curve *ijkl* the system DMSO-water.

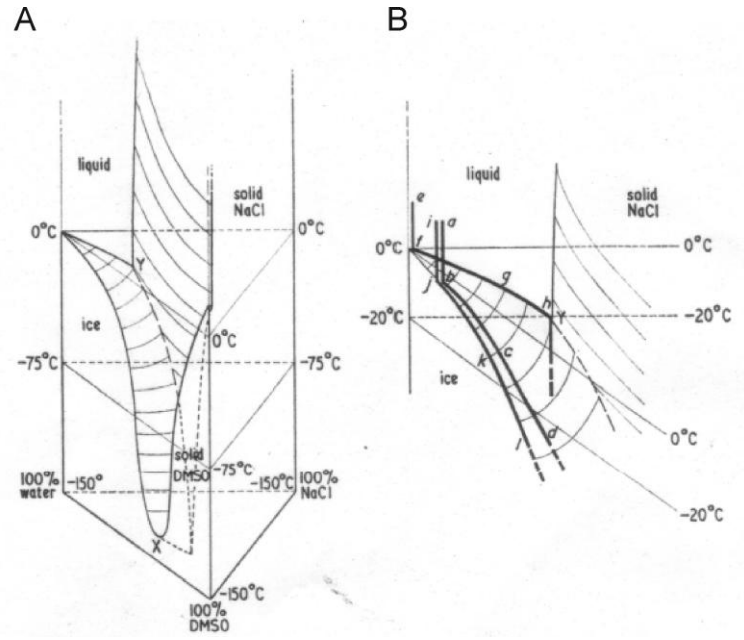

Figure 2.2. Phase diagram of the system DMSO-NaCl-water. From ref (40)

In 1972 Elford and Walter (29) also tested Farrant's method with smooth muscle tissue. They increased Me_2SO concentration in steps as cooling proceeded so that ice was never allowed to form. In 1974, this method also permitted to cool a heart frog to -78 ^{o}C in steps with addition of ethylene glycol, and recover its normal function after thawing (103).

Liquidus Tracking

In 1970, and based on Farrant's method, the group of Mill Hill in London (88, 116) built the first equipment capable to control the perfusion of cryoprotectant and its posterior washing out in a whole organ. It allowed to perfuse rabbit kidneys with 2M glycerol at 5 ^{o}C (89) and 4M glycerol at 10 ^{o}C (90), with the posterior survival and perfect functionality of kidneys. The perfusion consisted of adding and removing the glycerol with slow rates in changes of the concentration. Later, in 2006, Pegg et al. (94 to 97), at the University of York, developed a method called Liquidus Tracking which allows the successful cryopreservation of cartilage. This method consisted on, continuously, controlling the temperature of the sample and the CPA concentration, following the liquidus transition curve during the cooling process.

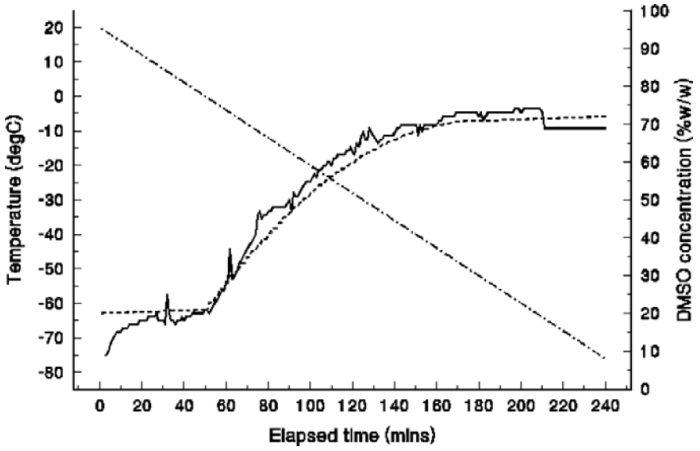

Figure 2.3. Plot of temperature, the Me_2SO concentration program (dashed line) and the actual Me_2SO concentration (solid line). From ref (97)

The Fig.2.3 shows the profile of temperature and Me_2SO concentration followed during the cartilage cryopreservation process. The dashed line represents the Me_2SO concentration program and the solid line the actual Me_2SO concentration.

Vitrification

In 1985, Rall and Fahy (101) demonstrated that another way of cryopreservation was possible. They achieved the vitrification of mouse embryos with high concentrations of cryoprotective solution cooling them rapidly into liquid nitrogen. At very low temperature, the solution became so viscous that solidified without ice formation, i.e. it vitrified. In 1984, Fahy et al. (33) had already pointed out the vitrification as an alternative for cryopreservation. They studied the different regions possible in a phase diagram of a CPA, in such as way that it is possible to avoid ice formation in samples by the addition of high CPA concentrations and cooling them rapidly at very low temperatures, below its glass transition temperature. This meant another method of organ cryopreservation which did not involve equilibrium. Fig.2.4 shows the different paths possible for vitrification in a glycerol-water phase diagram, taken from Wowk 2010 (131). Fig.2.4.A shows the non vitrification method proposed by Fahy et al., where the sample passes rapidly by the metastable region until the region under the glass transition temperature (T_g). The metastable region is the region between T_m (the melting point temperature) and T_h (the homogeneous nucleation temperature). Fig.2.4.B shows the equilibrium vitrification paths. Equilibrium vitrification is considered when the sample remains always in the stable region (above T_m), before achieving the glass transition temperature. In the Liquidus Tracking method (a), the sample remains always slightly above the liquidus line. Another equilibrium vitrification is represented (b) where there is a long isothermal until a high CPA concentration before cooling it before cooling it. This last method was proposed by Boutron in 1978 (14) and it permitted to vitrify cells even at slow cooling and warming rates.

As a downside, vitrification processes proposed by Fahy et al. and Boutron require highly concentrated and therefore more toxic cryoprotective solutions at ambient temperature. Thus, there was a need to develop non-toxic vitrification solutions. Fahy et al. focused part of their research on the preparation of low toxic vitrifying solution and the design of a perfusion protocol (33, 34, 36, 37, 38, 59, 60, 130, 3). Those vitrification solutions are mainly based on a combination of different CPAs (Me_2SO among others), ice blocking agents, saline solutes and buffer substances. Vitrification

solutions are also characterized by the melting temperature and the glass transition temperature, and the temperature regions where the nucleation and the crystal growth happened. Other parameters such as the temperature or the pressure of the perfusion are also controlled.

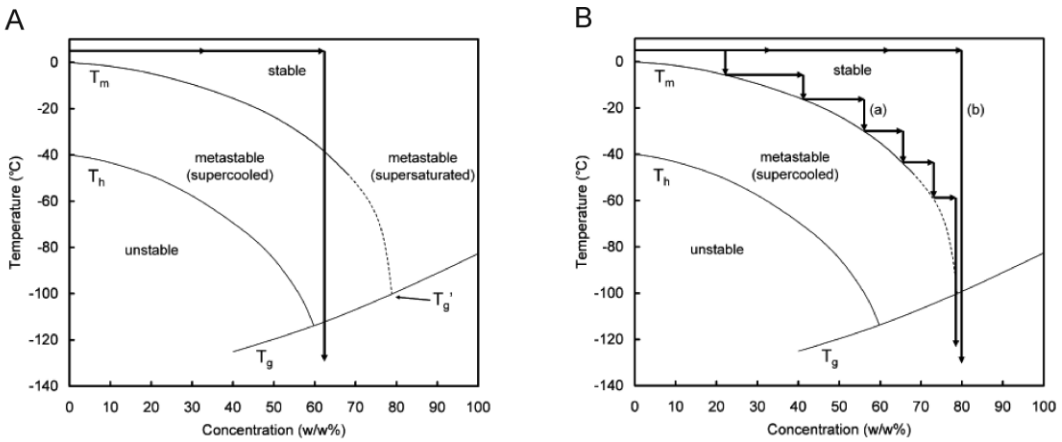

Figure 2.4. Different ways to achieve vitrification on a phase diagram of the system glycerol-water. A) Non-equilibrium vitrification. B) Equilibrium vitrification: (a) *Liquidus Tracking* method, (b) warm equilibration with an unfreezable solution. From ref (131)

All these efforts have achieved important advances in kidneys preservation (33, 34, 36, 38, 59, 60, 3) with a case of an animal survival after transplantation of a vitrified kidney (39). A rabbit kidney was perfused with a vitrification solution progressively until 9.2 M at -22 ^{o}C, as showed in Fig.2.5.A, with the exception of an increase of the pressure. The kidney was then cooled to -140 ^{o}C in vapors of liquid nitrogen. Afterwards, the kidney was thawed slowly to above T_g and then rapidly by conduction (Fig.2.5.B). Right after the kidney was transplanted into the rabbit with survival of the animal. The animal was then euthanized after 48 days and the kidney was assessed. The study showed that it was partially damaged because of ice formation, due to an uneven distribution of the cryoprotectant in some parts of the kidney.

In the case of tissues, many successful cryopreserved tissues have been reported in the last decade. Some of these examples include cartilage (94 to

97), small ovaries (124, 110, 82, 21, 8), blood vessels (122), heart valves (16, 17) and corneas (2).

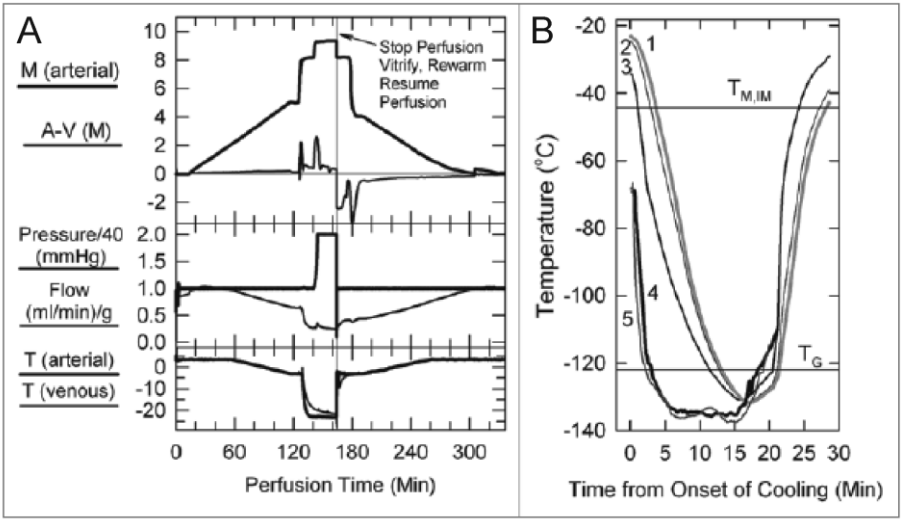

Figure 2.5. (A) Perfusion protocol of the survival rabbit kidney, with exception of the pressure that in this case was increased to 80 mmHg. (B) Temperature during the cooling and thawing processes of the survival rabbit kidney. From ref (39)

Electromagnetic Warming

As it was mentioned in section 2.2, recent reports prove that warming process might be more critical in organ cryopreservation, due to the likelihood of devitrification. It appears that a rapid warming could avoid devitrification. One of the methods investigated and most used to obtain a rapid warming rate is electromagnetic warming. Two different mechanisms of heating are possible in electromagnetic warming: ohmic heating and dielectric heating. The former is caused by movements of ions in response to the electric field, while dielectric heating is caused by rotation of polar molecules (especially water) in response to the electric field. The energy of the movement of ions and polar molecules is dissipated by friction with other surrounded molecules, and therefore causing heating.

The most important parameter in electromagnetic warming is the frequency of the electromagnetic wave. Ohmic heating is however independent of frequency and depends only on the electric field strength. At lower viscosities, mobility and conductivity of ions increase, producing an increase of temperature. This has associated the risk of *thermal runaway*, since hotter areas will heat faster than the others, producing a non-uniformity heating. On the contrary, dielectric heating depends on the frequency, and the heating is maximal at a particular frequency. This particular frequency varies inversely with the viscosity, which means that the higher the temperature is, the higher the optimum absorption frequency. This can be seen in Fig.2.6., from the study by Evans in 2000 (32) Fig.2.6.A shows efficiency of dielectric absorption in 50% v/v Me_2SO, expressed by loss factor, for four different frequencies. Fig.2.6.B shows the loss factor at the same range of temperature in 50% v/v Me_2SO in a carrier solution. The ion content of the carrier solution makes the ohmic heating to take place in the heating mechanism. As the temperature increases, the absorption becomes higher and therefore the temperature increases more and more.

Thus, it is important that the carrier solution has a low ion composition to avoid the ohmic heating, which is more likely to produce *thermal runaway*. Another approach to avoid *thermal runaway* is to work at a frequency below the optimum absorption frequency at the lowest temperature. Since during the warming process we go to higher temperatures, in this way the optimum absorption frequencies will be increase and warmer areas will heat less effectively avoiding non uniform heating. Moreover, to achieve a special uniformity there are two other effects to take into account: penetration depth and resonance effects. Penetration depth of the frequency must be greater than the size of the tissue or organ to be warmed in order to avoid surface heating more than the interior (75). Moreover, the wavelength must be also larger than the organs to avoid resonance effects (node and antinodes) (5). There is also an effect of reduction of the electric field inside the tissue, determined by the geometry and the electrical properties of the tissue (32). It is so necessary a good knowledge of the electric properties of tissues and the cryoprotective solutions, including the carrier solution. As conclusion, a particular frequency is critical to achieve a uniform warming, depending on the size

and geometry of the tissue or organ and on the composition of the vitrification solution.

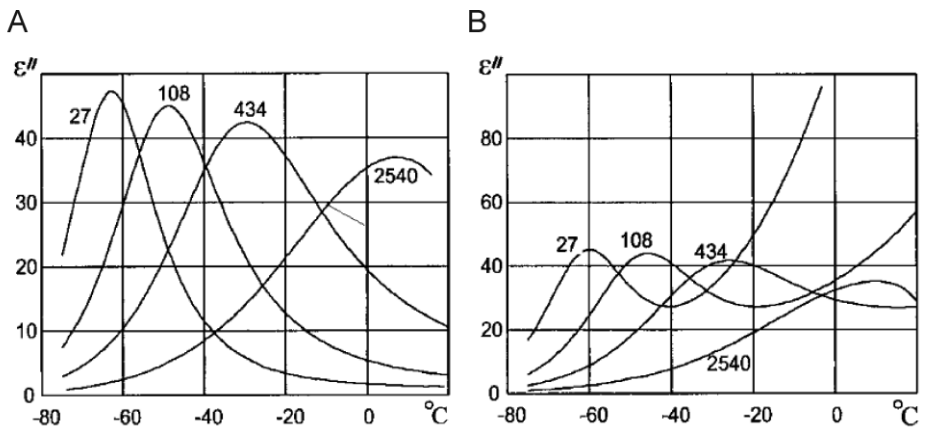

Figure 2.6. Efficiency of dielectric absorption (loss factor) versus temperature in a 50% v/v Me_2SO solution (A) and in a 50% v/v Me_2SO in a carrier solution (B), at four different frequencies. From ref (32)

First attempts of warming electromagnetic were performed by Halasz, Diezman and Guttman in later 60's and 70's (45, 23, 43). They used frequencies of conventional microwaves (2450 MHz) in dog kidneys, although no good results were obtained. In 1987, Marsland (75) suggested best frequencies for dielectric heating were from 300-1000 MHz for glycerol 3M cryoprotectant. Based on that, Evan's group built a resonant applicator operating at 434 MHz (75, 5). This equipment was adapted and refined by Robinson and Pegg and different experiment were performed to study electrical properties of different CPAs (105, 106). In 1990, Ruggera et Fahy (109) applied different radiofrequencies to a cryoprotective solution composed of Me_2SO and acetamide, at different powers. The highest warming rate achieved was 300 ^{o}C/min, in the range of -70 to -40 ^{o}C, which is the most favorable region for devitrification for the solution they used.

All this points out that electromagnetic warming might be a possible way to warm rapidly vitrified organs avoiding devitrification. However, there is still need to further research in this field and to improve these techniques to apply to vitrified organs.

2.4. Methods of CPA concentration measurement.

In this thesis we propose a new method of CPA (Me_2SO) concentration measurement and monitoring by X-ray Computed Tomography using low energies and its application to organ cryopreservation. Other methods to measure and control the CPA concentration have been used in organ cryopreservation. In this section we are going to make a review of the most important methods proposed and their limitations.

In 1969, Elford (28) measured the concentration of the CPA by a method called immersion weighing, which depended on the density difference between the CPA solution and water. When a piece of tissue was immersed in a CPA solution, it was possible to monitor the permeation of the CPA in the tissue using the change in immersed weight with respect to time. Based on his work, in 1994, Pegg et al. (92) presented a method to monitor the CPA transport in tissues, improving this gravimetric method in 2006 (93). The method was proved with a solution with Me_2SO and sucrose, and times were similar to those estimated by equations. However, it was not possible to differentiate the phenomenon of osmotic dehydration from CPA permeation, since they are very similar effects. Moreover, when they used the same method with glycerol, they did not get the expected results.

A year later Pegg et al. (95), in the Liquidus Tracking method, used a High-Performance Liquid Cromotography (HPLC) to determine the amount of CPA and the Karl Fischer method to determine the content of water in the sample. The Karl Fischer method consists on a volumetric titration with iodine reactive. CPA concentration was expressed in terms of tissue weight as follows:

$$\frac{\text{normalized weight of CPA x } 100}{\text{normalized weight of water} + \text{normalized weight of CPA}} \% \text{ w/w}$$

Another method is the use of electrical impedance as a marker to measure and monitor many biological parameters and processes, with the advantage of being a non-invasive and relatively cheap technique. Wang et al. (129) measured the response of fish embryos to the cryoprotective chemicals methanol and Me_2SO, using EIS (Electric Impedance Spectroscopy), in

Zebrafish embryos. They proved that the permeability of embryo membranes to CPAs could be monitored in real-time. The results obtained for permittivity and conductivity changes were encouraging for the development of EIS technique to cryopreserve fish embryos (133). In the work performed by Olmo et al. (87), the influence of temperature and CPA concentration in bioimpedance measurements was studied at different frequencies. The frequency response of a two electrode system to different concentrations of Me_2SO perfused into 3T3 fibroblasts and Monolayers of Mesenchymal Stem Cells (MSCs) was analysed with COMSOL Multiphysics software.

Fahy et al. used the difference between the refractive index of the urine and venous blood in kidneys to determine the equilibration of the tissues to the vitrification solution M22 (39). Fig.2.7 shows the difference between venous and urine during perfusion.

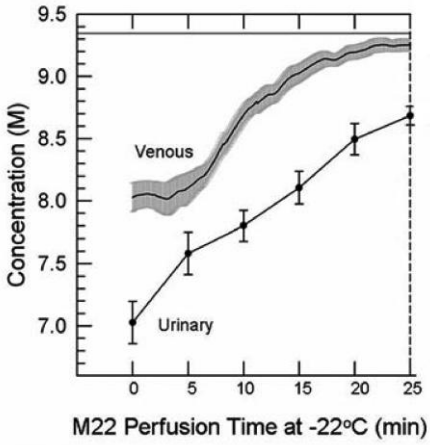

Figure 2.7. Difference between the venous concentration and the urinary space concentration during M22 perfusion at -22°C. From ref (39)

All these methods provide global information of the CPA concentration in samples, but they lack of the precision required to measure CPA concentration locally and therefore to know the CPA distribution inside a tissue or an organ.

A few imaging methods have been attempted to measure the CPA concentration, e.g. the Nuclear Magnetic Resonance. Proton Nuclear Magnetic Resonance (H NMR) has been used to measure the concentration of CPA (for example Me_2SO) concentration in tissues and organs (42, 125, 7, 50, 121). This method is based on the different proton spectra of the Me_2SO and water. Integration of the areas under the two peaks in the spectrum allows the determination of the proton ratio of Me_2SO with respect to water and the calculation of the concentration. H NMR was used by Fuller et al. (42) with rat livers in 1989 and by Taylor and Busza (125) with cornea in 1992. Later, Bateson et al. (7) used H NMR to measure the concentration of Me_2SO as it penetrated the common carotid artery of a rabbit. This method has also been used with other CPAs as well. In 1997, Isbell (50) used C4S NMR to monitor the penetration of cryoprotectant solvents in tissues (rat kidneys and rat livers) and measured the effective diffusion coefficients. Po-Wah So and Fuller in 2001 (121) made use of H NMR to determine the diffusion of solutes present in preservation solutions in rat livers during hypothermic storage (histidine and carnosine). The aromatic protons of histidine as well as the histidyl moiety of carnosine resonance frequencies are observed in the NMR spectrum, and integration of these resonances allow to establish the amount of solutes present in the sample. Among the inconveniences of H NMR are its relatively low precision (errors are of the same order of magnitude as the measurements), that is an expensive procedure, and its relative complexity. Other imaging techniques as MR have been used, however long acquisition time is necessary besides there is image contamination due to bound water (10).

CT technologies have already been used. Bischof et al. (12) used X-ray Tomography to map crystalline and amorphous phases and studied the applications to cryopreservation and cryosurgery. One of the main differences with our work it is the high acceleration voltage used, 420 kV versus 75 kV maximum used in our CT device. In these experiments they used glycerol as CPA and they obtained images of different concentration of glycerol solutions and tissues at three different temperatures, -196 ^{o}C, -78.5 ^{o}C and 20 ^{o}C. The CT signal obtained varied with the CPA concentration and with the temperature. For 20 ^{o}C the CT was almost proportional to the concentration of cryoprotectant. However, for the temperatures of -78.5 ^{o}C and -196 ^{o}C the curves were linear until a certain concentration, changing

the slope when a phase change occurred. This can be seen in Fig.2.8, where the X-ray attenuation is represented verus the CPA concentration at different temperatures.

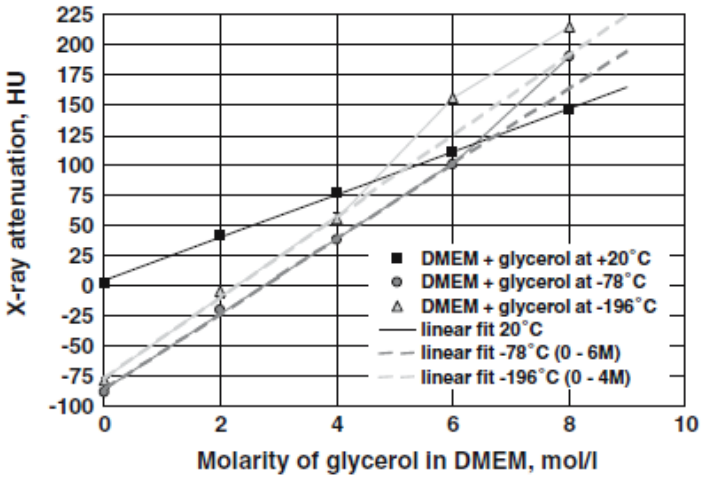

Figure 2.8. X-ray attenuation (HU) of glycerol (0-8 M) in DMEM at 20, -78 and -196°C. From ref (12)

At the X-ray energy that Bischof et al. worked, the changes in X-ray attenuation are due mainly to changes in density which depend on temperature and phase changes. On the contrary, due to the low range of energy that we used, the attenuation depends mainly on the atomic number of the substance, having proportional CT signals only to the Me_2SO concentration, at any temperature. All this will be further explained in Chapter 3.

2.5. Ice detection methods.

We have already mentioned that ice, intra or extracellular, is one of the main causes of damages in cryopreservation processes of cells, tissues and organs. There are many studies to assess ice damages in cells, as we will see in this section, especially studies of intracellular ice formation. However there are not too many in tissues or organs. In 2010, Pegg et al. compares the consequences of ice formation on tissues (smooth muscle and articular

cartilage) and organs (kidneys) (98). He found that there is a strong relation between the formation of ice, extra or intracellular, and structural and functional damages in tissue and organs. He also found out that the site of the ice is important to evaluate the damages, and the mechanisms of injury depend on each system. In this section we are going to mention the techniques most used to determine the ice formation, and the main methods to assess the damages produced by ice in tissues and organs.

One of the most common techniques used to detect at which temperature intracellular ice formation occurs is the differential scanning calorimetry (DSC). Differential scanning calorimetry is a thermoanalytical technique which measures the changes of the difference in the heat flow rate to the sample and to a reference sample while they are subjected to a controlled temperature program (47). Since the phase change from liquid water to ice requires more energy it is possible to know the moment when ice is formed. This technique has been widely used in cells, such as human lymphocytes (30, 19), Drosophila Melanogaster embryos (86) or frog oocytes (62). In 2008, Seki et al. (114) used this technique in a type of yeast and at different cooling rates. A first exothermal peak meant the extracellular ice formation and a second exothermal peak referred to the intracellular ice formation (IIF). To prove the second exothermal reaction was due to the IIF another cooling process was performed, if there was IIF membrane would be damaged and one only exothermal reaction would happen. In 2011, Mori et al. (83) used the DSC in human fibroblasts to detect IIF and the water transport at various cooling rates. So intra and extracellular ice can be detected, studies of the influence of cooling/warming rates, and water transport. However this method does not give information about the location or the size of the ice.

In 2007, Yoshimori et al. (132) used impedance to detect when the crystallization occurs in solutions. In the experiments, the eutectic crystallization is detected with impedance in NaCl solutions. Impedance is function of frequency and temperature, and a jump in the impedance is showed when the crystallization occurred. These techniques detect when the ice formation is taking place, but they do not give any information either about the site where the ice is formed or the damages caused by it.

One of the most useful methods to visualize ice formation in cells is the cryomicroscopy. The main advantage of cryomicroscopies is that they provide continuous visual information at controlled cooling rates from a very wide range of temperature, from ambient temperature to liquid nitrogen temperature. It has been used to study ice formation in many types of cells: erythrocytes (24), oocytes (66, 126), granulocytes (115), fibroblasts (84) or endothelial cells (123) among others. In most cases of IIF a darkening process happens from one side to another side of the cell. The opacity is due to the refraction of the ice crystals to light. However, this method has its limitations in tissues and organs, since samples have to be thin and translucent enough to be observed under the microcopies (49). Fig.2.9 shows images of mouse oocytes made for Leibo et al.(66) in 1978. Oocytes where imaged in a cryomicroscopy while cooling at 3 ^{o}C/min at temperatures of: 0 ^{o}C (A), -3 ^{o}C(B), -5 ^{o}C (C), -20 ^{o}C (D) -28 ^{o}C (E), -18 ^{o}C (F), -50 ^{o}C (G), -52 ^{o}C (H) and at 4 ^{o}C (I) when warmed at 8 ^{o}C/min until ice was melted. The pictures show the extracellular ice formation from picture (B), the progressive shrinking of the cell until it crashed (F) and the cell became darker.

Other techniques have been applied to detect ice crystals in cells, such as X-ray diffraction in pollen (22) or gamma radiation in lichen fungi (61).

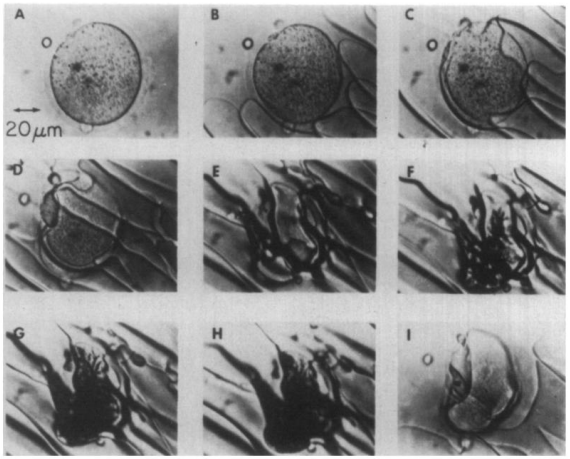

Figure 2.9. Cryomicroscopy views of mouse ova cooled at 3 ^{o}C/min from 0 ^{o}C to -58 ^{o}C (A to H) and warmed to 4 ^{o}C (I). From ref (66)

Apart from these techniques, some mathematical models have been developed to predict intracellular ice formation in isolated cells, (53, 54, 79, 85,) and even to predict the ice growth into macroscopic crystals (99, 126). However, in the case of tissues, developing mathematical models is much more complex since damages caused by freezing in tissues and organs are due to more factors.

However, all those techniques lack the precision to accurately maintain the location of the crystalline matrix of the frozen material. There are some techniques widely used to determine the location of the ice formed in tissues. The most commonly used are freeze-substitution and isothermal freeze-fixation. In freeze substitution, an organic solvent (water-soluble) is used to dissolve ice and remove it and cryoprotectants from the frozen tissue. It can be used a very wide range of temperature, from -30 to -120 ^{o}C. However there are two problems associated freeze-substitution: recrystallization and collapse (48). Recrystallization is more likely to happen when the sample has been cooled fast. Tiny ice nuclei can be formed during the cooling process and are risky to growth and form ice crystals during the freeze substitution process. Collapse might happen at very high subzero temperature. It is associated with the viscoelastic nature of the concentrated amorphous solute phase at temperatures above the glass transition temperature. It results in the loss of the freezing pattern and the alteration of the spatial relationships of cellular and subcellular structures.

Fig.2.10 shows an example of the application of freeze substitution in cartilage, from Pegg el al. (95). Fig.2.10.A and Fig.2.10.B shows the appearance of control cartilage, sectioned and stained with toluidine blue. Fig.2.10.C and Fig.2.10.D shows the cartilage that was cooled with 10% Me_2SO at 1 ^{o}C/min to -80 ^{o}C, freeze-substituted at that temperature, and also stained with toluidine blue. Ice crystals can be seen inside the chondrons of the cartilage.

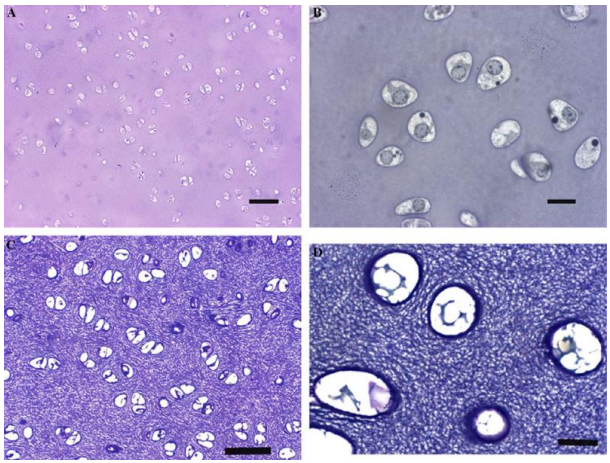

Figure 2.10. Freeze substitution with Me_2SO in cartilage. From ref (95)

Isothermal freeze-fixation consists of the chemical fixation of frozen tissues using conventional fixative at constant temperatures. Those fixatives are designed to have the melting point at the temperature you are interested in fixating the sample. Fig.2.11 shows an example of freeze-fixation of frog sartorious muscle tissues done by MacKenzie in 1975 (74). Fig.2.11.a and Fig.2.11.b show cross and longitudinal control tissues, respectively, while Fig.2.11.c and Fig.2.11.d show the same tissues after freezing and freeze-fixation in aqueous formaldehyde at -2 ^{o}C.

Both techniques give information about the amount of ice and the distribution inside the tissues, being able to obtain a relationship among the ice, the functional elements and the integrity of the tissue or organ. However they are valid in a particular range of temperature and there are risks of artifacts or damages during the application of the techniques that might alter the structures or misinterpret the results.

Another similar technique is freeze drying, although has to be used at very high subzero temperature and it has a high risk of collapse, losing the ice pattern. Besides, freezing drying gives similar results than freeze substitution, but freeze substitution is easier, cheaper and more reliable (49, 68). Some examples of tissues or organs assessed with these

techniques are: smooth muscle (48), cartilage (97), kidneys (90), heart (57), myocardium (117), lymphocytes (128) or sartorious muscle (74).

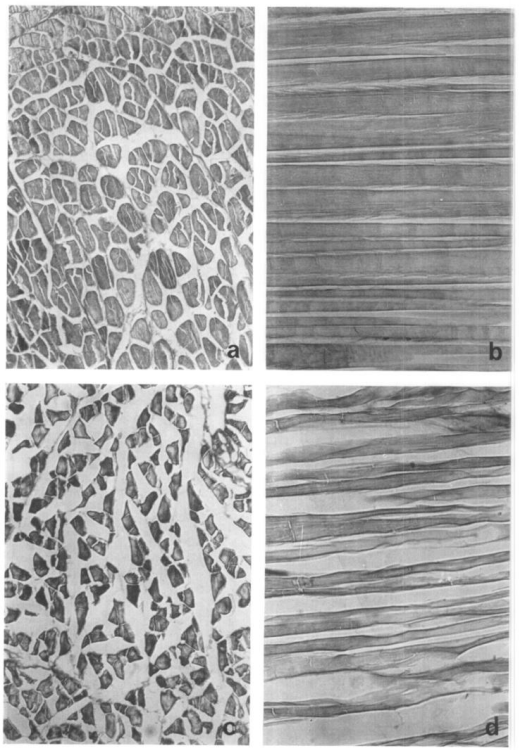

Figure 2.11. Frog sartorius muscle tissues, controls (a, b) and freexe fixed (c, d). From ref (74)

In 2007, Bischof et al. (12) applied X-ray Tomography to map crystalline and amorphous phase in frozen biomaterials. They used higher energy of the X-ray source compared to our experiments, 420 KeV versus maximum 75 KeV in our device. The changes in density of the crystalline phase of the frozen samples resulted in differences in the X-ray attenuation of the samples.

2.6. Me_2SO as cryoprotectant.

Dimethyl sulfoxide (Me_2SO) is an organosulfur compound with the formula $(CH_3)_2SO$. It is a colorless, odorless liquid, whose melting point is 18.45 ^oC and the boiling point is 189 ^oC. Me_2SO is prepared by oxidation of the

homologous series of organic sulfoxides. It is a useful solvent for many types of inorganic and organic compounds. The molecule is represented in Fig.2.12. It has two methyl groups, an oxygen and a sulfur atom, and it is a polar molecule. We will see in the following chapter that the sulfur atom is the key of this research.

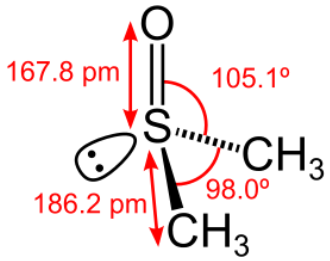

Figure 2.12. Me_2SO molecule

After the discovery of the cryoprotective properties of glycerol in 1949 (100), other substances with the same cryoprotective abilities were looked for. According to Lovelock (69), the protection of those compounds was due to their colligative properties, the ability to prevent the excessive concentration of electrolytes on freezing. Furthermore, cryoprotectants have to be the following features: non toxic, low molecular weight, high solubility in solutions with electrolytes and ability to permeate living cells. Other alcohols, amides and sugars also demonstrated to have protective actions (69).

In 1959, Lovelock and Bischop (70) compared the protecting abilities of Me_2SO and glycerol. It appeared that glycerol was not permeable to some cells, e.g. blood red cells. In their experiments, different concentrations and exposure times of Me_2SO and glycerol were used in sperm and red blood cells, and cooled them to -79 ^{o}C. Results showed that glycerol was better in sperm, although Me_2SO also showed some protecting action. On the contrary, in the case of red blood cells, Me_2SO was proved to be more permeable to those cells than glycerol. Me_2SO penetrates the cells more rapidly and therefore less solute was needed to complete protection. It was proved that Me_2SO might serve as an alternative cryoprotective agent.

In 1965 Farrant (40) also proved the ability of Me_2SO to reduce the electrolyte concentration as ice was separated. He studied the phase diagram of the system Me_2SO-NaCl-water, as we have seen in section 2.3. In 1968, Rasmussen studied more exhaustively the phase diagram of the system Me_2SO-water (104). The study indicated that the system could crystallize completely and that, under certain conditions, a stable hydrate, Me_2SO tri-hydrated, was formed. Fig.2.13 shows the phase diagram where both equilibrium and non-equilibrium transitions are included. In the diagram L refers to liquid; and the rest compounds, which are solids, refers to: A, H_2O; B, $Me_2SO.3H_2O$; C, $Me_2SO.2\text{-}1/2H_2O$; D, $Me_2SO.1/2H_2O$ and E, Me_2SO. The diagram also shows the glass transition temperature, T_g, from 40 to 80% w/w of Me_2SO, and the crystallization temperature during warming, T_c, from 40 to 55% w/w of Me_2SO. The glass transition temperature in 40% w/w is -135 ^oC and in 80% w/w is -124 ^oC. T_c however seems to be more dependent on the concentration, being -122 ^oC in 40% w/w Me_2SO solutions and it raises to -76 ^oC in 55% w/w Me_2SO.

From its discovery as cryoprotectant, Me_2SO has been widely used in cryopreservation and it is currently an essential component in almost all the cryoprotective solutions. In 1961 mouse bone marrow were cooled to -79 ^oC by use of Me_2SO as CPA by Ashwood-Smith (4). A year later, Dougherty (27) proved that Me_2SO had better cryoprotective actions than glycerol in cultured chick embryos fibroblasts. In 1963, Djerassi and Roy (26) cryopreserved succesfully platelets in liquid nitrogen using Me_2SO in combination with sugars. In 1965 Farrant (40) developed a method to cool smooth muscle to -79 ^oC in presence of Me_2SO avoiding ice formation. It has been also used to study cardiac cryopreservation, with heart (117) or myocardium (58). In 1973, canine bowel segments with Me_2SO as CPA were stored in liquid nitrogen for seven days and recovered after thawing by Hamilton. In 1989, Taylor et al. (125) studied the kinetics of permeation of Me_2SO in corneas. Me_2SO was also the CPA elected in successful cryopreserverd tissues the last decade, such as vascular tissue by Song (122), vitrification of mouse ovaries, in 2003, (82) or the cryopreservation of cartilage by the Liquidus Tracking in 2006 (94 to 97).

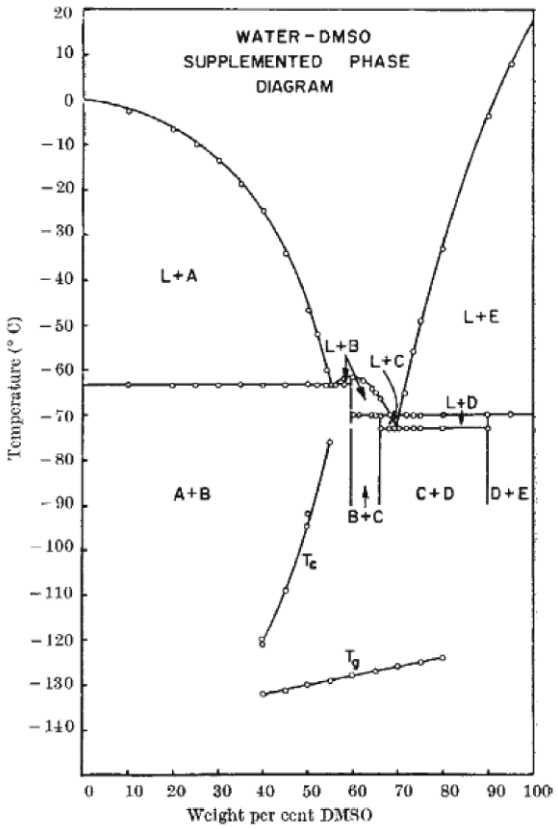

Figure 2.13. Phase diagram of the system Water-Me_2SO. From ref (104)

Moreover, Me_2SO is present in most of the vitrification solutions used by the group of Fahy. VS4 and VS1 (36) had MeSO as principal CPA together with formamide and 1,2-propanediol in VS4 and acetamide, 1,2-propanodiol and poliethyleneglycol in VS1. VS1 permitted Rall and Fahy to vitrify mouse embryos in 1985 (101). Many other mixed vitrification solutions were studied by Fahy et al. with Me_2SO as the CPA with the highest concentration, such as VMP or M22 (37). The famous solution M22 was used in the successful surviving rabbit kidney after transplantation (39). Some of these solutions permitted also the cryopreservation of some tissues, e.g., VS1 was used by Sugimoto et al. (124) to vitrify rat ovaries in

2000, and sheep ovaries were vitrified using VS1 and VS4 by Courbiere et al. in 2005 (21) and using VS4 by Baudot et al. in 2007 (7).

On the other hand, Me_2SO is also the most widely CPA used in oocytes and embryos vitrification, and it is normally used in solutions with same proportions of ethylene glycol combined with sugars, e.g. Vajta (127), Kuwayama (65) , Eroglu (31) or (Bonetti 13) among others.

As we have seen, Me_2SO as cryoprotectant has been widely used and it is still important nowadays. Our measurement concentration method is only useful for Me_2SO, which reasons will be explained in the following chapter.

3. CT functioning. Physical principles of X-rays.

Since our method of CPA concentration measurement is based on X-ray computed tomography (CT) imaging, we will introduce some of its basic physical principles in order to better understand the functioning of a CT device, and especially the effects that makes Me_2SO visible as opposed to other CPAs.

X-rays are the electromagnetic radiation in the range from approximately $3x10^6$ Hz to $3x10^{19}$ Hz of the spectrum (i.e., energies between 120 eV and 120 KeV). From 12 KeV on, the penetration properties of this radiation make it appropriate to the study of living tissues.

3.1. Attenuation.

When a beam of X-rays penetrates a substance, the intensity *I* of the beam at a distance *d* from the surface is reduced according to the following equation (63):

$$I = I_0 \exp(-\mu / d) = I_0 \exp(-(\mu/\rho)\,\rho\, d) \quad [1]$$

where I_o is the intensity of the initial beam, μ is a characteristic of the material called attenuation coefficient and ρ is the mass density of the material. The constant μ/ρ is called mass attenuation coefficient of the

material, which does not depend on its phase. This attenuation can be due to different physical processes, being the main ones:

- the coherent attenuation (Raleigh)
- the incoherent attenuation (Compton)
- the photoelectric effect
- the par production
- the photonuclear effect

The relative importance of these processes is given by the cross section σ and it depends on the energy. The cross section and the mass attenuation are related by:

$$\sigma = \mu/\rho \text{ u } m_a \quad [2]$$

where u is the mass atomic of the element and m_a the mass unit.

The par production only occurs at energies higher than 1.022 MeV, and the photonuclear effect takes place from energies of 5 MeV on. Since in our device the maximum energy used is 75 keV, none of these effects will occur. In our experiments only the three first effects will occur, although the coherent scattering will have a minimum effect, as we will see later. Therefore, we are going to explain briefly the principles of the incoherent attenuation and the photoelectric effect. The relative importance of them will be explained in the next section.

Attenuation values are normally expressed in Hounsfield Units (HU), which normalizes the values using water as reference according to the following expression:

$$HU = 1000\,(\mu_x - \mu_{agua})/(\mu_{agua} - \mu_{aire}) \quad [3]$$

3.1.1. Compton Scattering.

Compton scattering is a physical process of interaction between electromagnetic radiation and matter where a photon interacts with an electron giving it part of its energy. This energy is converted in kinetic

energy of the electron (see Fig.3.1). This effect basically occurs at medium energies of the photon.

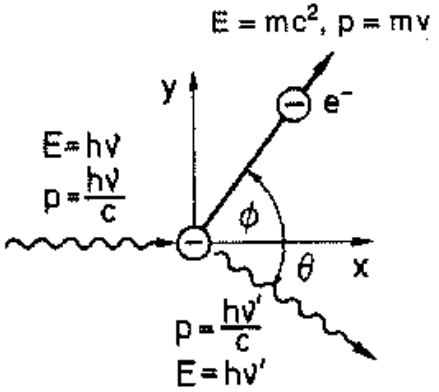

Figure 3.1. Compton Scattering. From ref (63)

3.1.2. Photoelectric Effect

Photoelectric effect is the physical process by which an atom completely absorbs a photon and an electron of the atom is excited to a higher level or ejected of the atom (see Fig.3.2). This effect occurs mainly at low photon energies.

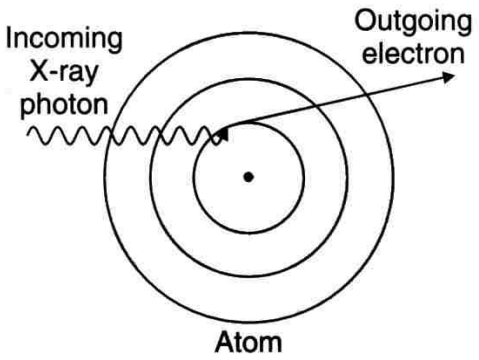

Figure 3.2. Photoelectric effect. From ref (63)

3.2. CT functioning.

The CT device is based on the measurement of intensity lost through different directions in the target, which permits to reconstruct the attenuation factor in the whole volume thanks to computational reconstruction techniques. The attenuation factor allows us to identify the material at each point. For instance, in table 3.1 there is a list with the typical attenuation values in different mediums.

Medium	Attenuation (HU)
Air	-1000
Fat	-120
Water	0
Muscle	40
Bond	400

Table 3.1. Attenuation (HU) of different mediums. From ref (63)

In the simplest CT device, the measurements are made in parallel planes separated by a small distance. There exist other helicoidal models which permit a better 3D reconstruction.

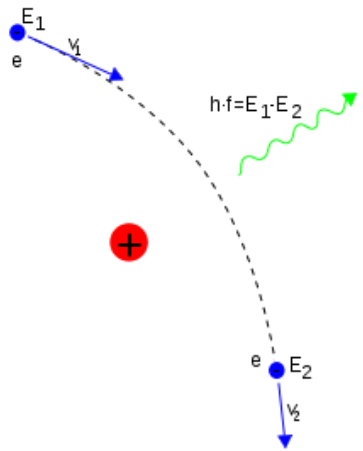

Figure 3.3. *Bremstrahlung* effect. During the acceleration process a photon is emitted

In CT devices, X-rays are produced by means of the *Bremstrahlung* effect. Electrons go out from a filament and are accelerated by a disc (target) through a differential of potential (65 or 75 kV in our case). When electrons go through the target, the *Bremstrahlung* effect is produced, which consists on the emission of radiation (X-rays) due to the acceleration of the electrons when they pass near the atoms of the target (Fig.3.3)

The X-rays emitted are distributed in a continuous spectrum. For a typical medical CT with an acceleration voltage of 120 kV, the typical energies of interaction are from 50 to 60 keV. In our case, with a maximum energy of 65 or 75 KeV, it corresponds approximately to 20-30 keV (112).

There are also some peaks in the emission spectrum due to the electronics levels of the material which the target is made of (L and K lines). However we have found that in our specific case these peaks do not contribute substantially to the results of our study and are therefore ignored for simplification in the following.

3.3. Scattering effects of different CPAs.

In the preliminary experiments, we introduced samples of four of the most common CPAs in the CT device (1,2-propanediol, dimethyl sulfoxide, ethylene glycol and glycerol) in a saline solution (PBS, phosphate buffered saline). The only case where the different CPA concentrations were distinguished and also different from water was with Me_2SO.

In this section we are going to explain why Me_2SO has a measurable signal in CT while no other CPA does it. Firstly, we are going to find the scattering effect predominant in our experiments, among the coherent attenuation (Raleigh), the incoherent attenuation (Compton) or the photoelectric effect.

The Rayleigh scattering is important when the dimensions of the target are much smaller than the wavelength. For our energies, the wavelength is approximately from 0.2 Å y 0.6 Å, and the molecules of the target are about several Å, so this effect is not going to be predominant. Regarding Compton scattering, the probability is proportional to $1/E^3$, whereas the photoelectric effect is proportional to 1/E (112). Since the energies we use are relatively

low, the photoelectric effect is going to be our predominance effect. This can be seen in Fig.3.4, where the graph is calculated from the NIST database (9) for a solution of 70% v/v Me_2SO in water. In the graph, it can be observed that for the region of our energy used, 20-30 keV, the greater mass attenuation is due to the photoelectric effect, although Compton scattering is also important.

On the other hand, Compton scattering depends mainly on the density, and most CPAs have similar densities and also similar to water. This would make the visualization of the CPAs concentration difficult. However, in the photoelectric effect, the cross section has dependence on Z^{α}, with Z the atomic number and α a number between 4 and 4.8 (112). Thus, the presence of the sulfur atom (Z=16) in the molecule Me_2SO increases the mass attenuation, making the concentration of this particular CPA measurable, compared to the other CPAs. Molecular compositions of other CPAs include only carbon, hydrogen and oxygen, all of them with a lower Z than the sulfur atom. This effect is showed is showed in Fig.3.5 for different CPAs, calculated from the NIST database (9). The mass attenuation is represented in our energy range, for different CPAs in concentrations of 5% v/v and 70% v/v in water.

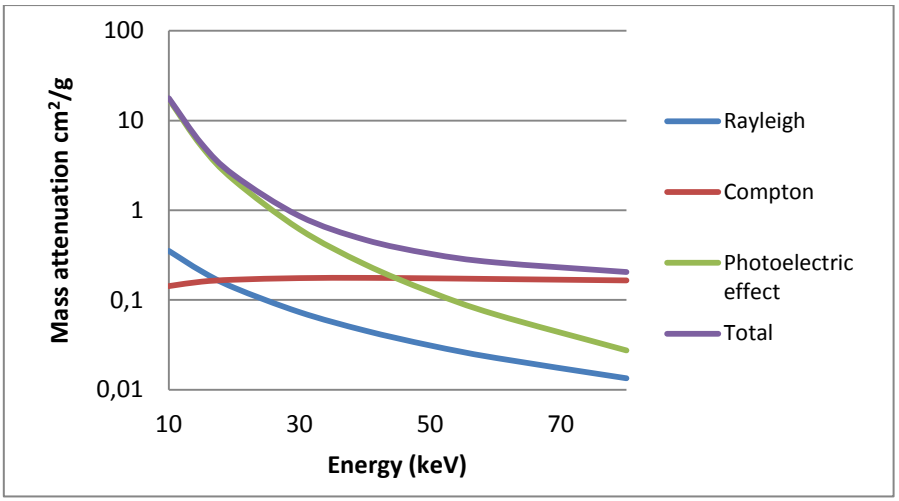

Figure 3.4. Dependence of the mass attenuation (cm^2/g) on the X-ray energy (keV) for different scattering effects, for a solution of 70% v/v Me_2SO in water. Our work energy range is around 20 to 30 keV. Data from NIST database (9)

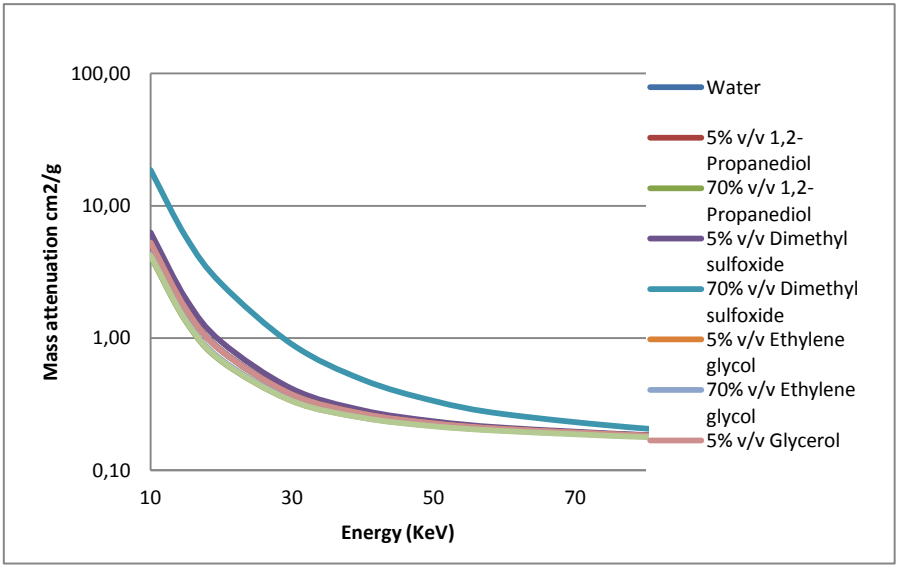

Figure 3.5.Dependence of the mass attenuation (cm^2/g) on the X-ray energy (keV) for 1,2-propanediol, dimethyl sulfoxide, ethylene glycol and glycerol, for concentrations of 5% v/v and 70% v/v in water. Our work energy range is about 20 to 30 Kev. Data from NIST database (9)

3.4. Ice detection.

The physical principles of why ice can be detected have been already exposed in the previous section. Since ice is pure water, and water is differentiated from Me_2SO, as we have already seen, ice should be differentiated of Me_2SO solutions too.

We have seen that Compton scattering depends mainly of the density on the sample to be imaged, although is not going to be the predominant effect it also participates in the global attenuation. To detect ice formation we need the samples to remain at temperatures at least below the freezing point of the water. Ice density is lower than water's, so in principle the attenuation of ice should be lower than the water's attenuation. Regarding Me_2SO solutions, density is going to change also with temperature, so the attenuation values are going to be slightly different to those values at ambient temperature. However, the attenuation between ice and different Me_2SO concentration will be still different enough to detect ice formation in Me_2SO solutions and tissues, as we will see later in our experiments.

4. Experiments: materials and methods.

In this section we are going to explain the materials and methods used to perform the experiments. The first sections describe the common part of the experiments, which consist of the CT imaging, where the CT device, the acquisition parameters and the imaging software used will be detailed, then there is a description of the solutions, the biological samples and the materials of the different containers used. Finally we will describe the cooling system used to cool the samples. Afterwards, we show a description of the experiments for CPA concentration measurements and ice detection. The experiments are classified into different groups. The last section of this chapter includes the description of the equilibrium vitrification method developed for future experiments, which combines the cooling system described here and the CT imaging method for measure the CPA concentration. The system is based on the Liquidus Tracking method developed by Pegg et al. (97).

4.1. CT imaging.

The CT device used for imaging is a NanoCT from Bioscan (Fig.4.1). It is located at the Centro Nacional de Aceleradores (CNA), Sevilla, Spain. The CT functioning has been described in Chapter 3.2. The main characteristic of this device is the use of low X-ray voltage (up to 75 kV) compared to the medical CTs (usually around 120 kV). It is normally used in medical

imaging research using animal experimentation (usually rats) for studies of diseases, mainly cancer.

Figure 4.1. Computed Tomography device from Bioscan

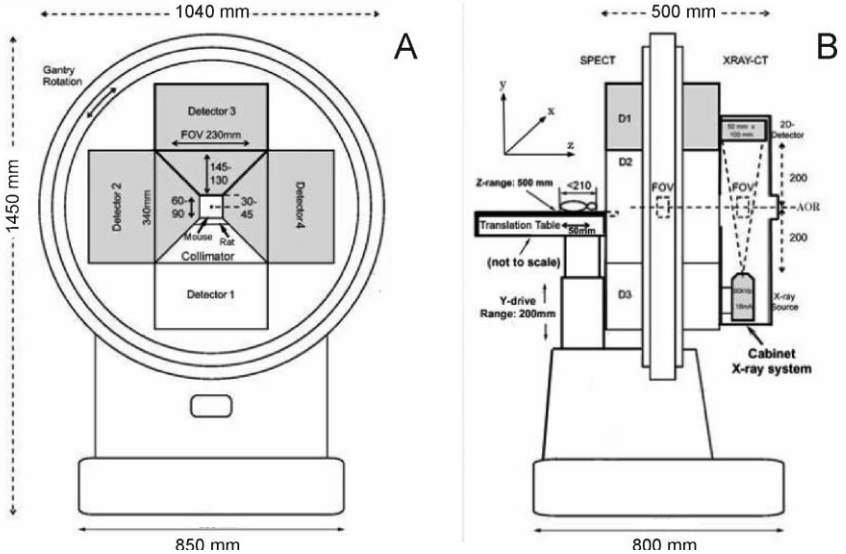

Figure 4.2. Front view (A) and side view (B) of the CT device with the main dimensions

One of the main limitations of the CT device is its small dimensions. Since it is used for animal experimentation, the dimensions are much smaller than the medical CTs. The CT bed is a mobile piece which introduces the samples inside the CT device. It has an outer diameter of 60 mm. This dimension is going to determine the dimensions of our containers and the cooling system, as we will see in the following sections. All dimensions of the CT device are showed in Fig.4.2.

Furthermore, in order to protect the CT device of the chemical compounds and the very low temperatures, we substitute the original CT bed by a cylindrical case of methacrylate, which has been built with the following dimensions:

- Outer diameter: 60 mm
- Thickness: 3 mm
- Length: 770 mm

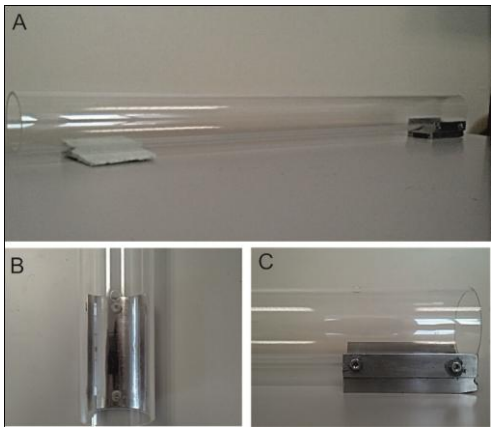

Figure 4.3. Methacrylate CT bed attached to the metallic piece which connects to the CT device

The methacrylate bed is attached to a metallic piece by means of two screws. Then the piece is inserted into the base of the CT device bed. The Fig.4.3.A shows the methacrylate bed attached to the metallic piece. Fig.4.3.B. and Fig.4.3.C are the top and the side view of the side of the methacrylate bed where the metallic piece is attached.

The images were acquired in NanoCT (Bioscan) with *Nucline* software and reconstructed with *IVS Image Processing* in Exact Cone Beam – Filtered Back Projection method at resolution ranging from 50 to 400 µm per pixel. Images were analyzed in *PMOD 3.3* software.

The acquisition parameters were kept practically the same for all the experiments, they were:

- X-ray voltage: 65 or 75 kV
- X-ray current: 123 µA for 65 kV and 106 µA for 75 kV
- 360 projections per rotation
- exposition time per projection of 1500 ms
- spatial resolution 200 µm, 100 µm or 50 µm

The voltage used for imaging and the resolution of the reconstructed image will be indicated for each experiment in the Chapter 4 and 5. The rest of parameters will only be indicated if they differ from those values mentioned above. Under these acquisition parameters the time needed for each experiment goes from 9 to 15 minutes, depending on the size of the sample and required resolution. For a rough estimation at 0.4 mm resolution, we can obtain satisfactory results in 3 min. However the acquisition of most of our images took 9 min and they were reconstructed in 0.2 mm

4.2. Solutions and biological samples.

Solutions:

All the aqueous solutions have been prepared with distilled water. The reagents have been purchased either from Sigma Aldrich or Panreac.

All the cryoprotectant solutions have been prepared in PBS (Phosphate Buffered Saline). PBS was prepared according to the following composition: NaCl 8 g/L, KCl 0,2 g/L, Na_2HPO_4 1,44 g/L, KH_2PO_4 0,24 g/L and adjusted to a pH=7.4.

The cryoprotective solutions were made with four of the most common CPAs in Cryobiology, which are, in increasing order of density: 1,2-propanediol, dimethyl sulfoxide, ethylene glycol and glycerol. Table 4.1 shows the density and molar mass for each CPA.

CPA	*Density* (Kg/m^3)	*Molar mass* (*g/mol*)
1,2-Propanediol	1040	76,10
Dimethyl Sulfoxide	1103	78,13
Ethylene Glycol	1113	62,07
Glycerol	1259	92,10

Table 4.1.1 Densities and molar mass of the CPAs used

Biological Samples:

The biological samples used in the experiments were rabbit kidneys. The kidneys used for experiments of sections 4.5 and 4.6 were obtained from a slaughterhouse. The kidneys were prepared for the experiments 24 to maximum 48 hours after the sacrifice of the animal.

The rabbit kidneys of the experiment described in section 4.7.5 are obtained from rabbit provided by the Agricultural and Forest Science Department of the Agro-Engineering School of Sevilla. The team of the Animal Production Area was responsible for the sacrifice of the animals according to their own protocols.

The average size of the kidneys were 35 mm of length, 25 mm of width and 20 mm of height (Fig.4.4).

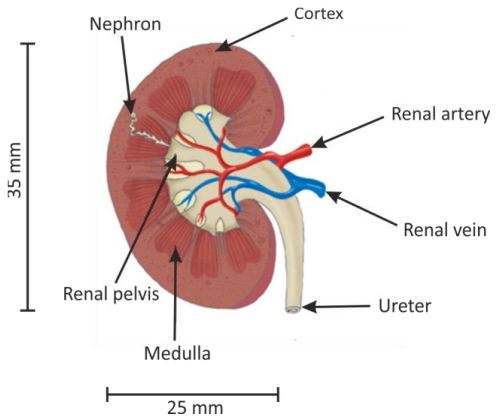

Figure 4.4. Average dimensions and main parts of a rabbit kidney

4.3. Materials and dimensions of the sample containers.

There are two conditions that are going to influence the selection of the material and dimensions of the sample containers.

The sample containers are going to be placed inside the CT device, thus, the material has to be transparent to X-rays, in order to avoid interferences in the images. Different tests were carried out with different materials. After that the materials selected were polypropylene (PP), polyethylene (PE) and polystyrene (PS).

The other constraint is the diameter of the CT bed, as we have already mentioned. The CT bed diameter is 60 mm, hence, the diameter of the containers has to be less than 60 mm. The selection of the container was different for each group of experiments, according to their needs. They will be indicated in the description of each group of experiments.

The different containers that are going to be used are: PS microplate of 200 µl wells from BD Falcon, 1.5 ml PP Eppendorf tubes, 2 ml PP Cryovials, 20 ml PP Falcon tubes, 30 ml PP vials from Vitlab, 30 ml PE vials from Nalgene and 50 ml PE vials from Nalgene.

4.4. The cooling system.

Some of the experiments in the CT device are at ambient temperature, however, we needed to cool samples in some of the situations, which are described below:

- in the experiments of CPA concentrations measurements, we performed some of the experiments at cryogenic temperatures, in order to assess the influence of the temperature in the X-ray attenuation of the samples.

- in detection of ice detection in vitrified samples, since samples must be cooled below the transition glass temperature to maintain them vitrified while the detection of ice.

- in the process of equilibrium vitrification, where samples are cooling while increasing the CPA concentration. In this case it is necessary a more rigorous control of the temperature, so the system is more complex. We will describe it at the end of this chapter.

In Cryobiology, one of the most commonly used cooling agents is liquid nitrogen. Liquid nitrogen has the advantage of its very low temperature at the liquid state, -196 ^{o}C. However there were two main constraints that do not let us to use liquid nitrogen straightly. The first one is the dimensions of the cavity and the CT device bed. The maximum volume of liquid nitrogen that the CT dimensions allowed was no sufficient and it evaporated before we could finish the experiment. We obtained blur and noise in the images as consequence of the liquid nitrogen evaporation. The other inconvenient is the possibility of damaging the CT device when being exposed to that extremely low temperature. Thus, we needed to build an alternative cooling system. We chose nitrogen gas as cooling agent, which is going to be pre-cooled with liquid nitrogen, as we will describe below. Fig.4.5 shows a scheme of the cooling system.

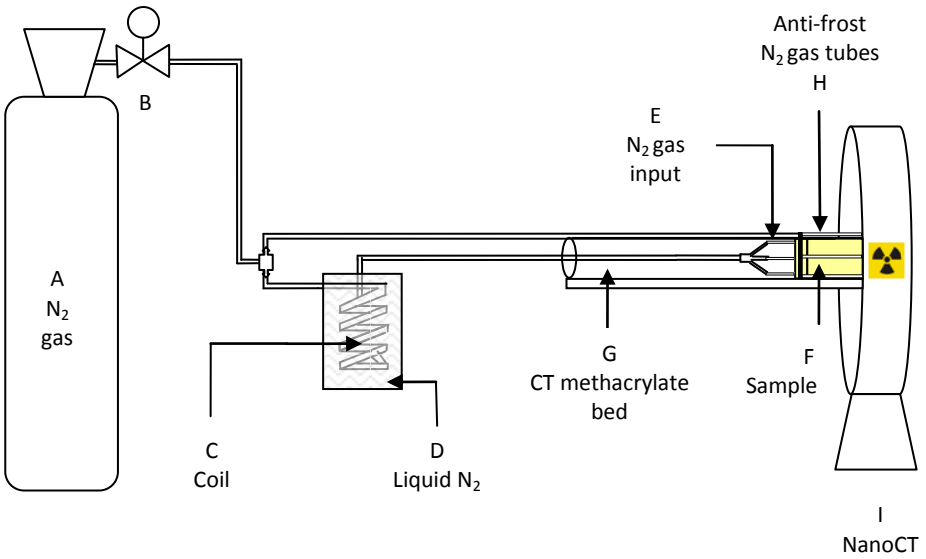

Figure 4.5. Scheme of the cooling system

The nitrogen gas comes from a pressurized tank (A). A pressure regulator valve (B) controls the flow of the nitrogen gas. The gas is sent through some polypropylene tubes to a cupper coil (C). The coil is immersed in liquid nitrogen inside a dewar flask of 2 L from Air Liquide (D). The cooled nitrogen gas goes through eight tubes of 1.5 mm diameter (E) into the insulating container which surrounds the sample container (F). A small fraction of the nitrogen gas, before being cooled, is used to create a dry atmosphere around the CT methacrylate bed (G) where the sample is. The nitrogen gas, at ambient temperature, is also divided in eight tubes of 1.5 mm diameter at the tip of the CT bed (H). In this way the formation of frost outside the CT bed is avoided, and therefore the possibility of any damage of the CT device by humidity. We will describe this anti-frost system in section 4.4.2. Finally, the sample is introduced inside the NanoCT device (I) to perform the measurements.

The Fig.4.6 shows a picture of the whole cooling system, where all the parts are named the same as the Fig.4.5.

Figure 4.6. Scheme of the cooling system. The red arrows show the nitrogen gas at initial temperature, the blue arrow shows the nitrogen gas pre-cooled with liquid nitrogen

4.4.1. Control of the temperature.

The temperature and the cooling rate of the system depend on the nitrogen gas flow. At the same time, the nitrogen gas flow depends on the outgoing pressure, which is controlled by the regulator valve (Fig.4.7). The nitrogen gas inside the pressurized tank is initially at 200 bars. It is necessary to achieve a trade-off between the cooling rate and the cost of the nitrogen gas. After different tests the work pressure selected for our experiments is from 0.5 bars to 0.7 bars. This pressure range corresponds to a nitrogen gas flow from 2 to 4 m^3/h.

Figure 4.7. Pressure regulator valve. The left barometer shows the pressure of the tank, the right one shows the gas outgoing pressure

The temperature is measured with a type K thermocouple, located inside the insulating container, and the data is logged by a TC-08 Temperature Data Logger from Picolog. The advantage of this data logger is that the temperature is registered each second, generating graphs and datasheets at the same time. Moreover it has 8 channels to connect up to 8 thermocouples, which allow us to measure the temperature in different points. This is very interesting in order to assess the homogeneity of the cooling process. In Fig.4.8, the picture shows the Picolog data logger connected to the computer, with two thermocouples whose hot junctions are placed inside the cap of the insulating container.

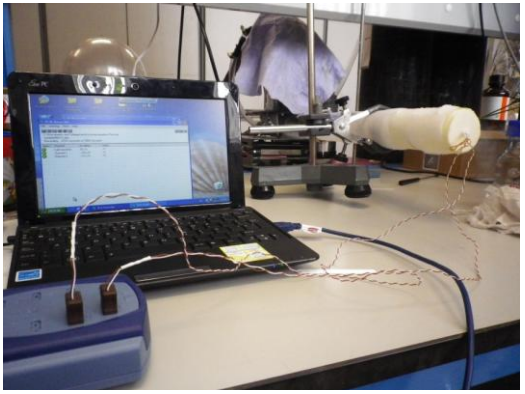

Figure 4.8. Recording of the temperature with the Picolog Data Logger during an experiment

We carried out different experiments in order to determine the time needed to achieve the desired temperature. The temperature we were interested in is a temperature below the glass transition temperature T_g. Although this temperature depends on the composition of the vitrification solutions and especially on the concentration, for the concentration we used this temperature is about – 120 ^{o}C, according to the literature (104). To make sure we were always below T_g and taking into account the different errors related to the measurement system, we decided to perform the experiments when the temperature was below -130 ^{o}C. To determine whether the system was able to achieve that temperature and the time needed to reach it, we placed two different thermocouples at the centre of the cap of the insulating container. Each thermocouple was located at a different distance of the cap. Another thermocouple was placed at the opposite side of the insulating container. Fig.4.9 shows a scheme with the location of each thermocouple.

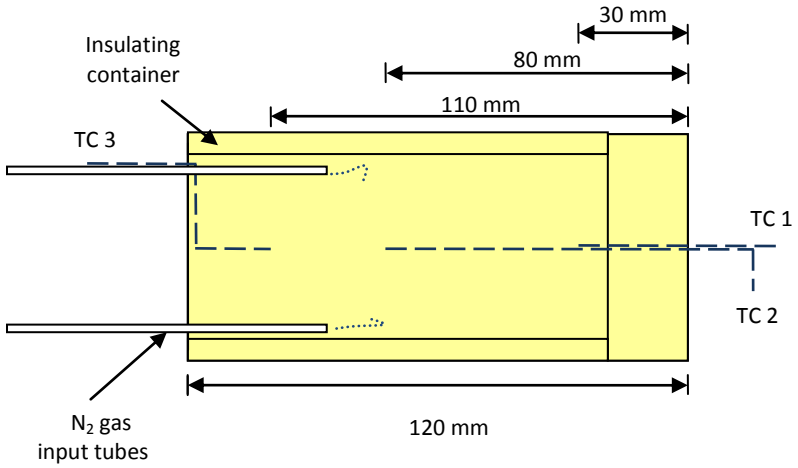

Figure 4.9. Scheme of the thermocouple locations for the control of the cooling process

After numerous tests of cooling processes of the equipment and samples, we are going to show following the temperature profile of the cooling processes chosen for our experiments.

Temperature profile of the equipment cooling.

In this cooling process, there were three thermocouples, Channel 1 corresponds to the thermocouple 1 from Fig.4 .10. (TC 1), Channel 2 to TC 2 and Channel 3 to TC 3. They were located inside the insulating container with no solution. The temperature of the cold junction is also registered during the cooling process. The outgoing pressure of the nitrogen gas is 0.7 bars. Note that the system goes below the -120 ^{o}C in less than 15 minutes, and it takes about 20 minutes to reach the temperature of -130 ^{o}C.

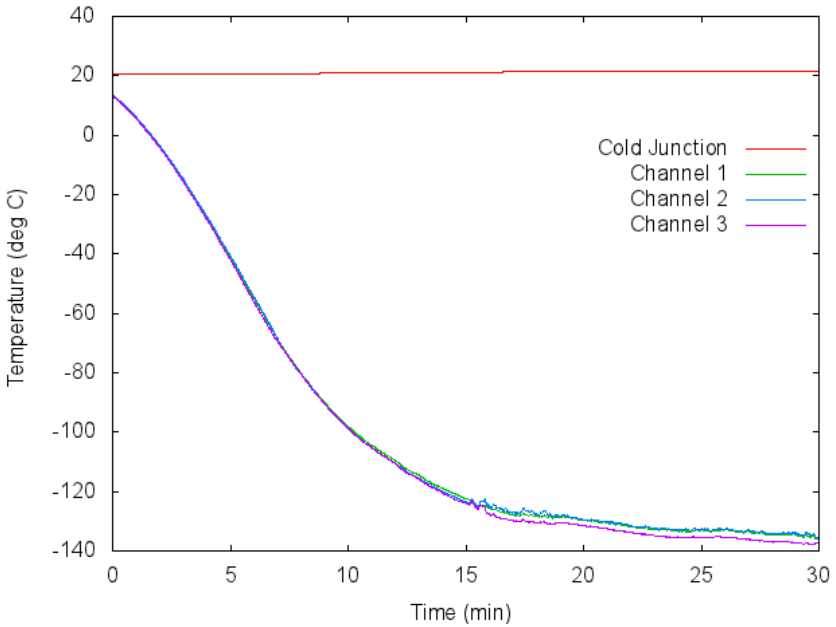

Figure 4.10. Temperature profile of the equipment cooling

Temperature profile of the cooling of a rabbit kidney by its immersion in liquid nitrogen.

We made other experiments to study the thermal properties of a rabbit kidney, in order to know how fast it cooled compared to the equipment and the solution. We were especially interested in the thermal inertia while warming. For that, we vitrify the kidney in liquid nitrogen while the system was being cooled below T_g. To record the temperature, we inserted one of

the thermocouples in the center of the kidney, as can be seen in Fig.4.11.A. Then the kidney was place in a container with a 50% v/v Me_2SO solution and another thermocouple was placed inside the solution (Fig.4.11.B). Fig.4.11.C shows the kidney and solution at some point of the rewarming. The system was not yet vitrified however the solution was still very viscous and sticky.

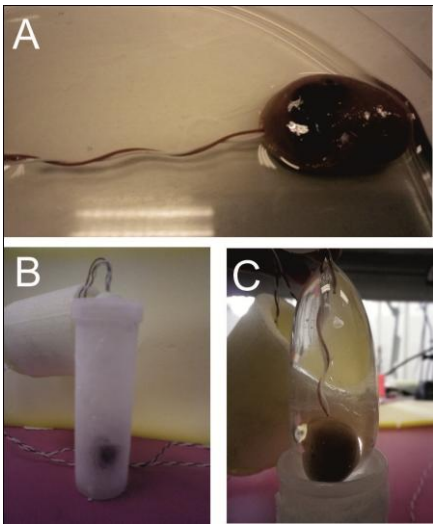

Figure 4.11. Study of the thermal inertia of a rabbit kidney

Afterwards, the container was placed in a dewar with liquid nitrogen and the temperature was recorded, as can be seen in Fig.4.12.

Figure 4.12. Cooling of a kidney in liquid nitrogen

Channel 1 was connected to the thermocouple inserted in the core of the kidney (TC 2), Channel 2 to the thermocouple inserted into the solution (TC 1). In the meantime, the equipment was being cooled too, using nitrogen gas at an outgoing pressure of 0,7 bars. The temperature was recorded at Channel 3 (TC 3). The cold junction temperature was also reordered. Once the kidney was vitrified and the system was cooled below -130 ^{o}C, we placed the container with the kidney into the equipment inside the insulating container, and stopped the nitrogen gas flow. The thermal inertia of the system, solution and kidney was recorded. The temperature profile is shown in Fig.4.13.

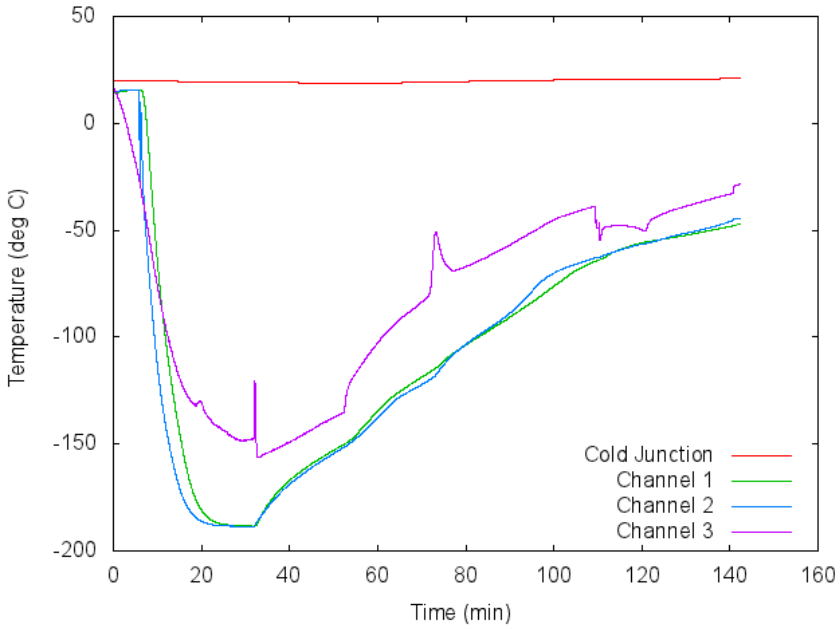

Figure 4.13. Temperature profile of a kidney immersed into a vitrification solution and cooled in liquid nitrogen. After vitrified, the kidney was placed into the pre-cooled system and rewarmed

At the moment where the container is placed into the system, the equipment's temperature drops (Channel 3), since the container is cooler. However after a few minutes the system begins to warm. While the solution seems to cool faster than the kidney, the difference is not

important, and during warming they show to have the same thermal inertia.

The problem with this way of cooling kidneys is that if we cool it so abruptly it is likely to fracture. These fractures are due to the difference of temperature in different points of the kidneys. Thus, we have also studied another way to cool the kidney. It consists of cooling it below its glass transition temperature but softly.

Temperature profile of the cooling of a rabbit kidney by the cooling system.

The first option was to cool the kidney inside the equipment, in a container with a 50% Me_2SO solution. The work pressure was initially 0.5 bars and once the temperature of the equipment reached -60 ^{o}C we increased the pressure to 0.7 bars.

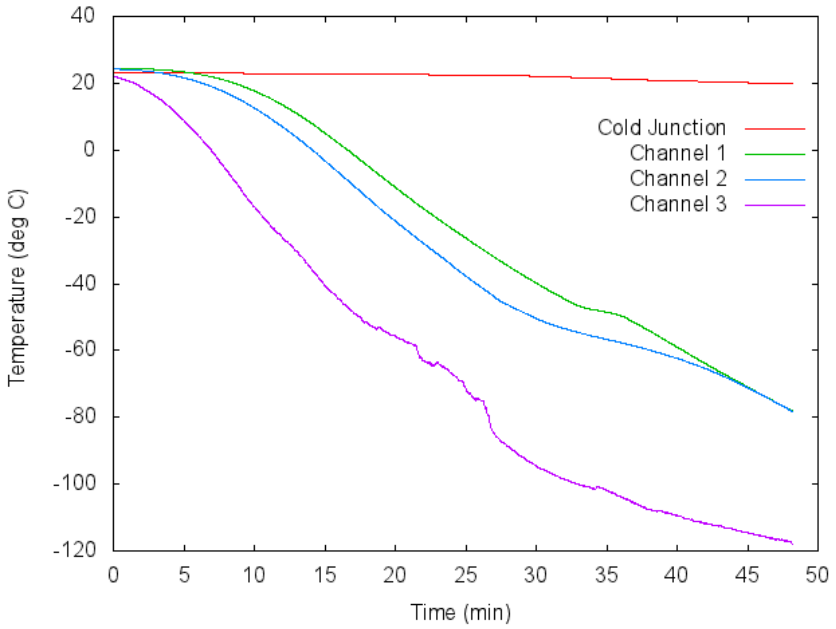

Figure 4.14. Temperature profile of a kidney in a 50% v/v Me_2SO solution placed into the cooling system

We recorded the cooling process (Fig.4.14), where Channel 1 was connected to the thermocouple inserted in the kidney (TC 2), Channel 2 recorded the temperature of the solution (TC 1) and Channel 3 the temperature of the equipment (TC 3). The graph also shows the cold junction temperature. It can be observed that the equipment cooled much faster than the kidney or solution, as expected. After 45 min the kidney did not reach the temperature of -80 ^{o}C, so we discarded this way of vitrifying the kidney because it was too slow and the cost of the nitrogen gas was too high.

Temperature profile of the cooling of a rabbit kidney by vapors of liquid nitrogen.

Another way of vitrifying kidneys is by using vapors of liquid nitrogen. For that, we placed a kidney in the container with the same solution and placed it in a big dewar with liquid nitrogen at a certain distance of the liquid nitrogen surface.

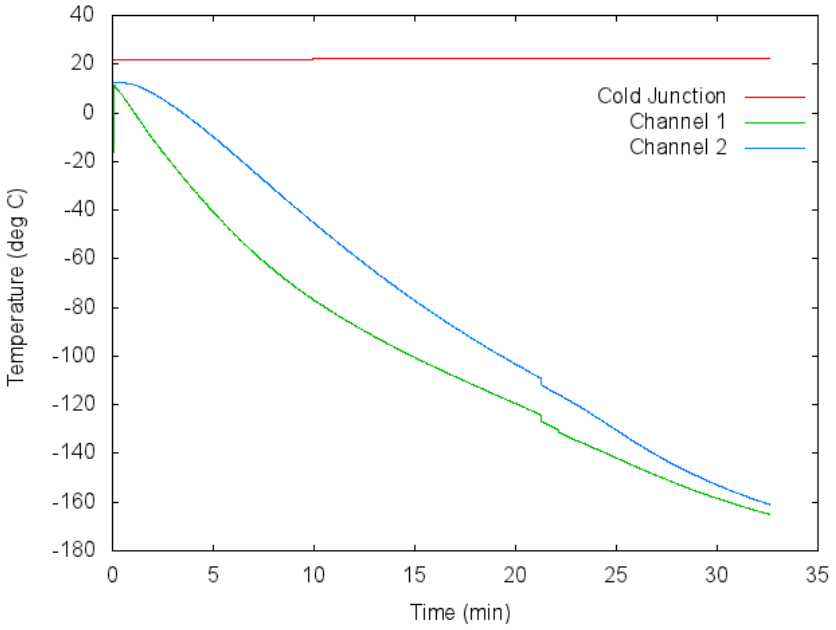

Figure 4.15. Temperature profile of a kidney in a 50% v/v Me_2SO solution cooled with vapors of liquid nitrogen

In this way, the kidney will be cooled with vapors which are at around -140 ^{o}C. In the beginning we placed the container with the kidney at 3 cm of the liquid nitrogen surface, and we recorded the cooling process. A thermocouple placed into the solution (TC 2), connected to Channel 1, and another thermocouple (TC 2) was inserted in the core of the kidney (Channel 2). The profile can be seen in Fig.4.15, where the cold junction is also showed. It can be observed that the kidney reaches the glass transition temperature in about 20 minutes, with a cooling rate around 5 ^{o}C/min.

4.4.2. Anti-frost system.

In the beginning of the cooling experiments, we realized that after a while there was formation of frost around the CT methacrylate bed, especially at the edge where the sample was (see Fig.4.16). This was a problem since that side was going to be introduced inside the CT device and it could cause problems with the condensation of the water.

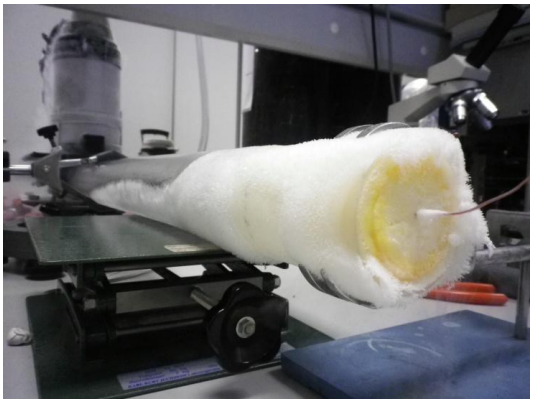

Figure 4.16. Formation of frost around the CT bed during one of the cooling experiments

In order to solve it we designed a system to create a dry atmosphere around the side where the sample was located. For that, we brought nitrogen gas at ambient temperature, through a tube, until the side of the sample. The nitrogen gas comes straight from the pressurized tank. The gas

is then divided in two ways (see Fig.4.5). One part of the gas is sent to the coil to cool the sample, and other part is used to prevent the frost, without cooling it (Fig.4.17.A). To create a dry atmosphere, we place a box around the tip of the CT bed (Fig.4.17.B). The nitrogen gas is spread through eight tubes of 1.5 m diameter around the CT methacrylate bed. We used a small valve to regulate the gas flow used for anti-frost (Fig.4.17.C). The position of the valve lets one quarter of the total gas flow through (Fig.4.17.D).

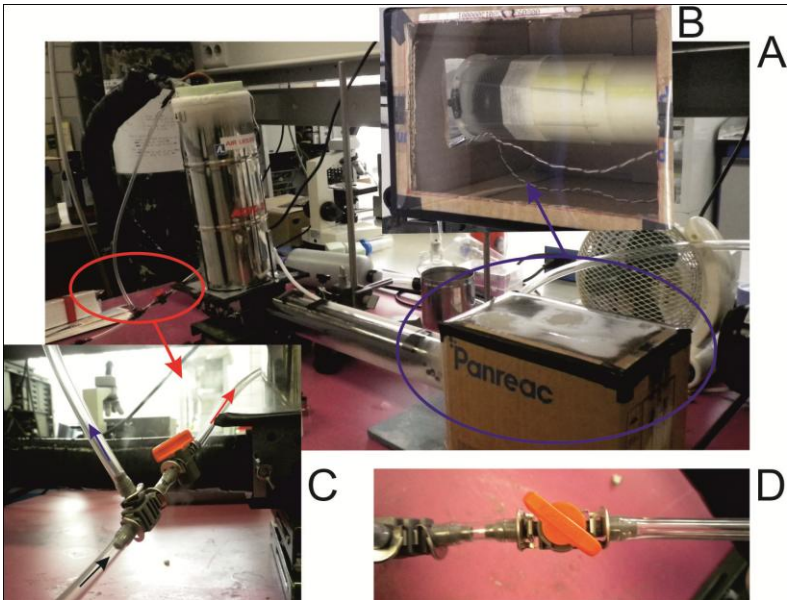

Figure 4.17. Anti-frost system. Detail of the valve to reduce the flow of gas used to avoid the frost

Fig.4.18. shows the result of the anti-frost system during one of the cooling tests. In Fig.4.18.A it can be seen the frost around the CT bed, and at the bottom the box where the dry atmosphere is created. Fig.4.18.B shows the output nitrogen gas tubes outside the dry atmosphere, thus some frost can be seen around the methacrylate bed. Fig.4.18.C shows the CT bed inside the box with the dry atmosphere. The frost has been avoided, and therefore the problem of water condensation around the CT bed.

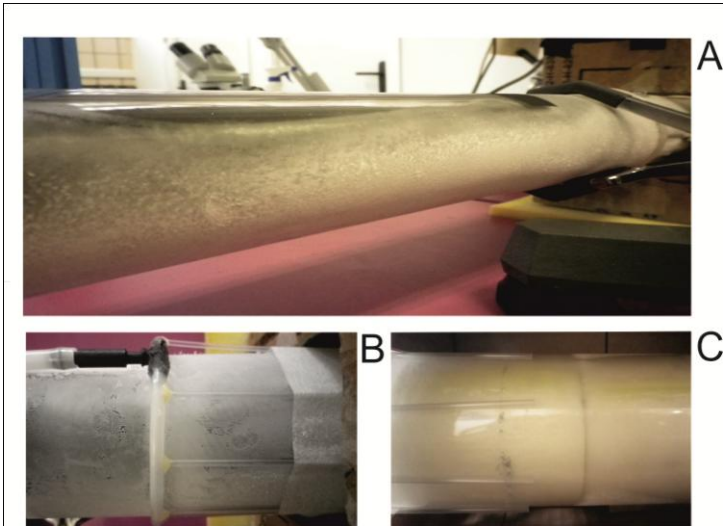

Figure 4.18. Anti-frost system

4.5. Experiments of CPA concentration measurement.

In this section we are going to describe the different groups of experiments related to the CPA concentration measurements. There are three different groups: in the first group, different concentrations of four different CPAs are measured; in group 2, we imaged different concentrations of Me_2SO solutions in different volumes and containers; and another group with rabbit kidneys immersed in different solutions of Me_2SO, equilibrated and not equilibrated with the concentration of the solution.

4.5.1. Group 1: comparison of different CPAs.

For the preliminary experiments we chose different concentrations of four of the most commonly used cryoprotectants: 1,2-propanediol, dimethyl sulfoxide, ethylene glycol and glycerol. The container for the solutions was a 96-well microplate from BD Falcon, made of PS. The plate was cut in a size of 45 microplate (9x5) in order to fit in our CT bed. In this way we were able to have all the different CPAs and concentrations in the same image. The plate was filled with 200 µl of each solution, in increasing order of densities in columns (water, 1,2-propanediol, dimethyl sulfoxide, ethylene glycol and

glycerol), and in increasing concentrations in rows (0% v/v, 5% v/v, 15% v/v, 30% v/v, 50% v/v and 70% v/v of the CPA in PBS). In the case of the water column all the samples were distilled water. The container was then placed at the CT bed and was imaged at 75 kV of acceleration voltage. The experiment was performed at 20 ^{o}C and -140 ^{o}C. For the experiment at -140 ^{o}C, the sample was cooled with the cooling system according to the protocol described at the previous section, Fig.4.10. The equipment was cooled for about 20 minutes with a gas pressure of 0.7 bars. A 3D view of the cooling system and dimensions of the microplate are shown in Fig.4.19.A. The cooled nitrogen gas enters through eight tubes (1) into the insulating container (2) where the microplate is (3). The nitrogen gas leaves the container through the cap (4). In Fig.4.19.B, there is a front view of the system and the dimensions of the insulating container. (5) marks one of the well of the microplate, where a sample of each solution is placed. Fig.4.19.C shows a view and dimensions of the nitrogen gas input tubes (1) inserted in the cap of the insulating container.

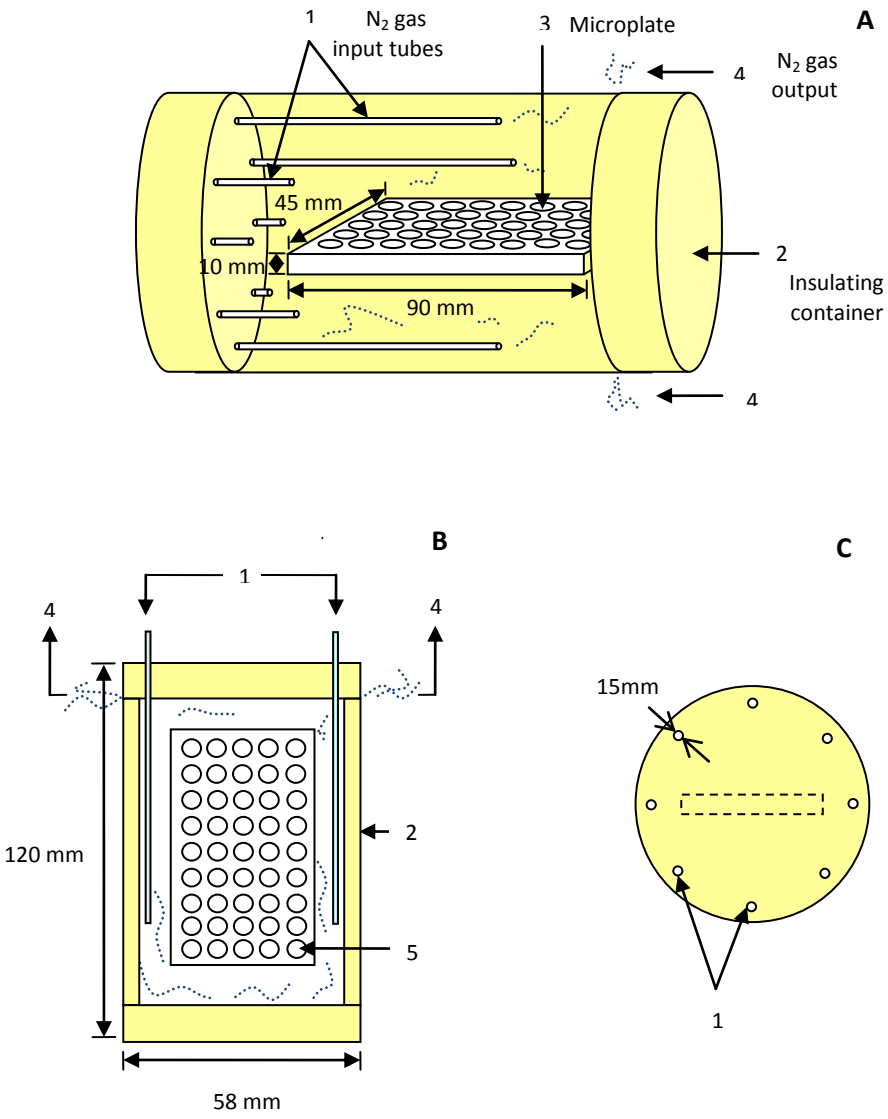

Figure 4.19. Detail of the cooling system of the microplate

Fig.4.20 shows the microplate at 20 °C (Fig.20.A) placed in the CT bed and ready to be imaged, and the microplate at -140 °C (Fig.20.B) after the measurement. Notice that in Fig.4.20.B some of the samples are frozen, except for the more concentrated in CPA.

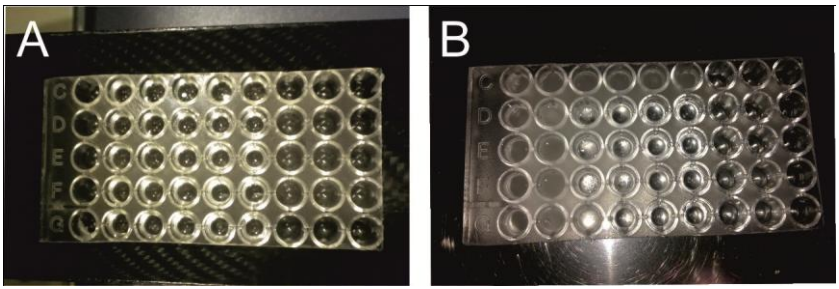

Figure 4.20. Microplates with different concentrations of CPAs at 20 and -140 °C

As we will see in Chapter 5.1, Me_2SO was the only CPA that showed measurable differences in the X-ray absorption for the different concentrations.

4.5.2. Group 2: comparison of different Me_2SO solutions in different volumes.

The aim of this group of experiments was to evaluate the differences among different volumes of different Me_2SO solutions. Two different containers were used in this group:

1.5 ml PP Eppendorf tubes: ten Eppendorfs were filled with water and Me_2SO solutions in PBS, in concentrations of 0M (PBS), 1M, 2M, 3M, 4M, 5M, 6M, 7M and 8M. The Eppendorfs were placed in the CT bed (see Fig.4.21.A), and the images were made at 75 kV, at 20 °C.

20 ml PP Falcon tubes: nine Falcon tubes were filled with Me_2SO solutions in PBS, in concentrations of 0% v/v (PBS), 10% v/v, 20% v/v, 30% v/v, 40% v/v, 50% v/v, 60% v/v, 70% v/v and 80% v/v. The containers were placed in the CT bed, as shown in the Fig 4.21.B. Three different measurements were necessary to image all the containers because of size limitations. The Falcon

tube with PBS was placed in all the measurements, in order to assess the reproducibility ot the results. All the images were made at 65 kV, at 20 ^{o}C.

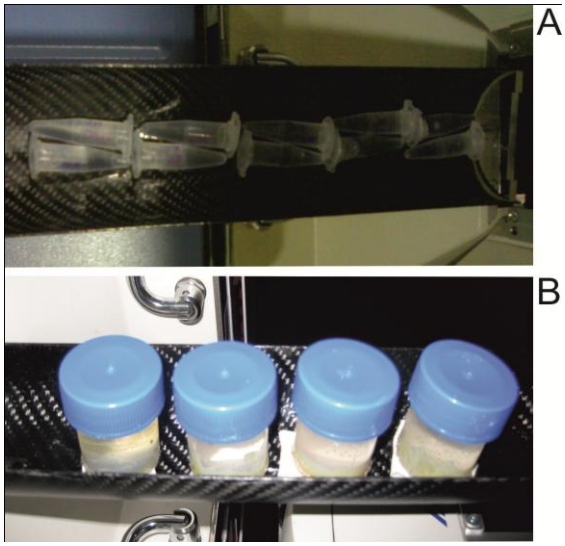

Figure 4.21. Eppendorf tubes (A) and Falcon tubes (B) with different solutions of Me_sSO placed into the CT bed ready to be imaged

4.5.3. Group 3: rabbit kidneys immersed in different Me_2SO solutions.

This group has as objective to study the X-ray attenuation inside tissues and to determine the differences between tissues and solutions. To that end, rabbit kidneys were immersed into different Me_2SO solutions in PBS: 0% v/v (PBS), 5% v/v, 30% v/v and 55% v/v, in 30 ml PP vials from Vitlab (Fig.4.22).

Two different groups of experiments were made with rabbit kidneys. For the first group of kidneys, the kidneys were not equilibrated with the concentration of the solution around. The images were obtained right after the immersion of the kidneys into the solutions, at 65 kV and at 20 ^{o}C .

For the other group, the kidneys were left to equilibrate with the concentration of the solution around for 9 days, at 4 ^{o}C. Hence, the

concentration inside the kidney was the same as the concentration of the outside solution. The kidneys were then imaged at 65 kV and at 20 ^{o}C.

Figure 4.22. Rabbit kidney in a container being placed inside the methacrylate CT bed

4.6. CT Ice detection experiments.

In this section we describe the different groups of experiments performed related to the detection of ice. There are five different groups: the first one, a preliminary study of piece of ice of approximately 2 cm^3 inside a Me_2SO solution; in group 2, a small sample of water (40 mm length of 200 µl diameter capillary) is immersed in different Me_2SO solutions; in group 3, the same capillary filled with water is immersed into a kidney equilibrated with a Me_2SO solution, group 4 consisted of kidneys with water of drops injected and cooled into liquid nitrogen, and in group 5, a kidney was cooled in vapors of liquid nitrogen and warmed progressively.

4.6.1. Group 1: piece of ice immersed in a 50% v/v Me_2SO solution, at -20 ^{o}C.

This first experiment was made in order to find out if ice could be differentiated from a Me_2SO solution. A 20 ml Falcon tube of PP was filled with a 50% v/v Me_2SO solution. The solution was then cooled to -20 ^{o}C in a freezer. Afterwards, a piece of ice of 1x1.5x1.5 cm^3 of ice was then introduced into the vial and the image was taken right after it. The acceleration voltage was 65 kV.

4.6.2. Group 2: 200 µm diameter capillary filled with water immersed in a 55% v/v Me_2SO solution, at 20° C.

In this group of the experiments we wanted to prove the capability to detect small samples of water in a concentrated Me_2SO solution. We performed several experiments in a similar way, although we are going to describe one of them whose result was the most relevant.

40 mm length of polycarbonate capillary of 200 µm outer diameter and 1.5 µm thicknesses was filled with distilled water. The two sides of the capillary were then heat-sealed, thanks to the fact that the capillary material is thermoplastic, as can be seen in Fig.4.23. Fig.4.23.A shows the phase of air-solution inside the capillary. One of the sides sealed is showed In Fig 4.23.B, and a profile view of the sealing is observed in Fig.4.23.C.

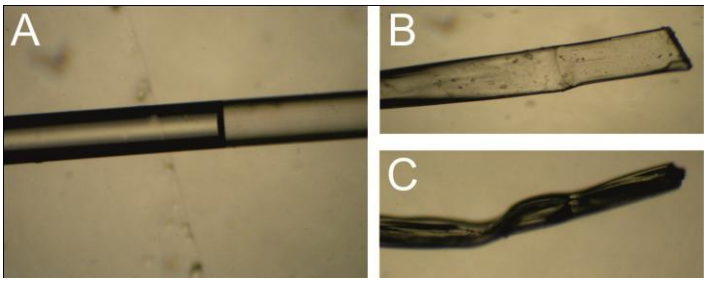

Figure 4.23. Detail of the sealing of the capillaries (magnification 40x)

Afterwards, the capillary was introduced in a 2 ml PP Cryovial with a solution of Me_2SO, at 20 °C. Fig.4.24 shows the cryovial laid on the CT bed. The image was then taken at 65 kV.

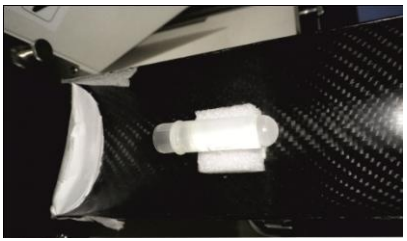

Figure 4.24. Cryovial in the CT bed

4.6.3. Group 3: 200 µm diameter capillary filled with water inserted into a kidney loaded with a 55% v/v Me_2SO solution, at 20 ^{o}C.

The aim of this experiment was to find out whether small samples of water could be detected inside a tissue. A kidney was introduced in a 30 ml PP vial from Vitlab with a 20% v/v Me_2SO solution in PBS and left to equilibrate for 72 hours. A polycarbonate capillary of 200 µm outer diameter, 1.5 µm thicknesses and 30 mm length was filled with distilled water and heat-sealed by the two sides. The capillary was then introduced in the kidney by means of a needle (Fig.4.25). The needle with the cateter was first introduced in the kidneys, (Fig.4.25.A), then the needle was taken out and the capillary was inserted (Fig.4.25.B), and finally the catheter was removed (Fig.4.25.C).

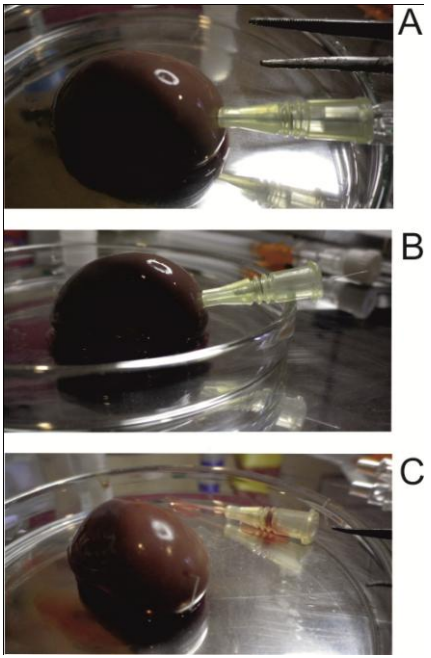

Figure 4.25. Process of the insertion of a capillary inside a kidney

The kidney was then placed in the same 30 ml PP container. A polystyrene piece of the same container diameter was introduced over the kidney in

order to fix its position (Fig.4.26). In this way the movements during the image are avoided. Afterwards the image was taken at 65 kV and at 20 ^{o}C.

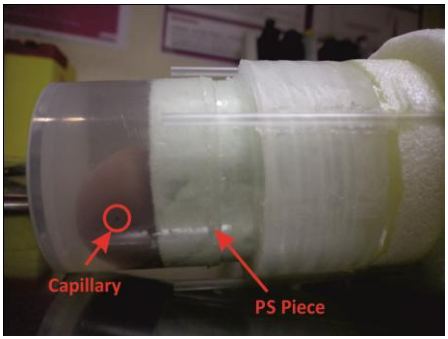

Figure 4.26. Kidney with the capillary inside the container before the CT measurement

4.6.4. Group 4: drops of water injected into a kidney loaded with a 55% v/v Me_2SO solution at -20 ^{o}C, and then cooled to -196 ^{o}C.

Three different kidneys were equilibrated with a 55% v/v Me_2SO solution in PBS in steps of intermediate Me_2SO concentrations and cooled to -20 ^{o}C in a 50 ml PE vial of Nalgene. Afterwards a 100 µL Hamilton syringe with 2 µL of precision was used to inject several drops of distilled water into the kidneys. The volumes of drops were between 2 and 8 µL and they were introduced in a line along the kidney. Fig.4.27.A shows the kidney before the drops insertion and Fig.4.27.B after the drops insertion. The kidneys were then introduced in the 50 ml PE vial with a 55% v/v Me_2SO solution and then cooled to -196 ^{o}C in liquid nitrogen during 30 minutes, following the cooling profile of Fig.4.13.

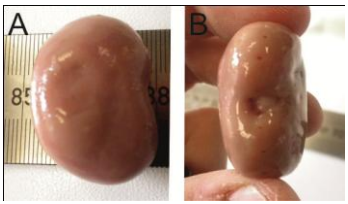

Figure 4.27. Image of the kidneys after introduction of water drops

In the meantime, the equipment was cooled until -140 ^{o}C, as described in Fig.4.10. Then the vial with the kidney was introduced inside the insulating container, as showed in Fig.4.28, and the image was taken.

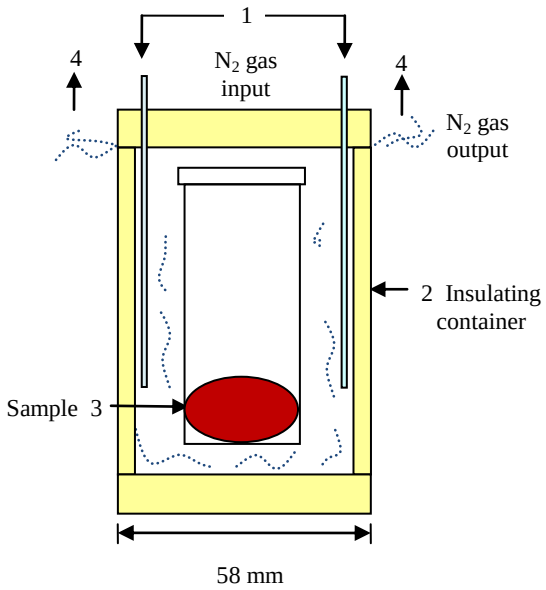

Figure 4.28. Scheme of a kidney to be cooled into the insulating container

In the following we describe the procedure in a more detailed way for each of the three kidneys: kidney A, kidney B and kidney C. As we said, the kidneys were equilibrated with 55% v/v Me_2SO solutions in several steps. The kidneys were immersed first in intermediate concentrations of Me_2SO solutions in PBS. This way, we avoided an excessive shrinking of the kidney due to the high gradients of concentrations between the solution and the kidney.

Fig.4.29 shows the images of rabbit kidneys after their immersion in different Me_2SO solutions for different periods of time. Notice that the more concentrated the solution, the more shrunk the kidneys are.

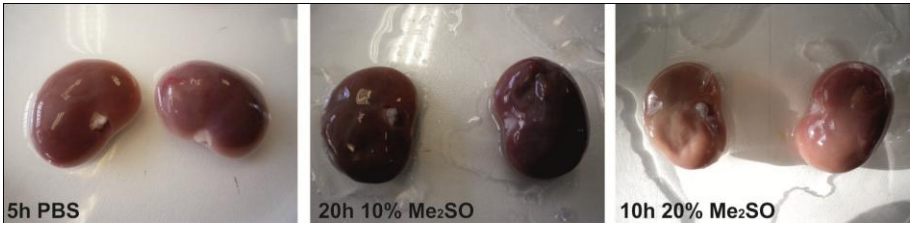

Figure 4.29. Images of rabbit kidneys after immersion in different solutions for different periods of time

The protocol of Me_2SO loading was not exactly the same for the three kidneys, although a minimum time of 5 hours was left between one step and the following. The kidney was normally stored at -20 ^{o}C until the experiment could be carried out.

Kidney A: the kidney was equilibrated with a 55% v/v Me_2SO solution, being introduced in intermediate concentrations in PBS for the following times:

- 10% v/v Me_2SO at 4 ^{o}C: 20 h.
- 25% v/v Me_2SO at 4 ^{o}C: 5 h.
- 40% v/v Me_2SO at 4 ^{o}C: 20 h.
- 55% v/v Me_2SO at 4 ^{o}C: 10 h.
- 55% v/v Me_2SO at -20 ^{o}C: 5 days.

Eight drops of distilled water were then inserted into the kidney with a needle of 21 G 1 1/2” (0'8 x 40 mm) from BD Microlance. The volumes of the drops, in the same order than they were introduced in a line were 2, 2, 4, 6, 8, 6, 4 and 2 µL. Afterwards, the kidney was cooled to -196 ^{o}C as described before and imaged at 75 kV.

Kidney B: the kidney was equilibrated with a 55% v/v Me_2SO solution, being introduced in intermediate concentrations in PBS for the following times:

- 10% v/v Me_2SO at 4 ^{o}C: 10 h.
- 25% v/v Me_2SO at 4 ^{o}C: 15 h.
- 40% v/v Me_2SO at 4 ^{o}C: 24 h.
- 55% v/v Me_2SO at -20 ^{o}C: 24 h.

After that, four drops of distilled water were introduced into the kidney with a needle of 21 G 1 1/2" (0'8 x 40 mm) from BD Microlance. The volumes of the drops, in the same order than they were introduced in a line were 4, 2, 2 and 6 µL. Afterwards, the kidney was cooled to -196 ^{o}C as described before and imaged at 75 kV.

Kidney C: the kidney was equilibrated with a 55% v/v Me_2SO solution, being introduced in intermediate concentrations in PBS for the following times:

- 10% v/v Me_2SO at 4 ^{o}C: 10 h.
- 25% v/v Me_2SO at 4 ^{o}C: 15 h.
- 40% v/v Me_2SO at 4 ^{o}C: 24 h.
- 55% v/v Me_2SO at -20 ^{o}C: 24 h.

After that, six drops were introduced into the kidney with a needle of 26 G 3/8" (0'45 x 10 mm) from BD Microlance. The volumes of the drops, in the same order than they were introduced in a line were 6, 4, 2, 4, 6 and 8 µL. Afterwards, the kidney was cooled to -196 ^{o}C as described before and imaged at 75 kV.

4.6.5. Group 5: kidney loaded with a 60% v/v CPA solution at -20 ^{o}C, cooled slowly to -140 ^{o}C in vapors of liquid nitrogen and then warmed up to 5 ^{o}C.

The kidney was loaded with a 60% v/v CPA solution. The CPA solution contains about 20% v/v Me_2SO among other CPAs. The kidney was then stored in the freezer at -20 ^{o}C in a 30 ml vial from Vitlab. After taking out the container of the freezer, we removed the kidney and cleaned the fat around the kidney. We removed the fat in order to obtain cleaner images, as we will see in Chapter 5. Then we put the kidney back into the solution, still at -20 ^{o}C.

The kidney was then cooled to -130 ^{o}C in liquid nitrogen vapors. The total time of this cooling process was 30 min, the profile temperature followed is showed in Fig.4.15. In the meantime, we cooled our equipment through pre-cooled nitrogen gas. The insulating container where the kidney was going to be placed for the image was cooled to -130 ^{o}C, according to

temperature profile of Fig.4.10. Then the kidney, in the original vial, was placed inside the insulating container in the CT bed, horizontally. A small sample of water was also placed inside the insulating container in order to have a reference value of ice. The temperature was registered with a thermocouple (TC 3) located at the opposite side where the kidney was inside the insulating container (Fig.4.30). Afterwards, the sample was imaged at -130 ^{o}C at 75 kV.

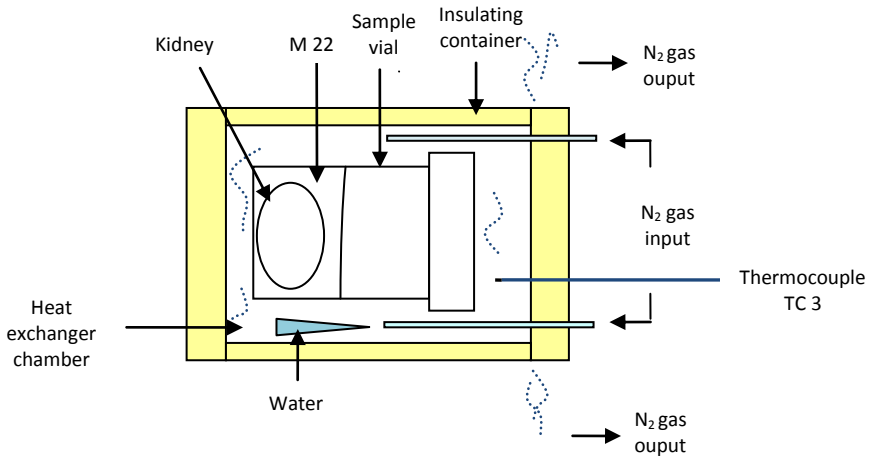

Figure 4.30. Scheme of the sample inside the pre-cooled insulating container

Then, we warmed the kidney progressively and imaged it at some points of the process. For that, we decreased the nitrogen gas flow. Firstly we lowered the outgoing pressure to 0.1 bars. When the temperature reached -55 ^{o}C the sample was imaged at 75 kV. The warming rate was around 2 C^{o}/min, according to data recorded. We wanted then to image the kidney at a temperature above 0 ^{o}C, so we closed the valve so that the nitrogen gas flow went to zero. We imaged the sample when the temperature was around 5 ^{o}C. The warming rate was around 3 ^{o}C/min.

4.7. Equilibrium vitrification.

The use of CT techniques for CPA concentration measurements and ice detection has multiple applications in Cryobiology, and it could be used as part of different cryopreservation processes for numerous biological systems. Due to the resolution of the images it has an especial interest in tissues and organs, where there is still a lack of successful cryopreservation methods. Our aim is to implement this technology to the equilibrium vitrification process to cryopreserve large samples. The equilibrium vitrification process consists of the following of the liquidus curve of a system maintaining the system always above the liquidus curve, as we have describe in Chapter 2. We have adapted the Liquidus Tracking system developed by Pegg et al. (97) to our necessities. Following there is a description of the equilibration vitrification system.

4.7.1. Equilibrium vitrification system: global scheme.

As we said, the equilibrium vitrification consisted of increasing the CPA concentration while decreasing the temperature of the system and maintaining always the sample above the liquidus curve, in order to avoid the formation of ice. Thus, we need to control two parameters, the temperature and the CPA concentration. For this purpose, we have programmed a software in Labview. While the temperature can be easily measured (e.g. by means of a thermocouple), the measurement of the concentration inside a large tissue is more complicated, especially its distribution. The main contribution to this method is the use of the CT technology to measure the CPA concentration and to detect the formation of ice.

The Fig.4.31 shows a global scheme of the equilibrium vitrification system. The upper part describes the control of the temperature. For the cooling process, we used the same cooling system described in section 4.4 is used (Fig.4.5), with a thermocouple to measure the temperature. However, we added two solenoid valves for the control of the temperature (description in section 4.7.4). The distribution of the CPA to the samples is made by two peristaltic pumps, one which will provide PBS and the other one the CPA (Me_2SO). The CPA concentration inside the organ will be measured by the CT device (section 4.7.4).

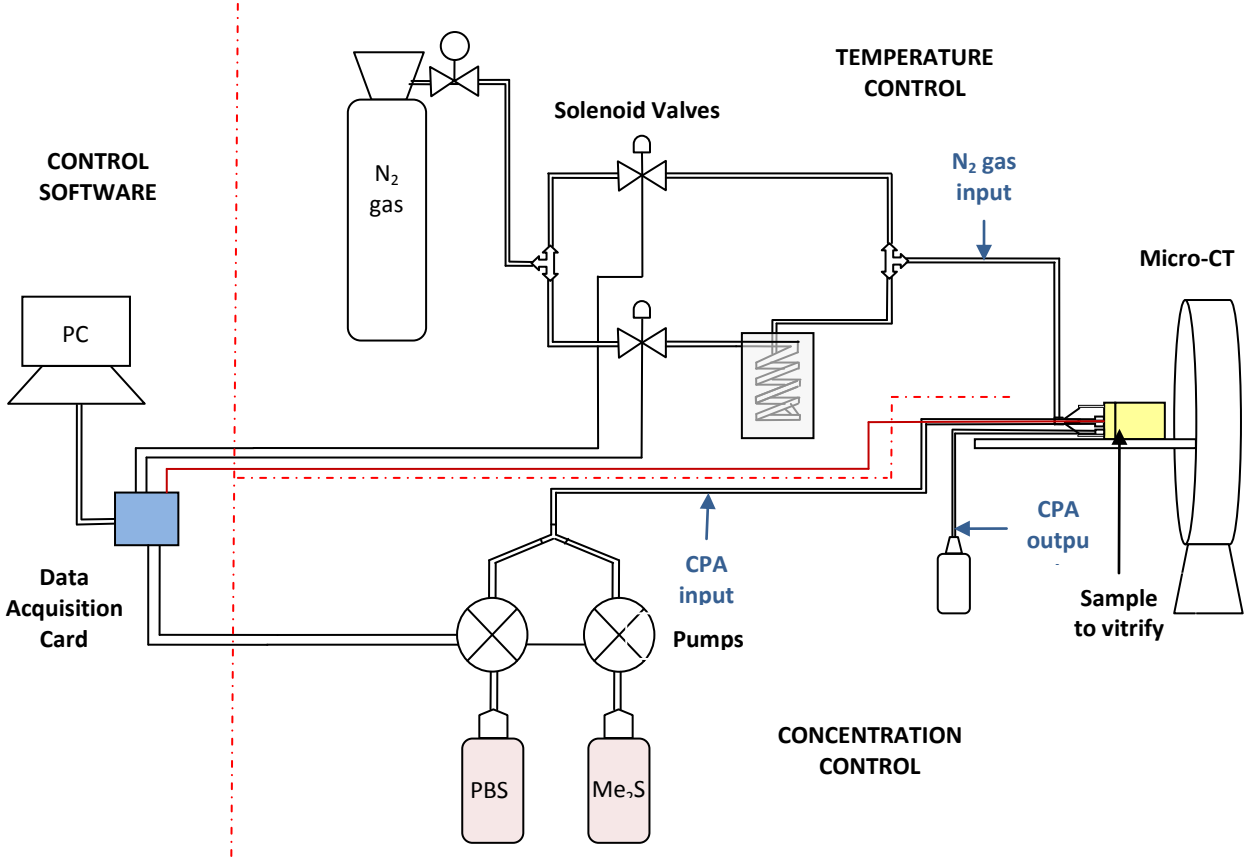

Figure 4.31. Global scheme of the equilibrium vitrification system

4.7.2. Software and data acquisition card.

As we have mentioned the software of control was programmed in Labview. The programming was made by one of the students of Dr. Risco's group (F.J. Yuste, 2008). Labview is a very easy programming language which uses a graphical interface (G language). Its main advantage is that lets a very easy integration with hardwares (e.g. measurement cards, data acquisition cards or data loggers). In our system, the card used is mainly designed to work with Labview and it includes some specific modules for data acquisition, data processing and output signals.

The Data Acquisition card used is a PMD-1208LS from Measurement and Computing. It has some analog inputs/outputs and digital ports. The connections that we have used for the different hardware are:

- thermocouple: one analog input,
- pumps: two analog outputs,
- solenoid valves: one digital port input.

The Fig.4.32 represents the different connections for the different part of the system. The analog outputs supply a maximum voltage of 5 V, so the pumps will receive a voltage from 0 to 5 V. However the analog inputs accept a voltage up to 10 V, which corresponds to the thermocouple. For the digital port, the solenoid valves, the voltage will be either 0 or 5 V.

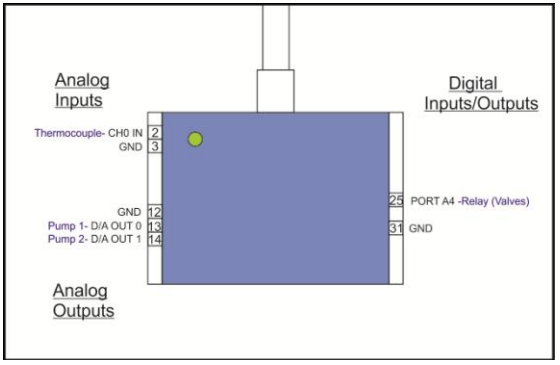

Figure 4.32. Different connections of the data acquisition card

The first step for the use of the software is the calibration of the thermocouple and the pumps. The software allows us to create different subroutines while programming. One of the subroutines reads the voltage of the thermocouple for a certain temperature (Fig.4.33.A). Then the subroutine voltage-temperature generates the function of the voltage versus the temperature (Fig.4.33.B).

In the case of the pumps, there is a subroutine where you introduce different voltages to the pumps (Fig.4.33.C). A higher voltage means a higher frequency of rotation of the pumps and therefore, a higher solution flow. Fig.4.33.D shows the subroutine that generates the function of voltage-flow.

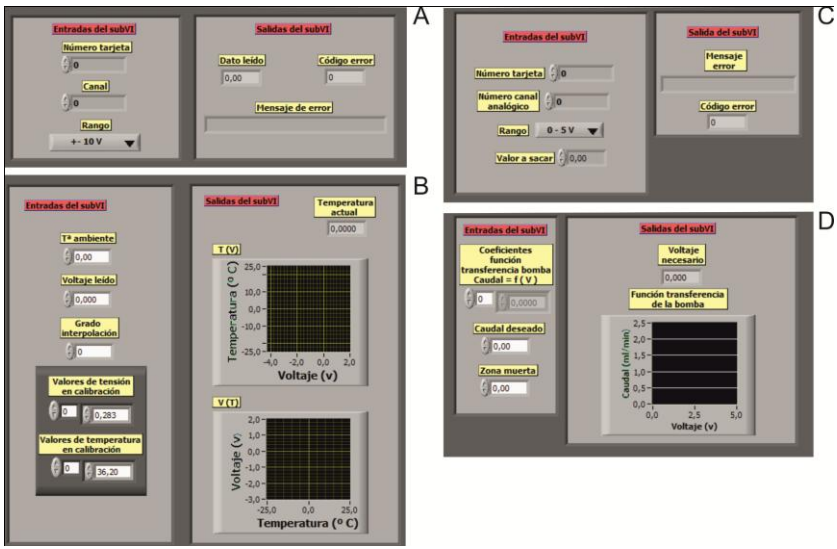

Figure 4.33. Labview subroutines for the calibration of the temperature (A and B) and the CPA flow (C and D)

Now the software is able to transfer the voltage to temperature and CPA concentration values. We remember these are the parameters we need to control, and they are related with the equilibrium curve of the system, in our case the Me_2SO liquidus curve (Fig.4.34).

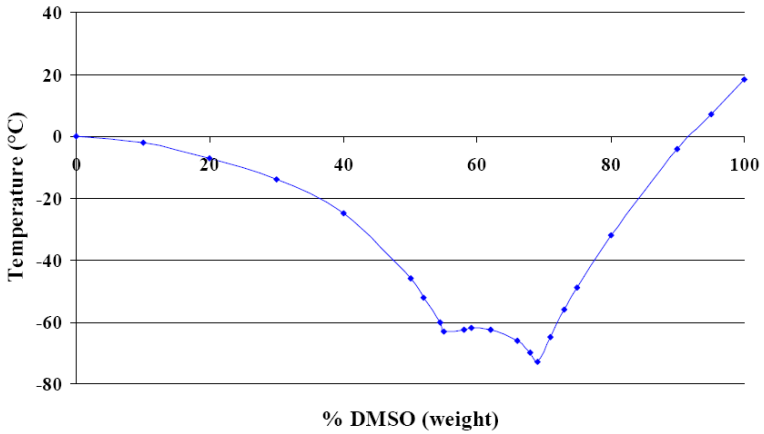

Figure 4.34.Concentration-temperature equilibrium curve of Me_2SO. Data from ref (104)

Introducing some points of the equilibrium curve in another subroutine (showed in Fig.4.35), the software will create the function of temperature and CPA concentration.

In this way, when the software reads a value of temperature, it uses the concentration-temperature function and sends the voltage necessary to the pumps to provide the flow according to the equilibration curves. In the following sections we will see how we control the temperature and the CPA concentration.

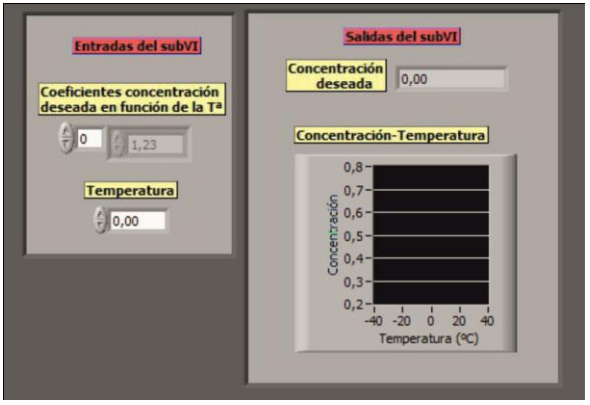

Figure 4.35. Labview subroutine of the curve concentration-temperature

4.7.3. Control of the temperature.

The equilibrium vitrification system has two processes: the cooling and warming processes. The software includes a subroutine (Fig.4.36) to indicate the cooling and warming rate desired. It asks you to insert the initial and final temperature of the process and the time needed for the process. The whole process can take place in several steps if necessary. The only condition is that the initial temperature of the warming process is the same as the final temperature of the cooling process. The image of that subroutine is shown in Fig.4.36.

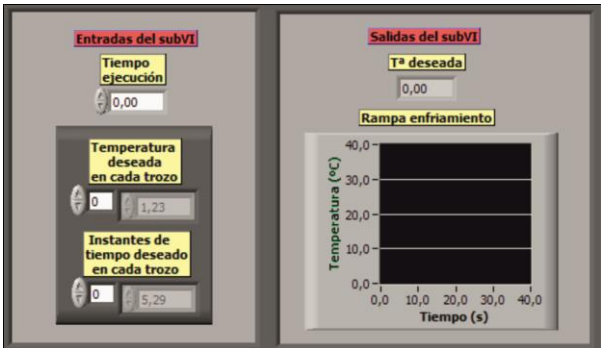

Figure 4.36. Labview subroutine of the temperature profile for cooling and warming processes

In this way the system will follow the previous profile of temperature introduced. The thermocouple sends the signal to the software through the data acquisition card.

Figure 4.37. Solenoid valve used for the control of the temperature

The cooling system is the same as described in section 4.4. Our cooling agent is going to be nitrogen gas pre-cooled with liquid nitrogen, however we added a warming agent (warm nitrogen gas) and control elements (solenoid valves, Fig.4.37).

The scheme of the temperature control system is shown in the Fig.4.38. The nitrogen gas comes from the pressurized tank and is divided into two flows. A solenoid valve is placed in each flow. One of them (lower) is sent to the coil with liquid nitrogen so it is going to be the cooling agent. The other one is sent directly to the input tubes around the sample container, at ambient temperature. This flow is going to be the warming agent. The solenoid valves and the thermocouple are connected to the data acquisition card, which sends the information to the computer (see also global scheme Fig.4.31).

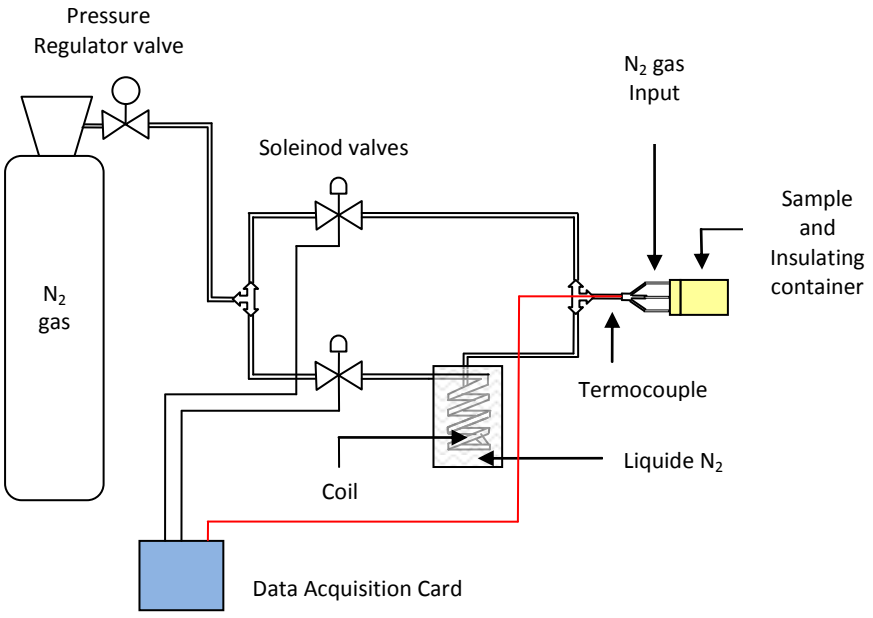

Figure 4.38. Scheme of the temperature control system

The two solenoid valves are activated by means of the same relay circuit. In this way, the two valves do not work at the same time. They need a power supply of 24 V AC so we needed a transformer too. The scheme of the circuit is shown in Fig.4.39. The relay circuit is connected between the power supply and the valves. The relay device works like a switch using an electromagnetic field produced by a coil powered with a direct current power source (6 V in our case). We have also added a transistor in the relay power circuit, which is directly connected to the data acquisition card in a digital port input. The relay has two different positions, one of them is normally connected or closed (NC) and the other one is normally opened (NO). When the transistor receives a signal from the acquisition card (5 V), the relay is powered and the circuit which is normally opened closes. We have connected the warm N_2 gas providing valve to the NO position and the cool one to the NC, in such a way that if the relay is not powered, the cold N_2 gas valve will be connected and vice versa.

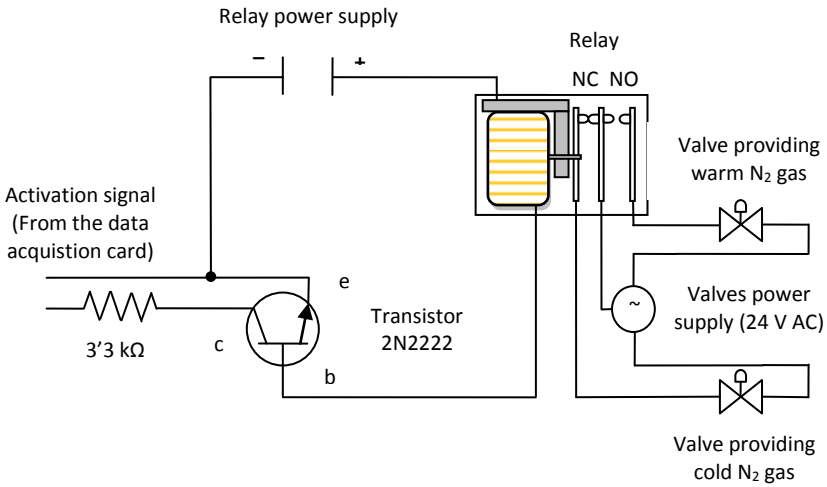

Figure 4.39. Scheme of the solenoid valves circuit and their connections to the data acquisition card

To summarize, the process is as following: the thermocouple reads the sample temperature (real temperature T_r) and sends the value to the software through the data acquisition card. The software compares that

temperature with the theoretical temperature (T_t) according to the temperature profile previously introduced in the subroutine. At the beginning of the cooling process, T_r (ambient temperature) will be higher than T_t, so the acquisition card will send 0 V to the relay power system and the cold N_2 gas valve will be opened. Once T_r is lower than T_t, the card will send the signal to power circuit (5 V), and the NO connector will close and the warm N_2 gas valve will be activated and the sample will warm, until T_r is again higher than T_t and so on. In this way the system will cool following the cooling rate fixed. The warming process will have the opposite functioning.

It is important to underline that during the CT measurement the thermocouple can not be inserted inside the sample. Thermocouples are made of metals and if we introduce metals in the area to be imaged the attenuation would be much higher for them and it could invalidate the images.

4.7.4. Control of the CPA concentration.

The CPA solution is sent to the sample by the impulse of two peristaltic pumps. This kind of pump consists of some rollers which rotate compressing the tubes through which the fluid passes. One of the main characteristics of these pumps is that the provided flow is variable. One of them will pump the CPA (Me_2SO) and the other one the solvent (PBS). The total flow (Me_2SO plus PBS) keeps constant during the process and is of 35 ml/min. The frequency of rotation depends on the voltage input and it can be controlled trough the data acquisition card. The pumps are connected to the acquisition card into the analogous outputs pins. The scheme of control system of the CPA concentration is showed in Fig.4.40.

Once the temperature is read by the thermocouple, the software will know the CPA concentration needed according to the temperature-concentration curve previously introduced (Fig.4.35), giving the voltage necessary for each pump. As the temperature decreases, the CPA concentration has to be higher, so the voltage to the CPA pump will increase and therefore the CPA flow, while the PBS flow will decrease, maintaining the global flow constant.

In this way we know the concentration sent to the sample. However in the case of large samples, we do not know when the sample has been equilibrated with the necessary CPA concentration. Thus a good system of perfusion is needed. Moreover, it is at this point when our main contribution is introduced, i. e. the use of the CT technology in order to measure the CPA concentration of each point of the sample with a resolution up to 50 µm. Since the images can not be connected directly to the software for the control of the CPA concentration, it will be necessary to perform experiments to relate the CPA concentration inside the sample with the temperature-concentration curve. Also the detection of ice during the process will allow us to modify the temperature profile of the cooling and warming processes in order to obtain an adequate protocol to vitrify large samples successfully.

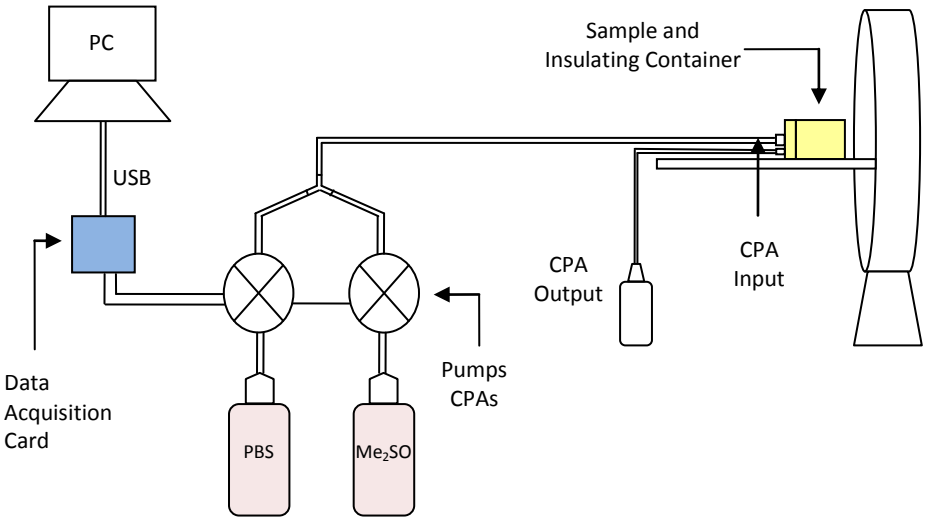

Figure 4.40. Scheme of the CPA concentration control system

The containers of the solutions are from polyethylene-terephthalate (PET), since this material can resist the corrosive Me_2SO solution. They have 100 mm of diameter and 160 mm of height. The residual solution container is a 70 mm diameter and 150 mm height PET container.

The tubes from the solutions are of nylon, which can also resist Me_2SO solutions and are flexible enough to handle them in the equipment. The diameter of the tubes from the solution containers to the pumps is 4mm and from the pumps to the sample and residual container is 6 mm. The total length of the tube system is 800 mm.

The introduction of the CPA into the sample depends on the sample to vitrify. In the case of organs, the CPA must be introduced by perfusion through the vascular system. We have created a system of perfusion for rabbit kidneys. Due to the big dimensions of the kidneys (Fig.4.3) in comparison with the limiting CT bed diameter (less than 60 mm), the best location of the kidney is as shown in Fig.4.41.

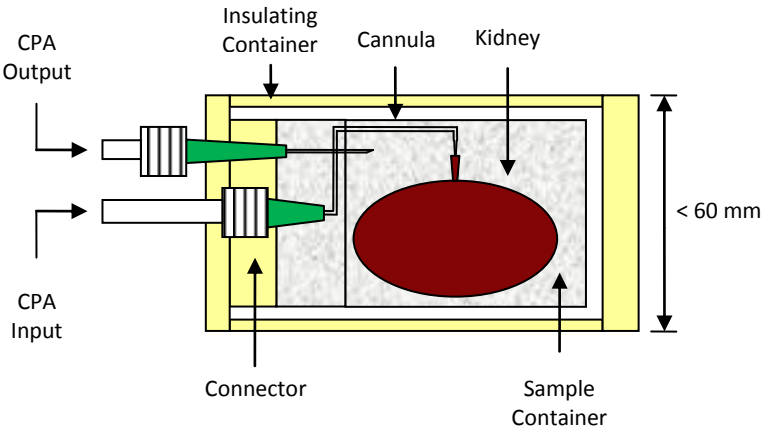

Figure 4.41. Scheme of the perfusion system for a rabbit kidneys

The container of the sample and the insulating container have to be cylindrical. The CPA input is produced by a needle in which a cannula has been attached. The cannula is introduced into the artery of the kidney. The vascular system will distribute the CPA inside the organ the same way it does with the blood. The remaining solution will go out by the vein into the container. The CPA solution will go out from the container by pressure through another needle and it will be recollected in another container.

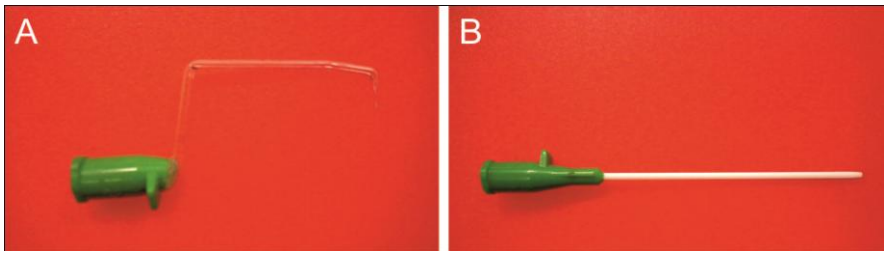

Figure 4.42. CPA solutions needles: (A) input and (B) output

The CPA solution input needle (cannula) is made with a glass hematocrit tube. We chose this material in order to avoid interferences in the CT measurements. Moreover, we needed a malleable material to make the appropriate shape represented in the scheme of Fig.4.41. The U shaped glass is made by heating the tube with a Bunsen burner. The tube is then attached to a connector of a catheter 18 G x 2" (51mm) from Abbocath-T, see Fig.4.42.A. The output needle is a the catheter 18 G x 2" (51mm) from Abbocath-T (Fig.4.42.B). The CPA input/output tubes are connected to the nylon tubes through plastic M 18 connectors.

4.7.5. Perfusion of a rabbit kidney with a Me_2SO solution, at 20 ^{o}C.

In this section we are going to explain the experiment of perfusion of a rabbit kidney with Me_2SO with the equilibrium vitrification system described above, at 20 ^{o}C. The kidney was imaged a three different points of the perfusion process: at the beginning, in the middle and at the end of the process. Due to complexity of this process, especially the providing and handling of the fresh kidneys, we only were able to perform one complete experiment of perfusion, and at ambient temperature. We describe it in the following.

Once the animal has been sacrified, the extraction of the kidney is made as fast as possible by cutting the renal artery, the renal vein and the ureter. The kidney is then placed in a plate with PBS at 4 ^{o}C. Afterwards, the kidney was washed with PBS in order to prevent the coagulation of the blood inside the vascular system. A cannula was introduced inside the artery and fixed with suture thread. Then the washing was made by injection of PBS through the vascular system at a constant pressure, which made the blood

to go out through the vein. The washing process took place until no more blood but only PBS was going out the vein. This is a very delicate process since the capillary are very narrow and can be damaged by overpressure. Moreover, the washing process has to be very quick to avoid the ischemia of the organ. The Fig.4.43 shows a picture of two kidneys, before and after the washing out of the blood. Then, the kidney was placed in a container with PBS at 4 ^{o}C and introduced in a refrigerator with ice for its transport to the place where the experiment is going to be performed.

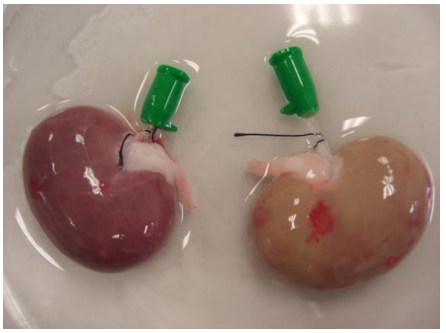

Figure 4.43. Rabbit kidneys before (left) and after (right) the washing out of the blood

Previously, the tubes of the perfusion equipment and also the sample container (30 ml from Vitlab) had been filled with a 20 % Me_2SO solution, which was going to be the initial concentration of the perfusion.

Once we arrived to the CT unit, the kidney was placed into a 20 ml PP Falcon tube, equipped with the perfusion system. The cannula is connected to the tip of the container. Fig.4.44 shows the container with the sample on the CT bed where the CPA input/output tubes are showed. Fig.4.44.A shows a profile view where the kidney can be observed and Fig.4.44.B shows the front view of the container and tubes. The CPA input tube (right) has a valve which is used to purge the system in case there is air inside it. The perfusion system differs from the one from the Fig.4.41. In this experiment the container was placed vertically. However we realized that the volume was to small compare to the size of the kidneys and we then designed the perfusion system described in section 4.7.4.

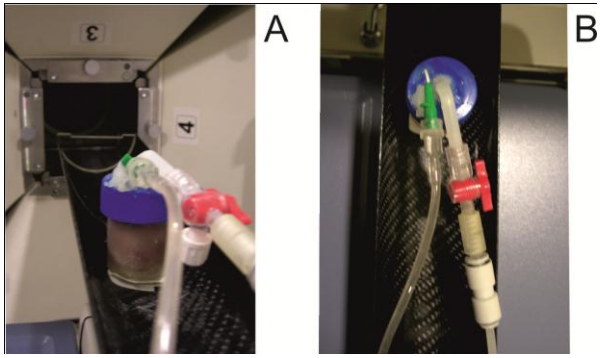

Figure 4.44. CPA input/output tubes for the perfusion of the kidney

The perfusion of the CPA was programmed in the equilibrium vitrification software, to be increased from 20% to 70% v/v Me_2SO in two hours and always at room temperature, 20 ^{o}C. The kidney is imaged at the initial point of the perfusion, after an hour of the process and at the end of the process. The acceleration voltage of the CT images was 65 kV.

Figure 4.45. Perfusion of a rabbit kidney with the equilibrium vitrification system, while CT imaging, at 20 ^{o}C

Fig.4.45 shows the perfusion process of the kidney while the container is prepared for a CT image. Part of the equilibirum vitrification system can be observed: the computer with the software running (A), the peristaltic pumps (B), the electronic circuits and acquision data card are packed in (C), the CPA carrying tubes (B), the sample laid on the CT bed (E) and the CT device (F).

5. Results and discussion

In this chapter we will present all the CT images obtained for the experiments performed for the CPA concentrations measurements and ice detection. We will also show the results of the perfusion experiment. We present also a few graphs which show the tendency of the attenuation in each situation. Moreover we will analyze and discuss all the results presented.

5.1. CPA concentration measurements.

In this section all the results related to the experiments of CPA concentration measurements are presented. These results are organized into the same groups that have been described in Chapter 4.5.

5.1.1. Group 1: comparison of different CPAs.

The aim of this group was to evaluate the attenuation values of different concentrations of four of the most common cryoprotectants. As we will see in this section, these results prove how the CT technology is an appropiate method to detect differences in CPA concentrations for the case of Me_2SO as CPA. Moreover these differences are also noticeable at cryogenic temperatures (-140 ^{o}C).

In Fig.5.1 we can observe the concentration of the different CPAs, at 20 ^{o}C. The color scale used to visualize the image is what we will call “cold scale”. It changes from dark blue for the lowest attenuation to intense red for the highest attenuation, which correspond to 0.0 to 3.0 CT values approximately. Fig.5.1.A shows a picture of the microplate with the samples in increasing order of density, from left to right: water (W), 1,2-propanediol (P), dimethyl sulfoxide (D), ethylene glycol (E) and glycerol (G). Fig.5.1.B shows the bottom view of the microplate, where samples appear in the opposite order than in (A), from top to bottom: 70% v/v, 50% v/v, 30% v/v, 15% v/v, 5% v/v and 0% v/v (PBS). The column of water (W) has water samples from top to bottom. The solutions are, from left to right: glycerol (G), ethylene glycol (E), dimethyl sulfoxide (D), 1,2-propanediol (P) and water (W). As we can see, the image shows how the differences in concentrations are only detectable in the case of Me_2SO (column D), with a different color for a different concentration. For the rest of the CPAs the color, or attenuation, maintains the same for each concentration and similar to the color for water. In Fig.5.1.C, the column of different concentrations of Me_2SO is selected (column D in Fig.5.1.B), from left to right: 70% v/v, 50% v/v, 30% v/v, 15% v/v, 5% v/v and 0% v/v (PBS). A clear gradient of color is observed: the more concentrated the solution, the higher the attenuation and therefore the more intense the red color. Fig.5.1.D shows the selection of the top view of the Fig.5.1.B. We can observe the highest concentrations of all the CPAs and water, from left to right: 70% v/v glycerol, 70% v/v ethylene glycol, 70% v/v dimethyl sulfoxide, 70% v/v 1,2-propanediol, in PBS, and water. This is the most favorable case to see any effect on the attenuation for each CPA. However, the image shows the color of all CPAs, except for Me_2SO, similar to water’s color, which corresponds to a low attenuation. Only in the case of Me_2SO the color, a red intense, represents a high attenuation. (1) marks one of the N_2 gas input tubes for the cooling process, inside the insulating container, however no gas was passing in this experiment. (2) marks one of the tubes used to prevent the formation of frost around the CT bed (3), although no gas was passing through the tubes, since the experiment was performed at room temperature. The voltage is 75 kV, the time of exposition is 1500 ms and the spatial resolution is 200 µm. Color bar scale is in CT units, from 0.0 to 0.3, which in this case corresponds to -1000 to 2000 HU.

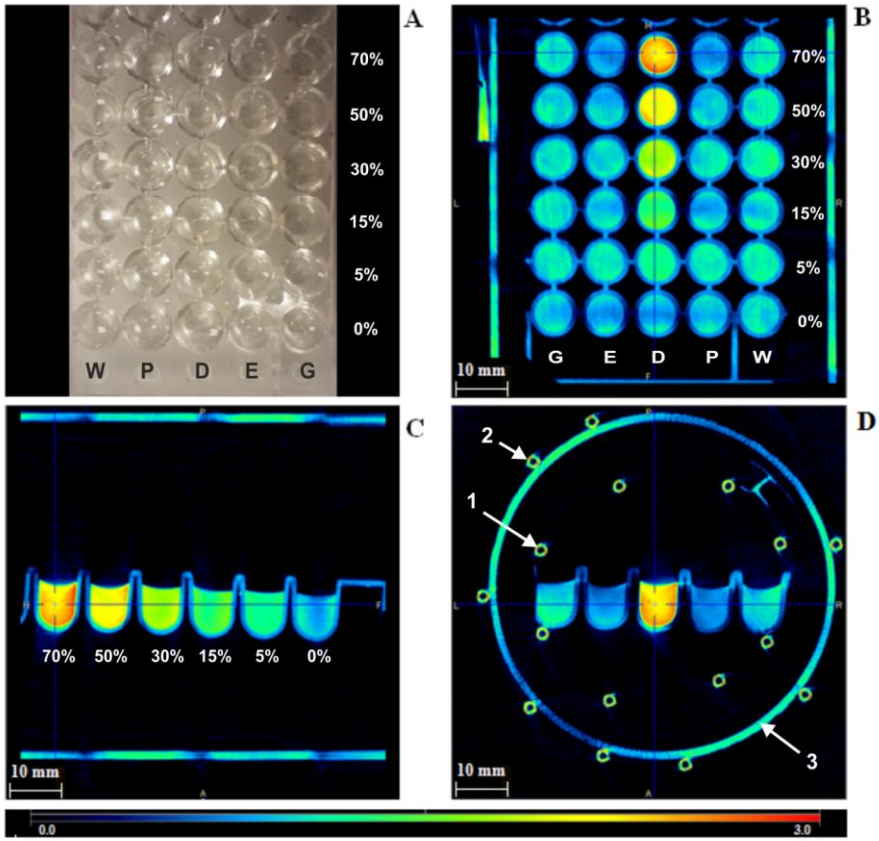

Figure 5.1. CT image of the three orthogonal views of different CPAs in several concentrations in a 9x5-well microplate, at 20 °C. The CT image uses the cold scale and a spatial resolution is 200 µm. The solutions correspond to water (W), 1,2-propanediol (P), dimethyl sulfoxide (D), ethylene glycol (E) and glycerol (G)

Fig.5.2 shows the relation between the concentration and the X-ray attenuation (HU), for water and for each CPA (1,2-propanediol, dimethyl sulfoxide, ethylene glycol and glycerol). The attenuation values are obtained from the CT image of Fig.5.1. The graph shows that the CT signal (HU) increases with the concentration only in the case of Me_2SO. The HU goes from a value of -170 ± 80 HU for 0%v/v, to 1260 ± 90 HU for 70% v/v in PBS, showing a linear dependency on the concentration and the HU. Taking into account that the errors are much smaller than the signals, this graph shows the capability of this method to measure the concentration of Me_2SO

by means of the X-ray attenuation. For the rest of CPAs, attenuation is almost constant. For example in the case of glycerol, the lowest value is 3 ± 60 HU for 70% v/v in PBS, the highest value is 90 ± 60 HU for a 5% v/v in PBS, and it has an average value of 51 ± 16 HU. Error bars are one standard deviation of the distribution of the attenuation within a 1 mm radius sphere in which the attenuation was measured in the image of Fig.5.1.

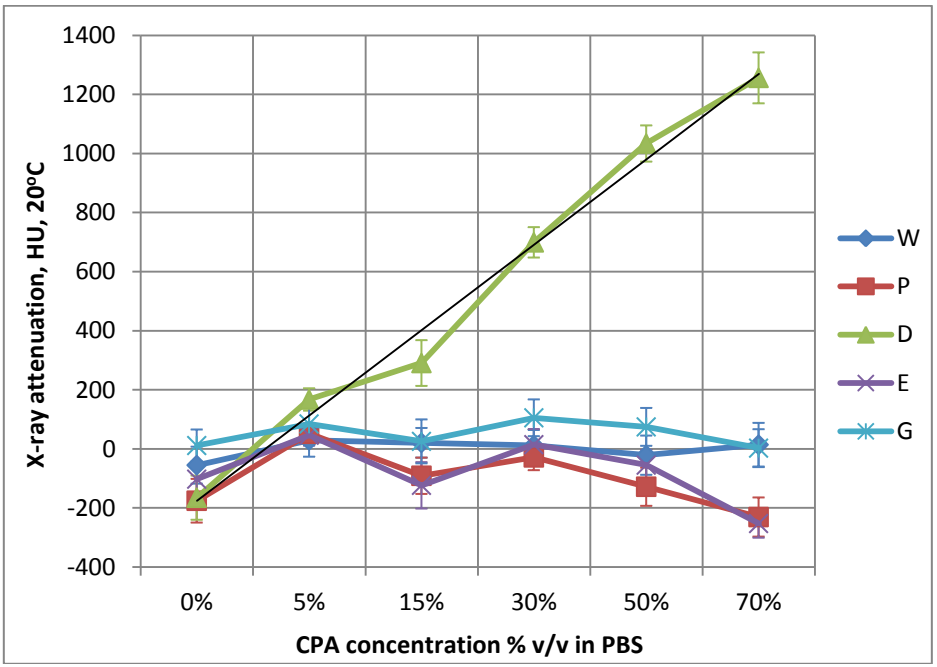

Figure 5.2. X-ray attenuation (HU) of water (W), 1,2-propanediol (P), dimethyl sulfoxide (D), ethylene glycol (E)and glycerol (G), for concentrations from 0% v/v to 70% v/v in PBS, at 20 ^{o}C

In Fig.5.3, the images show the same sample of CPAs than in Fig.5.1. but at -140 ^{o}C, visualized with the same color scale. The differences in concentrations are again only measurable in the case of Me_2SO, with similar intensity in colors. Fig.5.3.A shows a picture of the microplate with the samples. It can be observed that the first column and two first rows are frozen, which correspond to water (W) and the lowest CPA concentration (0% v/v and 5% v/v). Fig.5.3.B Bottom view of the microplate. All the CPAs are showed, from left to right: glycerol (G), ethylene glycol (E), dimethyl sulfoxide (D), 1,2-propanediol (P), and water (W), in concentrations, from

top to bottom: 70% v/v, 50% v/v, 30% v/v, 15% v/v, 5% v/v and 0% v/v (PBS), except for water, which has water in all samples. The image shows how the concentration is detectable only in the case of Me_2SO (column D), showing a different color for each concentration. In the rest of the CPAs, the color, or attenuation, remains constant for all the concentration and similar to water's. In Fig.5.3.C the column of different concentrations of Me_2SO is selected, from left to right: 70% v/v, 50% v/v, 30% v/v, 15% v/v, 5% v/v and 0% v/v (PBS). The image shows the degradation in colors, from an intense red to a dark blue, corresponding to the highest attenuation for the highest concentration. Fig.5.3.D is a selection of the top row in Fig.5.3.B, the highest concentrations of every CPA. The most favorable case to see any possible effect on different CPAs is showed. From left to right: 70% v/v glycerol, 70% v/v ethylene glycol, 70% v/v dimethyl sulfoxide, 70% v/v 1,2-propanediol, in PBS, and water. The image shows a red intense (high attenuation), only in the case of dimethyl sulfoxide. The colors are similar to the image of Fig.5.1, at 20 ^{o}C. (1) marks one of the N_2 gas input tubes, inside the insulating container, which is made of material transparent to X-rays. (2) marks one of the tubes used to prevent the formation of frost around the CT bed (3). N_2 gas, at room temperature, is sent through those tubes around the CT bed (3) to create a dry atmosphere, avoiding the condensation of water and the formation of frost. The voltage is 75 kV, the exposition time is 1500 ms and the spatial resolution is 200 μm. Color scale as in Fig.5.1. Notice that in 0% and 5% CPA concentration appear cracks due to the ice breaking.

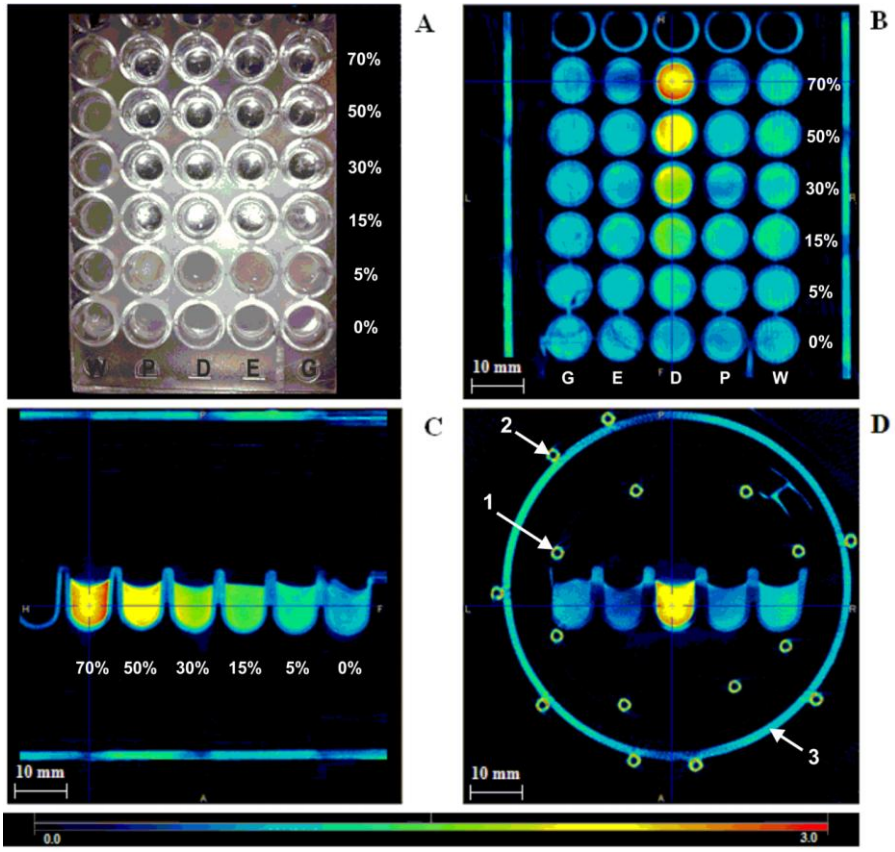

Figure 5.3. CT image of the 3 orthogonal views of different CPAs different concentrations in a 9x5-well microplate, at -140 °C. The CT image uses the cold scale and a spatial resolution is 200 µm. The solutions correspond to water (W), 1,2-propanediol (P), dimethyl sulfoxide (D), ethylene glycol (E) and glycerol (G)

In Fig.5.4, the graph shows the X-ray attenuation (HU) of each concentration for each CPA and water at -140 °C. In the graph it can be observed more detailed how HU increases only in the case of Me_2SO, in the same way that at 20 °C (Fig.5.2), although the attenuation values obtained at low temperature are slightly greater. In the curve of Me_2SO, HU values go from -90 ± 50 HU for 0% v/v, to 1450 ± 90 HU for 70% v/v in PBS. The X-ray attenuation for the rest of CPAs keeps almost constant for all the concentrations, but the averaged HU has also increased. For the case of glycerol, the lowest attenuation corresponds to 0% v/v (70 ± 90 HU), the

highest to 50 % v/v (220 ± 70 HU) and the average is 146 ± 19 HU. Error bars are one standard deviation of the distribution of the attenuation within a 1 mm radius sphere in which the attenuation was measured in the image of Fig.5.3.

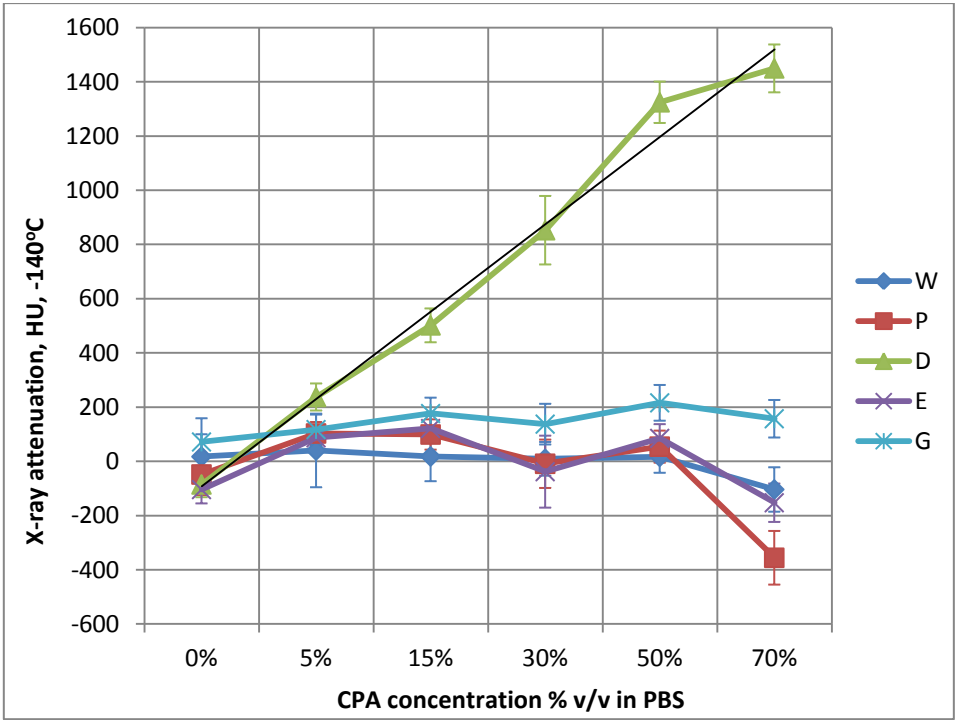

Figure 5.4. X-ray attenuation (HU) of water (W), 1,2-propanediol (P), dimethyl sulfoxide (D), ethylene glycol (E) and glycerol (G), for concentrations from 0% v/v to 70% v/v in PBS, at -140 °C

The comparison of the curve of Me_2SO at 20 °C and -140 °C is showed in Fig.5.5. There is a linear relation between X-ray attenuation (HU) and the CPA concentration for both measured temperatures; that is, in both cases it can be represented as:

$HU = a * C_{CPA} + b$

Table 1 shows the values of *a*, *b* and the regression coefficient (*r*). For 20°C and for -140 °C, the slopes of both linear regressions are similar, with a value of 19 ± 2 at 20°C and 22 ± 3 at -140 °C. However it is observed that HU in the solutions at -140 °C are in average 170 HU greater than the solutions at 20 °C.

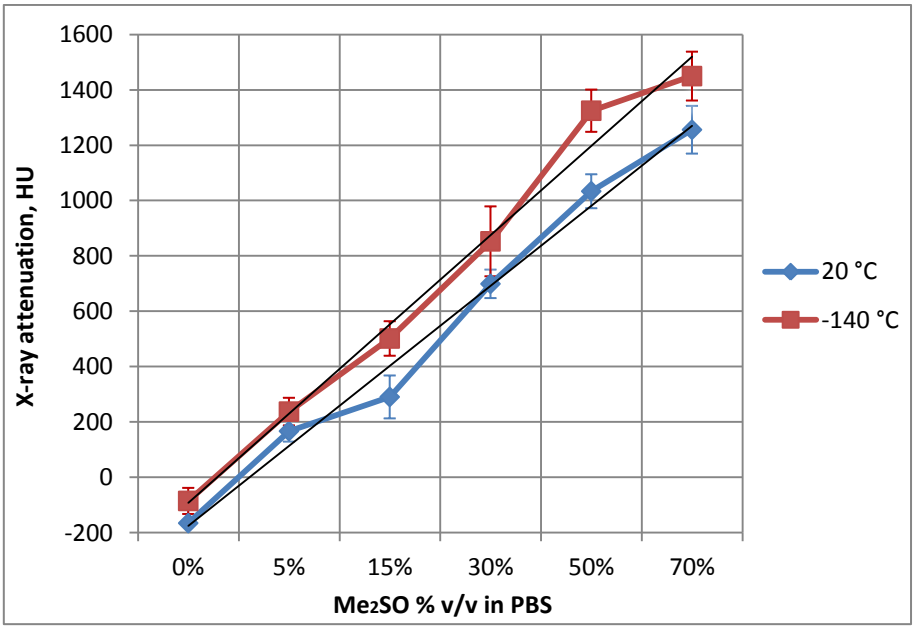

Figure 5.5. Comparison of X-ray attenuation (HU) of dimethyl sulfoxide, at 20°C and -140 °C , for concentrations from 0% v/v to 70% v/v in PBS

Linear regression coefficients	*20 °C*	*-140 °C*
a	19 ± 2	22 ± 3
b	0 ± 80	100 ± 100
r	0.97	0.97

Table 5.1. Coefficients of the linear regressions of HU versus Me_2SO concentration at 20 °Cand -140 °C, represented in Fig.5.5

5.1.2. Group 2: comparison of different Me_2SO solutions in different volumes.

After proving that Me_2SO solutions are measurable by CT method, we imaged samples of higher volumes to evaluate the influence of the volume and container into the attenuation of the samples. The results are presented below.

The image of the Eppendorf tubes is shown in Fig.5.6. The figure shows ten Eppendorf tubes, of 1.5 ml, filled with water, and solutions of Me_2SO in PBS, from 0M to 8M, at 20 ^{o}C.

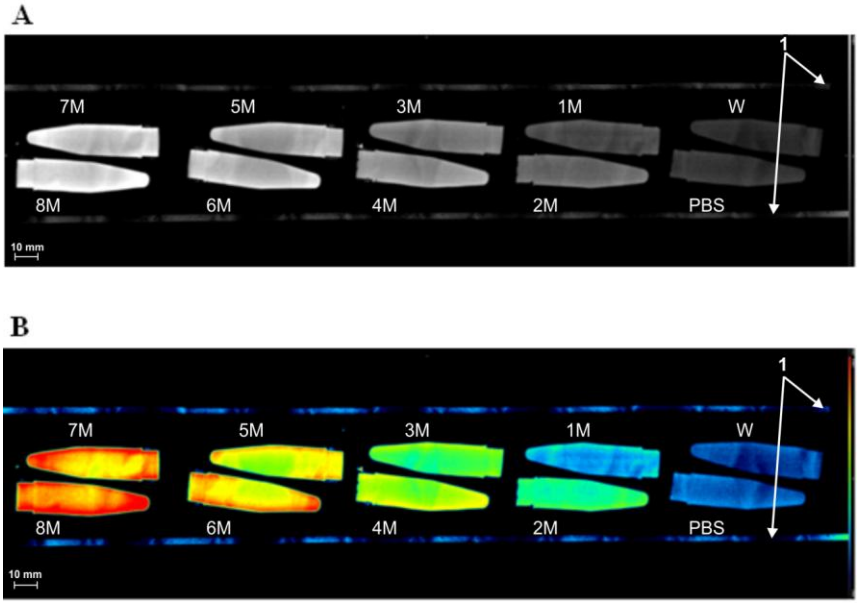

Figure 5.6. CT image of 10 Eppendorf tubes with different solutions of Me_2SO in PBS, at 20 ^{o}C. Top image (A) uses the gray scale and bottom image (B) the cold scale. In both scales, bottom row, from right to left, correspond to: 0M (PBS), 2M, 4M, 6M and 8M Me_2SO, and top row, from right to left: water, 1M, 3M, 5M and 7M Me_2SO

Images are shown in the gray scale (Fig.5.6.A), and the cold scale (Fig.5.6.B). The solutions correspond to, first row right to left: 0M (PBS), 2M, 4M, 6M and 8M of Me_2SO, and second row, from right to left: water, 1M, 3M, 5M and 7M of Me_2SO, for both images. In Fig.5.6.A, the most intense white

color corresponds to the highest concentration, being the color of water or PBS dark gray. In Fig.5.6.B, the 8M concentration has an intense red color, while water and PBS has a dark blue color. (1) marks the carbon fiber bed of the CT device. The voltage is 75 kV, the time of exposition is 1500 ms and the spatial resolution is 200 µm in both images.

The graph of Fig.5.7 shows the average X-ray attenuation (HU) for each molar concentration of Me_2SO in PBS, at 20 ^{o}C, in the Eppendorf tubes. The average attenuation values have been obtained from the CT image of Fig.5.6. Again, it can be observed that the attenuation increases with the concentration, where values go from 80 ± 40 HU for 0M (PBS) to 960 ± 60 HU for 8M Me_2SO in PBS. Error bars are one standard deviation of the distribution of the attenuation within a 1 mm radius sphere in which the attenuation was measured in the image of Fig.5.6.
H_2O Me_2SO

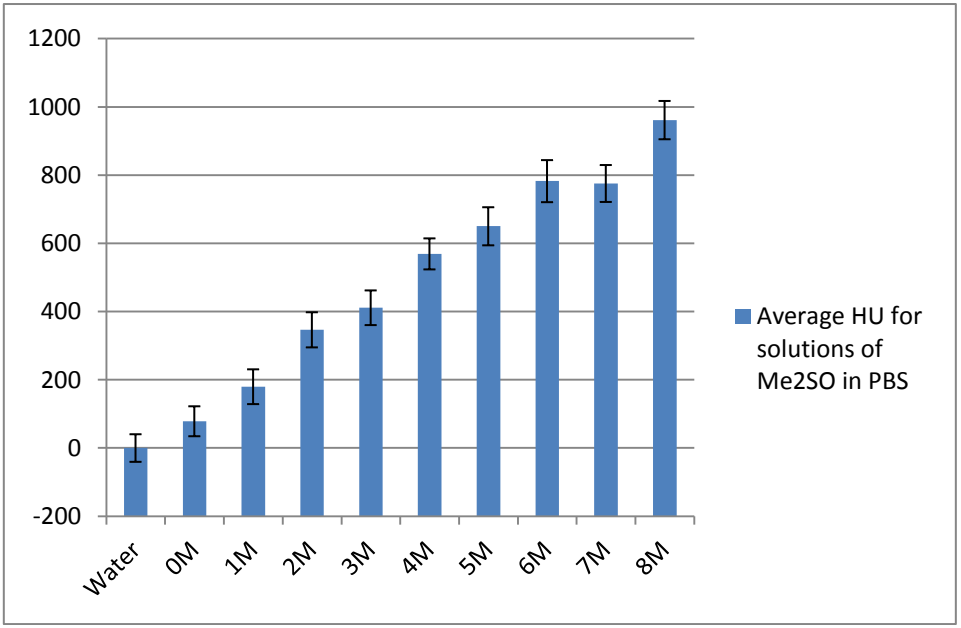

Figure 5.7. Average X-ray attenuation (HU) of water and Me_2SO solutions in PBS from 0M (PBS) to 8M, at 20 ^{o}C, in the case of the Eppendorf tubes as containers

This relation is also proved in Fig.5.8, where the image shows different containers, Falcon tubes of 20 ml, filled with different concentrations of Me_2SO in PBS. The cold scale was used for its visualization, where the colors scale go from dark blue for low attenuation to intense red for higher attenuations.

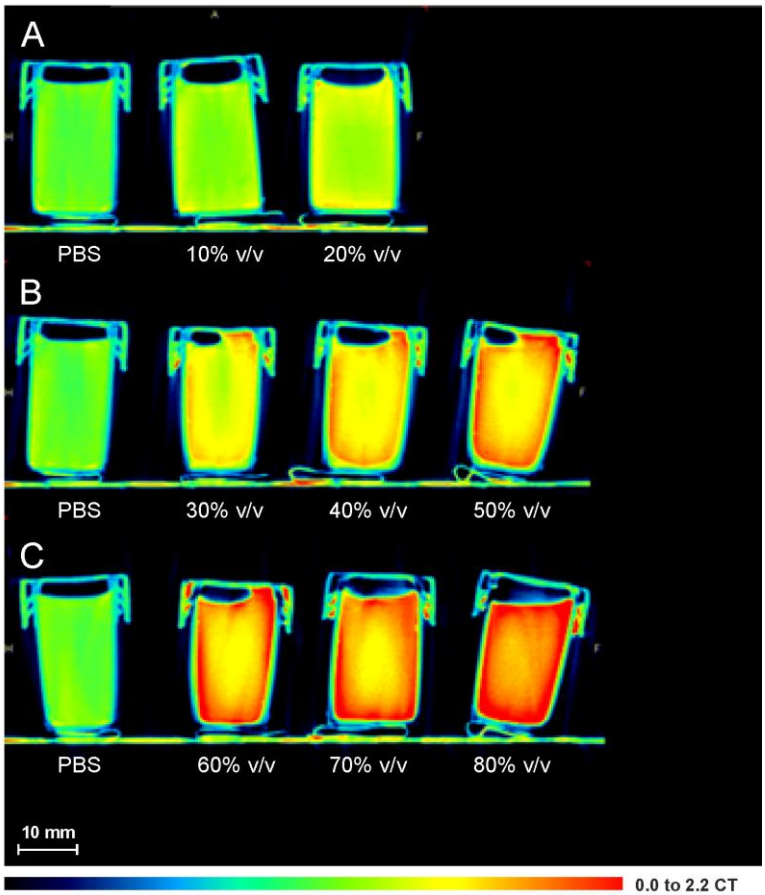

Figure 5.8. CT image of different Me_2SO solutions in PBS in 20 ml PP Falcon tubes, at 20 °C. The different solutions are, from left to right: (A) 0M (PBS), 10% v/v and 20% v/v Me_2SO, (B) 0M (PBS), 30% v/v, 40% v/v and 50% v/v Me_2SO and (C) 0M (PBS), 60% v/v, 70% v/v and 80% v/v Me_2SO. The CT image uses the cold scale and the spatial resolution is 200 µm

The containers from left to right, correspond to: in Fig.5.8.A, 0% v/v (PBS), 10% v/v and 20% v/v of Me_2SO, whose colors go from green to yellow, low attenuation in this scale; in Fig.5.8.B, 0% v/v (PBS), 30% v/v and 40% v/v of Me_2SO, with colors from yellow-orange to red, which means an increase of the attenuation; and in Fig.5.8.C, 0% v/v (PBS), 60% v/v, 70% v/v and 80% v/v of Me_2SO, from red to intense red for the highest concentration. In this image it is observed how the color is not homogeneous for the same concentration. This fact is due in part to artifacts during the reconstruction of the images because of the beam hardening effect. The effect happens when X-rays pass through matter, the low energy photons are preferably absorbed. As consequence, the beam which traverses the medium has higher energy photons and therefore is more penetrated. Hence, the attenuation produced by a given material is not strictly proportional to its thickness (ec. [1]) and it leads to artifacts in reconstruction tomography. These artifacts are minimized by the application of filters of the beam and linearization corrections to the detector outputs (18).The voltage is 65 kV, the time of exposition is 1500 ms and the spatial resolution is 200 µm.

Fig.5.9 shows the number of pixels with the same attenuation value (CT values) in a sphere of 20 mm diameter for each solution of image from Fig.5.8: PBS (from Fig.5.8.A) and Me_2SO solutions from 10% v/v to 80% v/v. This graph shows again that there is a direct relation between the Me_2SO concentration and the CT signal (X-ray attenuation). Moreover it gives information about the dispersions errors of the measurements, showing Gaussian curves where most pixels have the same CT value for each concentration. The maximum CT value for each curve is increasing with the concentration, as expected.

In Fig.5.10 we study the reproducibility of the CT measurements. The curves show the CT values (CT) of the three different measurements of PBS versus the number of pixels in a 20 mm diameter sphere with the same CT value. The attenuation values are taken from the average attenuation values of the three different measurement of the PBS solution from Fig.5.8.A, Fig.5.8.B and Fig.5.8.C. The three curves present the same shape with an average CT value of 1.05, corresponding to the maximum of the curve.

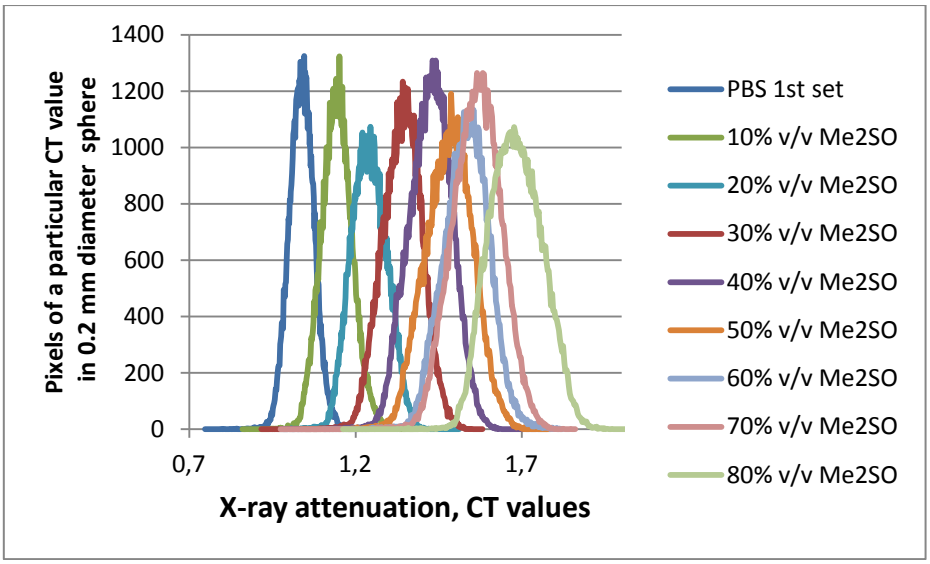

Figure 5.9. Number of pixels in a 20 mm diameter sphere with the same X-ray attenuation (CT values), for the different Me_2SO concentrations of Fig.5.8

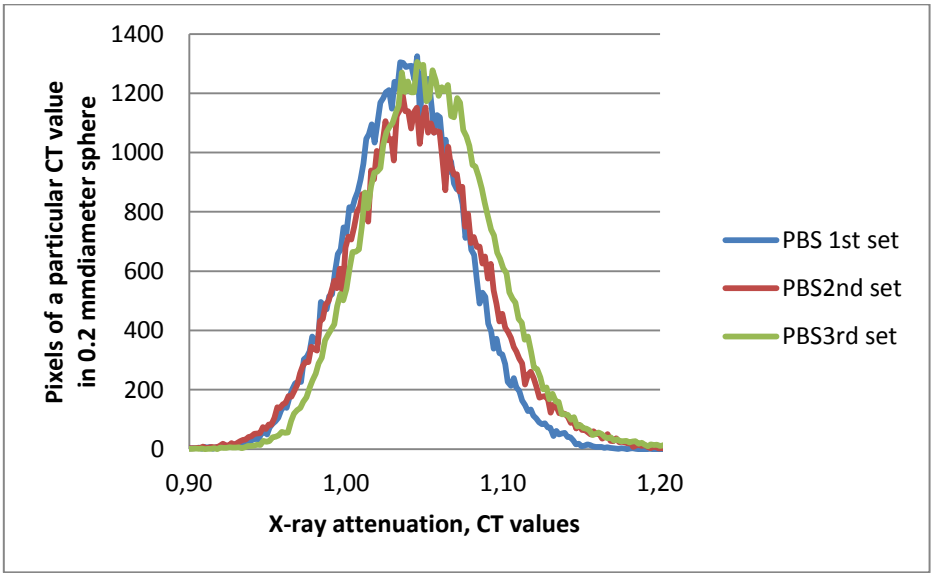

Figure 5.10. Number of pixels in a 20 mm diameter sphere with the same X-ray attenuation (CT values), for the three different measurements of PBS of Fig.5.8

5.1.3. Group 3: rabbit kidneys immersed in different Me_2SO solutions.

The main objective of these experiments was to prove the behavior of tissues under the X-rays treatment. This CT technology was demonstrated to be adequate to measure CPA concentrations inside kidney tissues.

Fig.5.11 and 5.12 show the attenuation for tissues in different solutions. A rabbit kidney is immersed in different solutions of Me_2SO in PBS. In both figures, from top to bottom: (A) 0% v/v (PBS), (B) 5% v/v, (C) 30% v/v and (D) 55% v/v of Me_2SO. An Eppendorf with water is also added into the vials. Also in both, Fig.5.11 and Fig.5.12, (a) shows the air contained at the top of the container, (b) marks the Eppendorf with water and (c) the location of the kidney. In some of the views the Eppendorf is not present because it is located in a different slice to that of the kidney.

In Fig.5.11, the images are obtained right after their immersion and for the visualization we selected the cold scale. It can be observed that the kidney (c) is not detected in PBS (Fig.5.11.A), and hardly detected in 5% v/v (Fig.5.11.B), since the composition inside and outside the kidney is similar. Moreover it behaves similar to the water in the Eppendorf (b), since the kidney composition is mainly water. For a higher concentration, 30% v/v (Fig.5.11.C) and especially 55% v/v (Fig.5.11.D), both, Eppendorf (b) and kidney (c), can be differentiated from the solution, showing a much lower X-ray attenuation than the solution. It is also observed that the kidney floats in the solution, since the density of the kidney is lower than the most concentrated Me_2SO solution. The voltage is 65 kV, the time of exposition is 1500 ms and the spatial resolution is 200 μm.

In Fig.5.12, the kidneys were left to equilibrate with the solution concentration of the vial for 9 days, and then imaged. The kidney (c) is not now detected in any of the solutions, since the kidneys have the same concentration as the solutions outside. However, the Eppendorf (b) can be distinguished in the highest concentrations, 30% v/v (Fig.5.12.C) and 55% v/v (Fig.5.12.D).

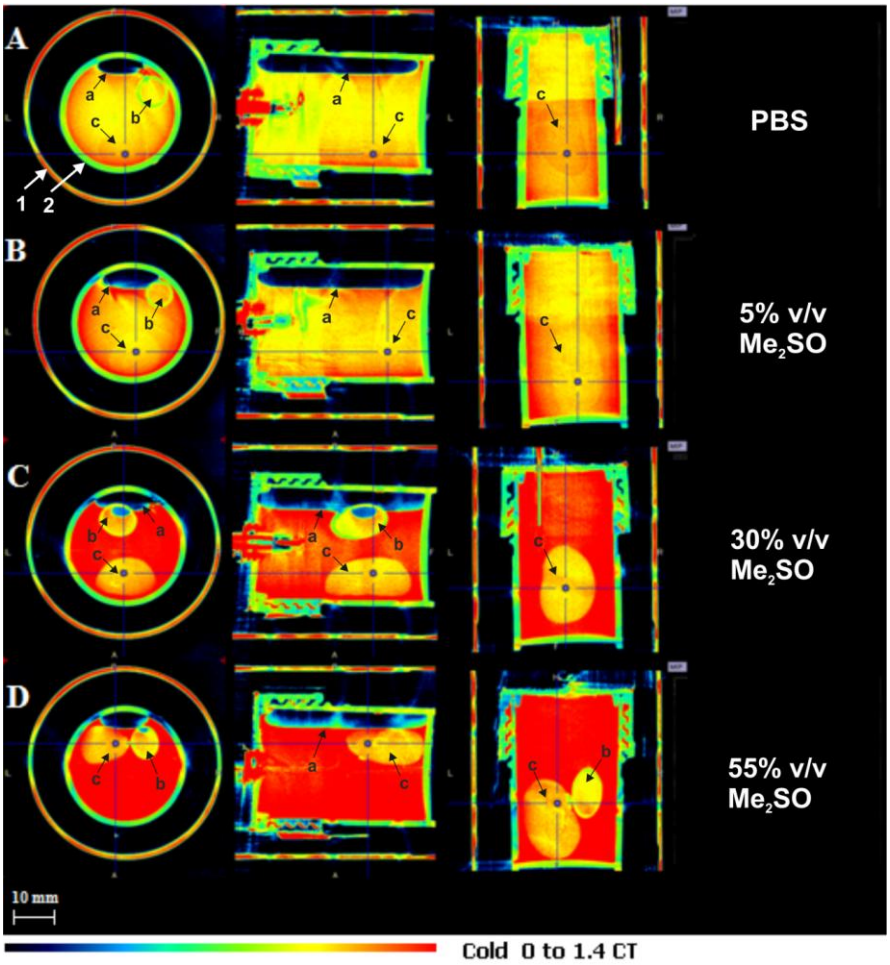

Figure 5.11. CT image of the 3 orthogonal views of kidney and Eppendorf with water immersed in different Me_2SO solutions in PBS, in a 30 ml PP vial at 20 °C. The kidneys were not equilibrated with the concentrations of the solutions. The solutions correspond to: (A) 0% v/v (PBS), (B) 5% v/v, (C), 30% v/v and (D) and 55% v/v of Me_2SO in PBS. The CT image is uses the cold scale and the spatial resolution is 200 µm

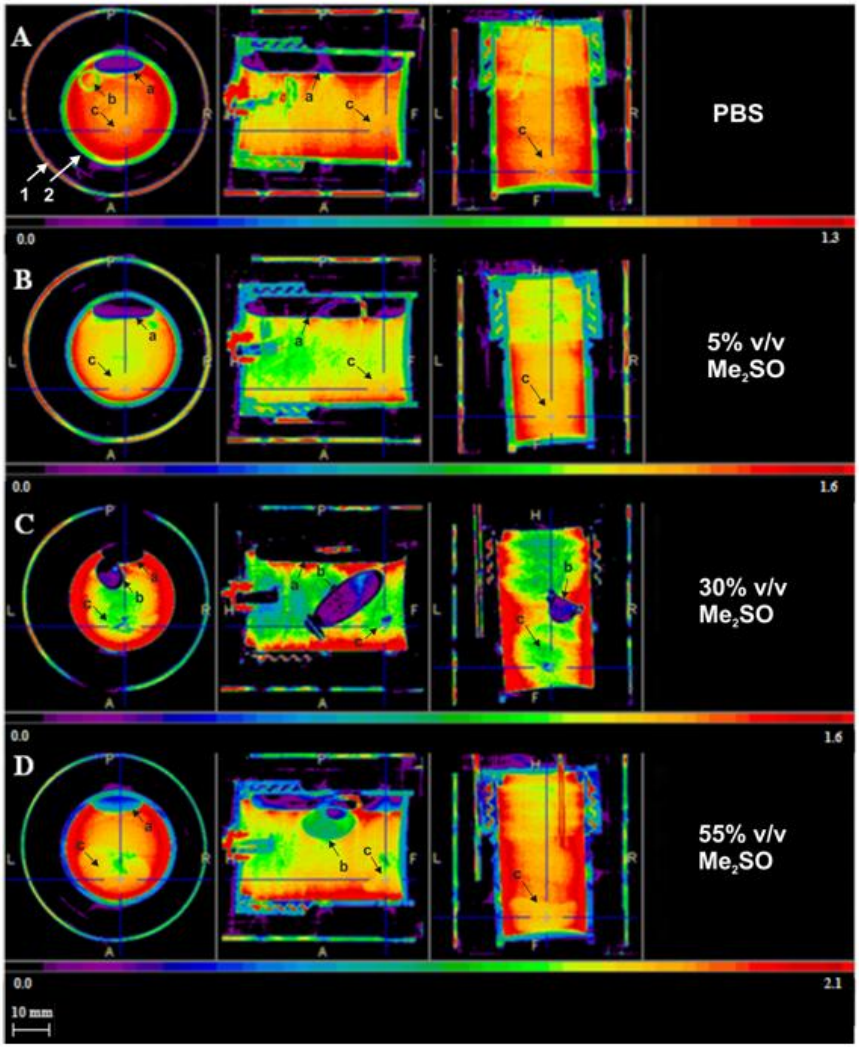

Figure 5.12. CT image of the 3 orthogonal views of kidney and Eppendorf with water immersed in different Me_2SO solutions in PBS, in a 30 ml PP vial at 20 ^{o}C. The kidneys were equilibrated with the concentration of the solutions for 9 days. The solutions correspond to: (A) 0% v/v (PBS), (B) 5% v/v, (C), 30% v/v and (D) and 55% v/v of Me_2SO in PBS. The CT image uses the cold scale and the spatial resolution is 200 µm

5.2. Ice detection measurements.

In this section we will present and discuss the results obtained from the experiments performed with the aim of detecting ice formation in samples or solutions. In the previous section we have proved that Me_2SO solutions can be differentiated from water, and therefore ice could be also differentiated from tissues equilibrated with Me_2SO solutions. The results are presented in the same order as the different groups of experiments were described in Chapter 4.6.

5.2.1. Group 1: piece of ice immersed in a 50% v/v Me_2SO solution, at -20 ^{o}C.

This is a preliminary experiment to very simply to determine whether a piece of ice immersed in a Me_2SO solution (50% v/v) could be detected by means of the CT device. Fig.5.13 shows the CT image of the three orthogonal views of a piece of ice of 1x1.5x1.5 cm^3 immersed in a 50% v/v Me_2SO solution, at -20 ^{o}C, in a 20 ml vial. For the visualization of the image we selected the cold scale, which corresponds to dark blue color for low attenuation and intense red color for high attenuation. Fig.5.13.A shows the main view of the vial, where the profile of the CT bed is also seen. The ice is perfectly differentitated from the Me_2SO solution, which appears in a green color versus the red color of the solution. Fig.5.13.B and Fig.5.13.C are the side and top view of the vial with the ice block, showing the same color for ice. The voltage is 65 kV, the time of exposition is 1500 ms and the spatial resolution is 200 μm.

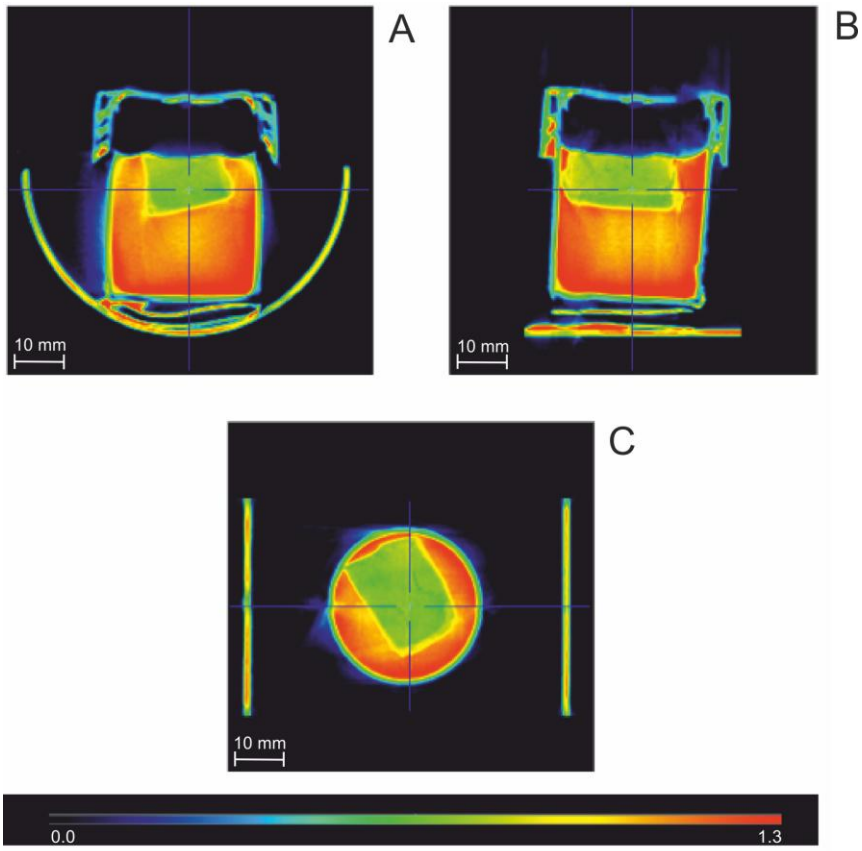

Figure 5.13. CT image of the 3 orthogonal views of an ice block in a solution of 50% v/v Me_2SO in PBS. A piece of ice of 1x1.5x1.5 cm^3 was immersed in a solution of 50% v/v Me_2SO in a 20 ml vial, at -20 ^oC. The image uses the cold scale and the spatial resolution is 200 µm

5.2.2. Group 2: 200 µm diameter capillary filled with water immersed in a 55% v/v Me_2SO solution, at 20 ^oC.

The aim of this group of experiments was to detect small volumes of water, at room temperature, in order to determine the minimum size of ice to be able to detect. The volume of water introduced is about 3 x 10^{-4} cm^3, five orders of magnitude less than the experiment of the previous group (around 2 cm^3). Although several experiments were performed we present

here the most representative result. Since this section show qualitative result of ice detection, other images were not relevant for the presented result.

Fig.5.14 showed the capability to detect small volumes of water, around 0.3 mm^3, inside a concentrated Me_2SO solution, at 20 ^oC. The CT image shows the three orthogonal views of a 40 mm length of a polycarbonate capillary of 200 μm diameter filled with water immersed in a 55% v/v Me_2SO solution of in PBS. The image uses the cold scale, and the capillary can be detected with a green-yellow color, showing low attenuation, very different from the red color of the solution, of high attenuation. Fig.5.14.A shows the main view of the Cryovial, where the solution appears in an intense red (high attenuation). The capillary with water is differenciated in a green-yellow color. The image proves that small volumes of water can be distinguised in a concentration solution of Me_2SO. Fig.5.14.B shows the top view, with a magnification of 5 times. A slice of the capillary can be observed at the top of the image, at the center of the two blue axis, in a yellow color. The image presents too much noise, due in part to the high resolution. Moreover, the capillary shows a color , and therefore attenuation, higher than the one corresponding to water. This is due to the envorimental density artifacts, which consist of a small change in the CT value of a central region when it is sourrounded by a larger area with different attenuation coefficents (102). In this case, since the attenuation of the volume around is greater than the capillary's one, the CT values corresponding to the capillary have been slighty increased. Fig.5.14.C shows the side view, with the same magnification as Fig.5.14.B. The capillary is detected at the top, in green-yellow color. The same noise as in Fig.5.14.B. is observed. The voltage is 65 kV, the time of exposition is 1500 ms and the spatial resolution is 100 μm.

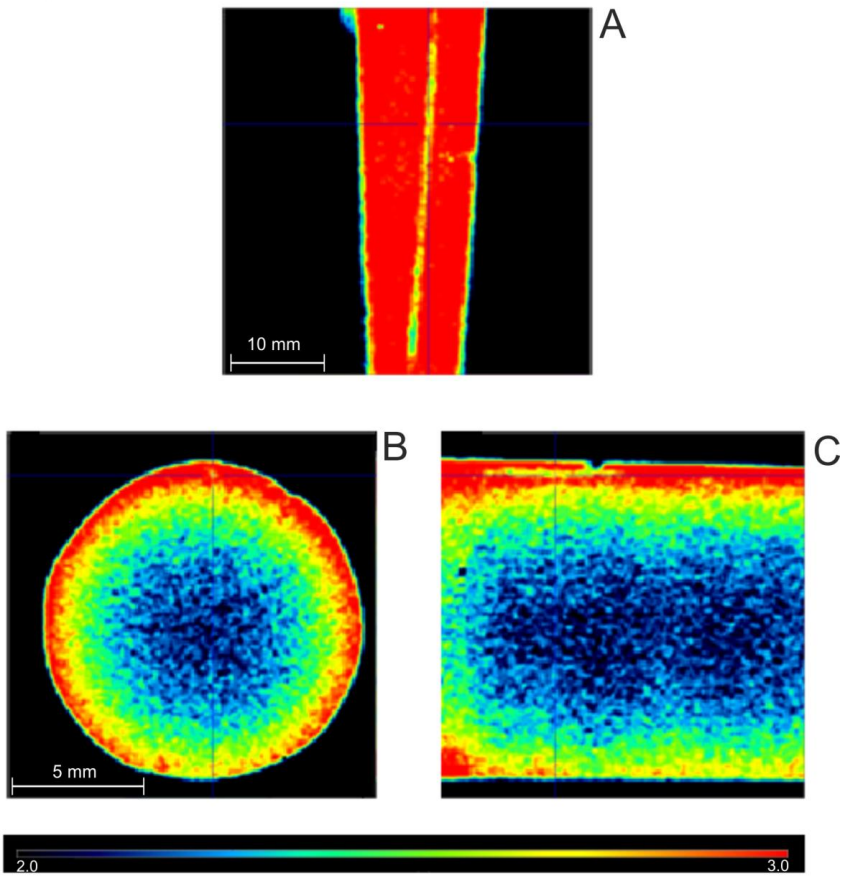

Figure 5.14. CT image of the 3 orthogonal view of 40 mm of 200 µm diameter capillary filled with water and heat-sealed in a solution of 55% v/v Me_2SO in PBS, in a Cryovial, at 20 ^{o}C. The image uses the cold scale and the spatial resolution is 100 µm

5.2.3. Group 3: 200 µm diameter capillary filled with water inserted into a kidney loaded with a 55% v/v Me_2SO solution, at 20 ^{o}C.

The next step for our final aim was to study wether those small volumes of samples of water could be detected in tissues equilibrated with Me_2SO solutions. Also we only show the most representive image.

30 mm length of capillary of 200 diameter filled with water is inserted in a kidney equilibrated with 55% v/v Me_2SO, at 20 ^{o}C. Fig.5.15 shows the 3

orthogonal views. The image uses the cold scale and a spatial resolution of 50 µm. Fig.15.5.A shows a picture of the position of the capillary inside the kidney, which has been previously loaded with a 20% v/v Me_2SO solution in PBS. Fig.5.15.B shows the main view of the image, where the capillary appears in green-yellow color, which means lower attenuation than the tissue, in red. In this approach we are able to distinguish small volumes of water inside tissues loaded with Me_2SO. In the image some noise is observed (yellow points), due especially to the high resolution used in the reconstruction of the image. Fig.5.15.C is the top view, where a slice of the capillary is showed at the center of the two blue axis, in a green-yellow color. Fig.5.15.C shows the side view: the capillary in green-yellow color is again differenciated from the solution, in red color. The voltage is 65 kV, the exposition time is 1500 ms and the spatial resolution 50 µm.

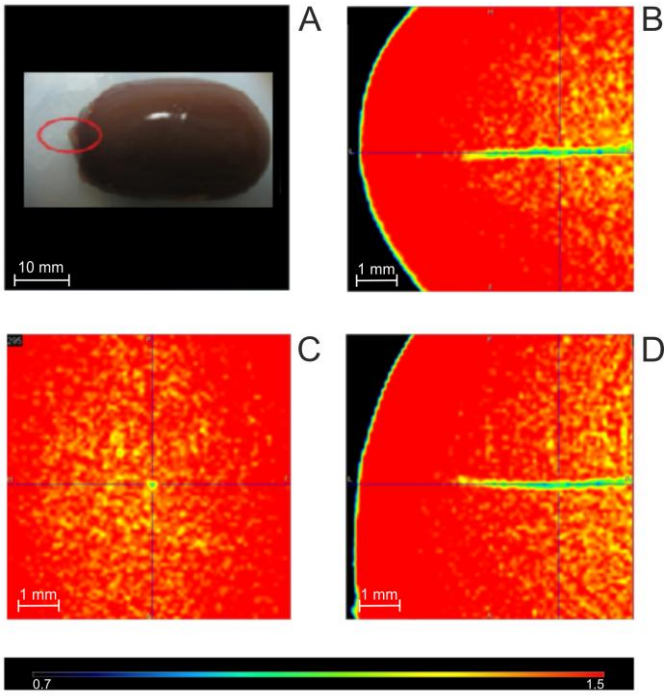

Figure 5.15. CT image of the three orthogonal views of 30 mm of 200 µm diameter capillary filled with water and heat-sealed inserted inside a kidney loaded to 20% v/v of Me_2SO in PBS, at 20 ^{o}C. The image uses the cold scale and the spatial resolution is 50 µm

5.2.4. Group 4: drops of water injected into a kidney loaded with a 55% v/v Me_2SO solution at -20 ^{o}C, and then cooled to -196 ^{o}C.

With this group of experiments we have proved the capability of this approach to detect ice crystals of volumes up to 2 µL inside a vitrified kidney. In the following we show the results obtained for experiments with kidney A, kidney B and kidney C.

Kidney A:

Fig.5.16 shows a section of the kidney A, loaded with 55% v/v Me_2SO, with 8 drops of water inserted and then cooled to -196 ^{o}C and placed inside the equipment previously cooled at -140 ^{o}C (see Chapter 4, section 4.6, group 4). In the image we can observe three of the eight drops of water, which are ice crystals. The drops are surrounded by colored lines, blue, pink and red, which are VOIs (volume of interest). VOIs are a tool of the image analysis software (PMOD) which allow us to calculate the CT attenuation of the vowels inside them. We calculate the volume of the drop as the volume inside the VOI with a value of attenuation equal to water's value. The image uses the cold scale, where blue means a low attenuation. The kidney is not differentiated since the solution outside it is the same concentration than inside it. All the VOIs are showed in Fig.5.17. There is also some big blue area around the VOIs. That can not be ice because of its shape and big area. It corresponds to the fat of the kidney, which also has low attenuation, as we have seen in other experiments. The voltage is 75 kV, the time of exposition is 1500 ms and the spatial resolution is 50 µm.

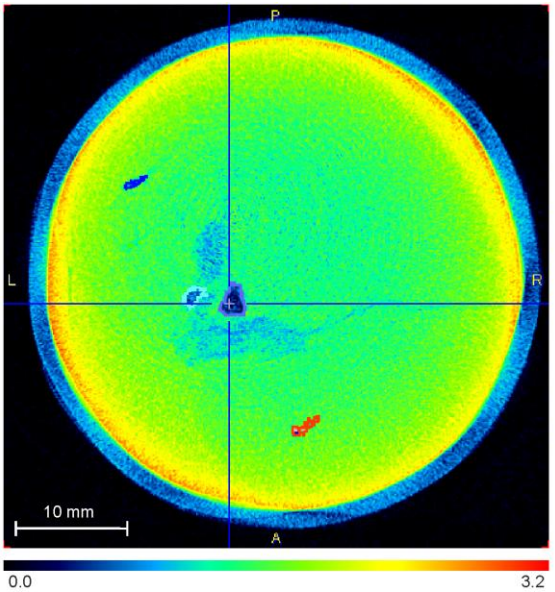

Figure 5.16. CT image of a slice of the kidney A, loaded to 55% v/v Me_2SO, in which has been inserted eight drops of water and then cooled to -196 ^{o}C. The image was taken at -140 ^{o}C. The image uses the cold scale and the spatial resolution is 50 µm.

Fig.5.17 shows the 3 orthogonal views of the same kidney. The image uses the grey scale, where white corresponds to the lowest attenuation and black to the highest one. Fig.5 .17.A shows the top view of the kidney with the VOIs surrounded by six of the ice crystals in different colors: blue, green, light blue, purple, red and pink. In the center of the kidney a region with grey color is observed, which corresponds to the fat of the kidney, with a low attenuation. Fig.5.17.B is the side view where the light blue VOI is showed. Fig.5.17.C corresponds to the front view where light blue and blue VOIs are observed. In Fig.5.17.D the kidney is observed with the eight VOIs in different colors, which correspond to each of the drops. Most of the VOIs are in line, as drops were inserted. However, there is a red VOI which is away from that line. That could be due to a diffusion of the water inside the canal that the needle made.

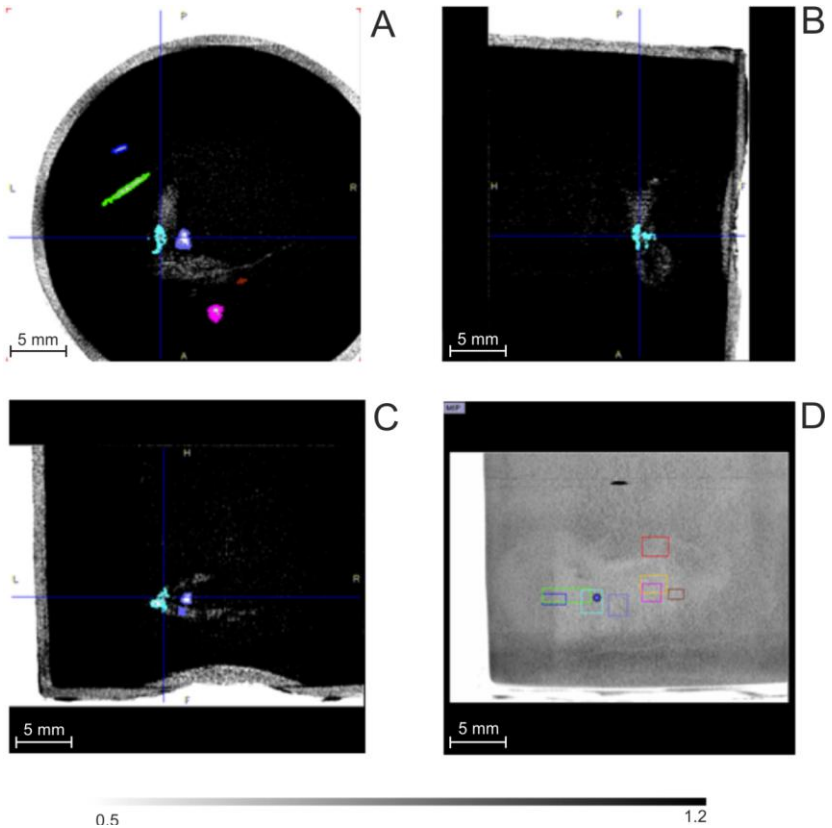

Figure 5.17. CT image of the three orthogonal views of the kidney A, loaded to 55% v/v Me_2SO, in which has been inserted eight drops of water and then cooled to -196 ^{o}C. The image was taken at -140 ^{o}C and it uses the gray scale

Fig.5.18 shows the X-ray attenuation for each drop of water, in CT values, for kidney A. The values go from 0.65 to 0.90 CT values. These values are in the range of water attenuation, which is around 0.8 CT values, calculated from our experiments. This proves that the volumes correspond to water and therefore to ice, since the temperature is -140 ^{o}C. So this technique is able to detect small volumes of ice crystals, which is the objective of this group of experiments. However, most drops of water diffused before became frozen.

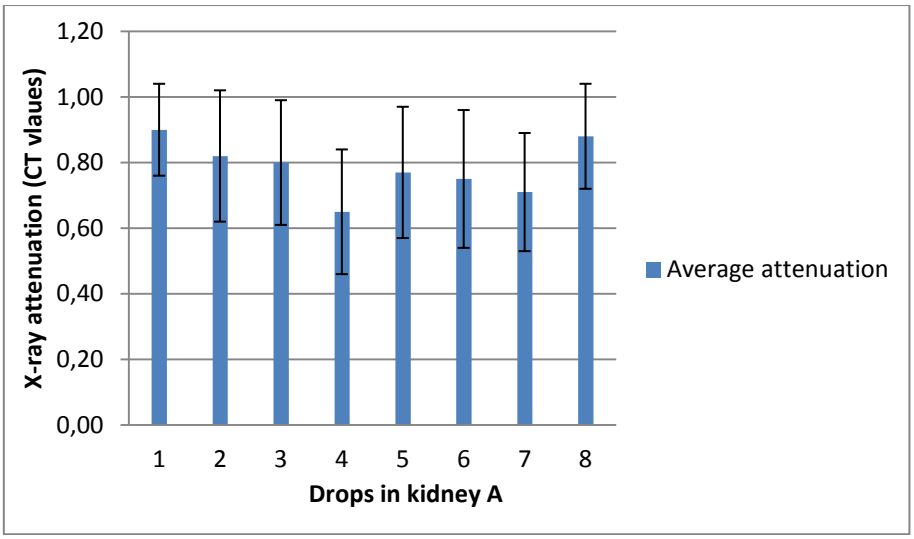

Figure 5.18. The graph shows the average attenuation for each drop in kidney A, in CT values

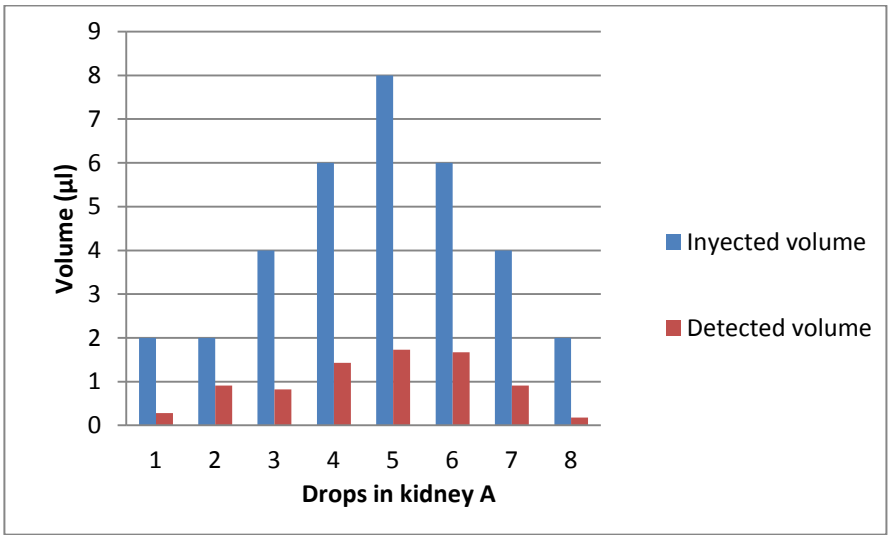

Figure 5.19. The graph compares the volume (µL) of the drops of water inserted (blue columns) versus the volume of ice detected (red columns) in kidney A. The values of the volumes are also showed in table 5.2

That can be seen in Fig.5.19, where there is a comparison of the inserted drops volumes and the volumes calculated by the VOIs method, in kidney A. The values of those volumes are showed in table 5.2, with the highest percentage of detection, 46 %. The drops of water have been diffused during their insertion. Although the temperature of the kidney was -20 ^{o}C, not all the water freezes during their insertion and some of the volume could have warmed the tissue and diffused in it. Anyway, the results show the capability of the technique to detect ice crystals of volumes less than 1 µL in a vitrified tissue loaded with Me_2SO.

Kidney B:

Fig.5.20 shows two CT images of the three views of the kidney B. The kidney was loaded with 55% v/v Me_2SO and 4 drops were inserted in it before cooling them to -196 ^{o}C. The image was taken at -140 ^{o}C and it uses the cold scale. The border of the kidney is barely appreciable in all views in a blue color. In Fig.5.20.A three of the four drops can be observed, surrounded by colored lines, which correspond to VOIs: pink, red and blue. In Fig.5.20.B, the blue VOI appears at the top. Fig.5.20.C shows another view of the kidney, where two VOIs are observed (light blue and blue). Fig.5.20.D shows a 3D view of the container with the four VOIs in line: pink, red, blue and light blue. The voltage is 75 kV, the time of exposition is 1500 ms and the spatial resolution is 100 µm.

Kidney B is also represented in 3D in Fig.5.21. The 3D image shows kidney B with the VOIs. The image is created showing only the vowels with a high attenuation, from a certain CT value. In this way the kidney is determined, since it is loaded with a high concentration of the Me_2SO. VOIs also appear in the image in different colors, showing the location of the ice crystals.

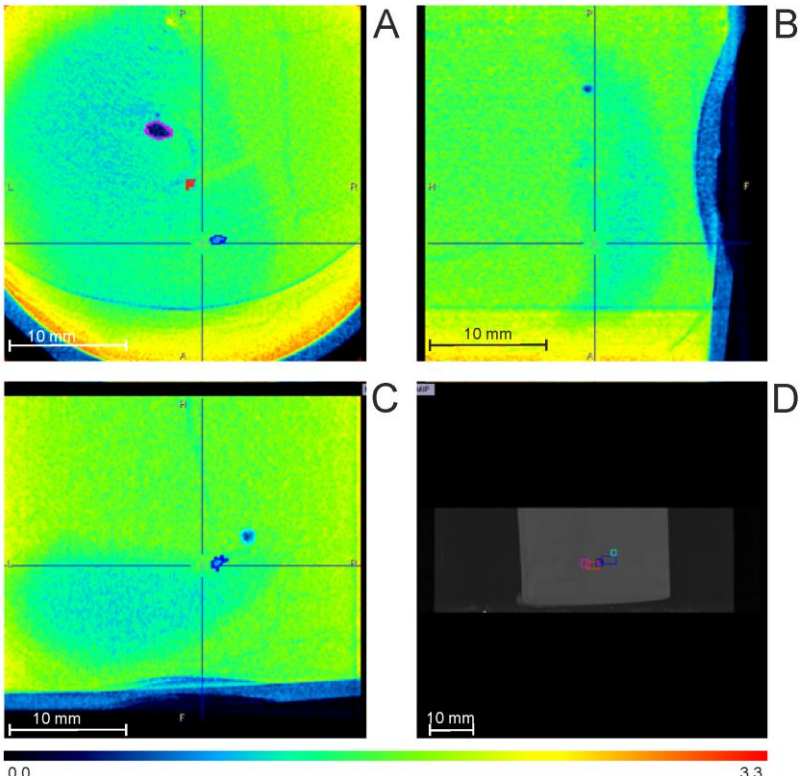

Figure 5.20. CT image of a slice of the kidney B, loaded to 55% v/v Me_2SO, in which has been inserted four drops of water and then cooled to -196 °C. The image was taken at -140 °C. The image uses the cold scale and the spatial resolution is 100 µm

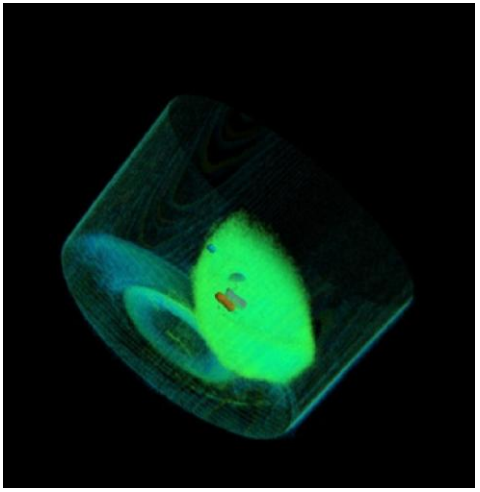

Figure 5.21. CT 3D image of kidney B with VOIs (volumes of interest). The image shows only the vowels with high attenuation from a certain value of CT

Fig.5.22 represents the average X-ray attenuation of the ice crystals in kidney B. The values go from 0.56 to 0.95 CT values, which are values similar to water's attenuation, much lower attenuation than the solution. This values prove that the volume found in the kidney correspond to ice, since water at that temperature has been solidified.

Fig.5.23 shows the comparison of the volume of drops of water injected and the volume of ice crystals detected for kidney B. Again most of the water has been diffused inside the tissue, with a maximum percentage of detection of 69 %, as can be observed in table 5.3. Part of the drops of water has been diffused during their insertion.

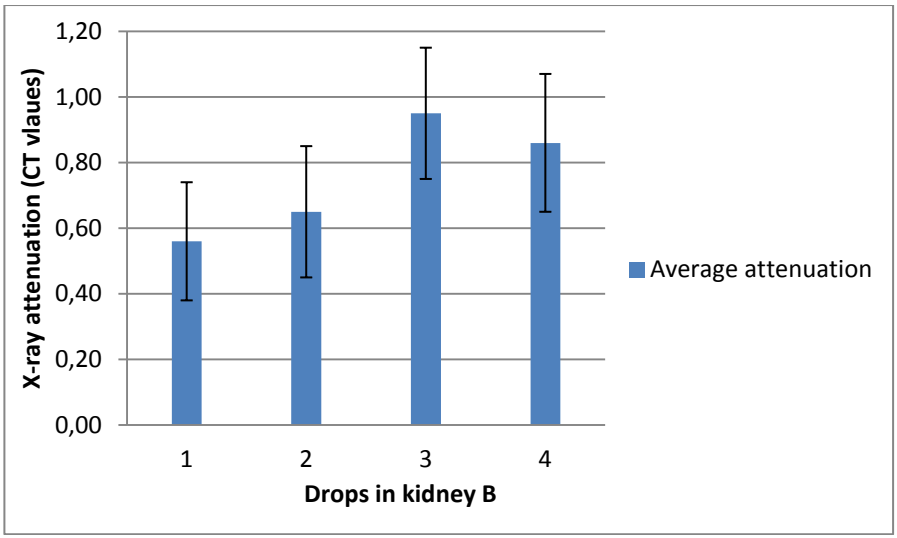

Figure 5.22. The graph shows the average attenuation for each drop in kidney B, in CT values

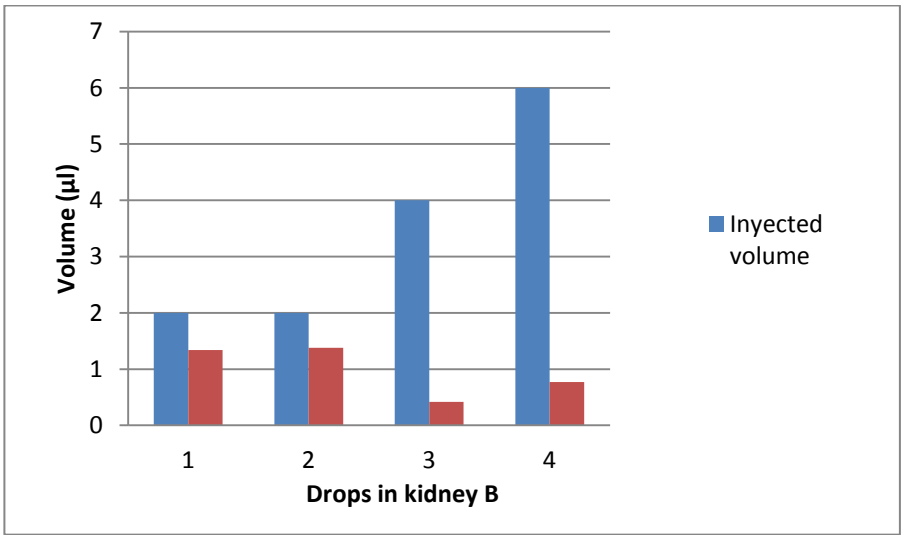

Figure 5.23. The graph compares the volume (µL) of the drops of water inserted (blue columns) versus the volume of ice detected (red columns) in kidney B. The values of the volumes are also showed in table 5.3

Kidney C:

The capability to detect ice is also proved with kidney C. Six drops of water were inserted in the kidney, loaded also with 55% v/v of Me_2SO, before cooling it to -196 ^{o}C by immersing it in liquid nitrogen. The CT image of kidney C is showed in Fig.5.24. Even though we introduced only 6 drops of water, we could detect 9 VOIs which could be drops of water, according to their CT values. The kidney is barely seen in all the view in blue. In Fig.5.24.A it can be observed 4 of the VOIs in colors, from right to left: red, purple, blue and light blue. In Fig.5.24.B shows the side view of the kidney where the brown VOI is detected. In Fig.5.24.C the VOIs blue and purple are showed. Fig.5.25.C is a 3D view of the container where all the VOIs are observed in line, from right to left: yellow, red, purple, orange, pink, blue, brown, light blue and green. The voltage is 75 kV, the exposition time is 1500 ms and the spatial resolution is 100 µm.

Any of these 9 VOIs have CT values in the range of ice CT values, so it was difficult to assign which VOIs correspond to the drops inserted. The interpretation we have done of it is that some drops have been divided into two drops. According to the proximity of some of the drops and the volume detected in them, we have grouped together some of the drops. This can be easily understood with image of Fig.5.25. Fig.5.25.A shows the 9 VOIs in a line, corresponding to: yellow (a), red (b), purple (c), orange (d), pink (e), blue (f), brown (g), light blue (g) and green (h). The CT values and volume of these 9 VOIs are showed in table 5.4. We have grouped together VOIs d, e in one VOI, VOIs f and g, and VOIs h and I, having as result 6 VOIs, as showed in Fig 5.25.B. The corresponding detected volumes of those joined VOIs are showed in table 5.5. The VOIs have been assigned to the injected drops according to the detected volume and their position.

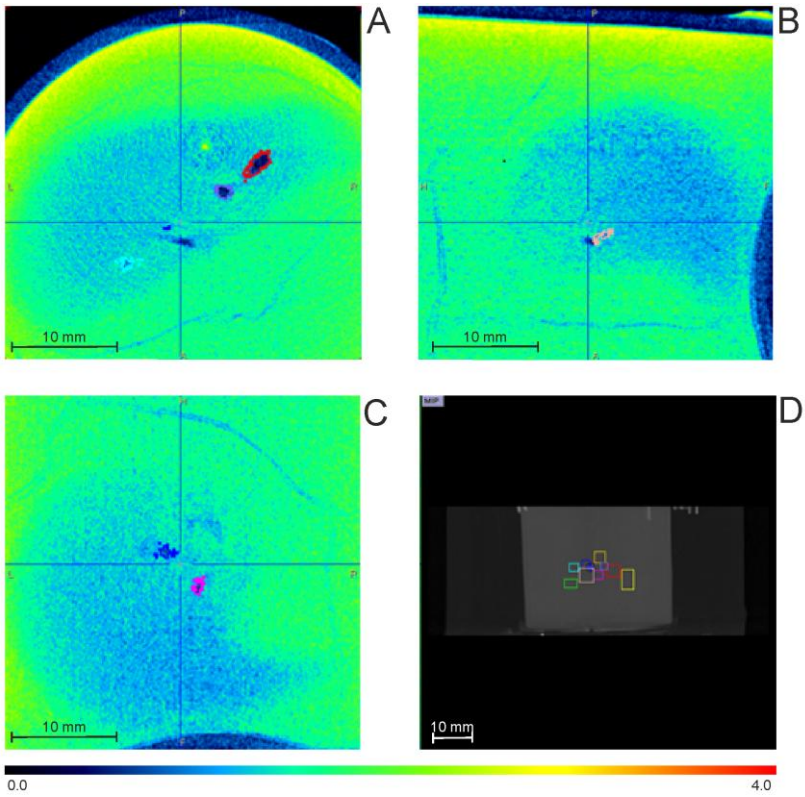

Figure 5.24. CT image of a slice of the kidney C, loaded to 55% v/v Me_2SO, in which has been inserted six drops of water and then cooled to -196 °C. The image was taken at -140 °C. The image uses the cold scale and the spatial resolution is 100 µm

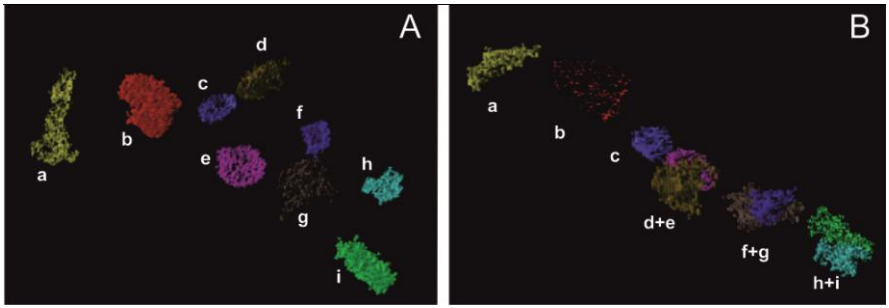

Figure 5.25. (A): 9 VOIs found in kidney B, data in table 5. (B) 6 VOIs after joining some VOIs of (A)

Fig.5.26 shows the 3D image of the kidney C with the VOIs, showing only the vowels with a high attenuation. The image show the 9 VOIs detected at the beginning in the same order than Fig.5.25.A. The kidney can be distinguished in a yellow color. This image gives a spatial view of the location of the drops inside the kidney.

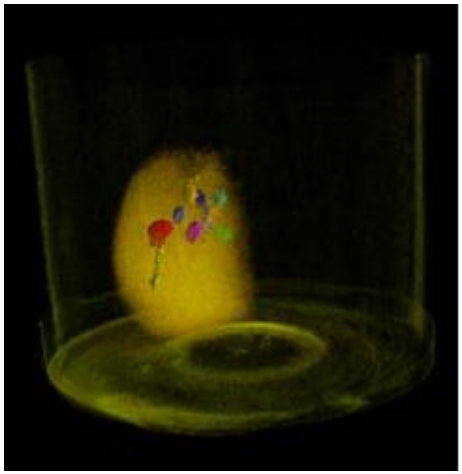

Figure 5.26. CT 3D image of kidney C with VOIs (volumes of interest). The image shows only the vowels with high attenuation from a certain value of CT

The graph of Fig.5.27 shows the average X-ray attenuation for each drop of kidney C of the 9 VOIs found. Attenuation values go from 0.63 to 1.02 CT values, as can be seen in table 5.4. The graph of Fig.5.28 shows the comparison between the volumes of water inserted and the volumes of ice detected in kidney C. There is again too much diffusion of the water before it freezes, with a highest percentage of detection of 70 %. Those graphs are calculated from values showed in table 5.5.

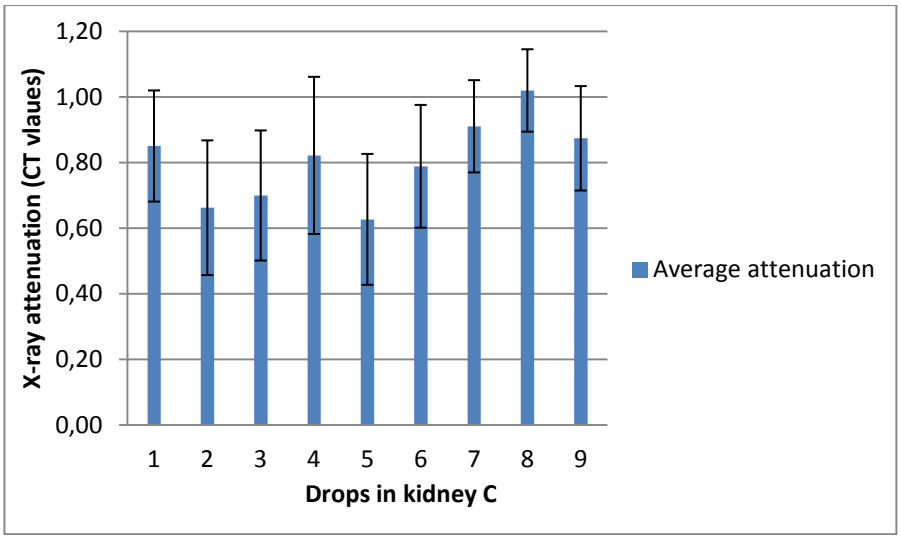

Figure 5.27. The graph shows the average attenuation for each drop in kidney C, in CT values

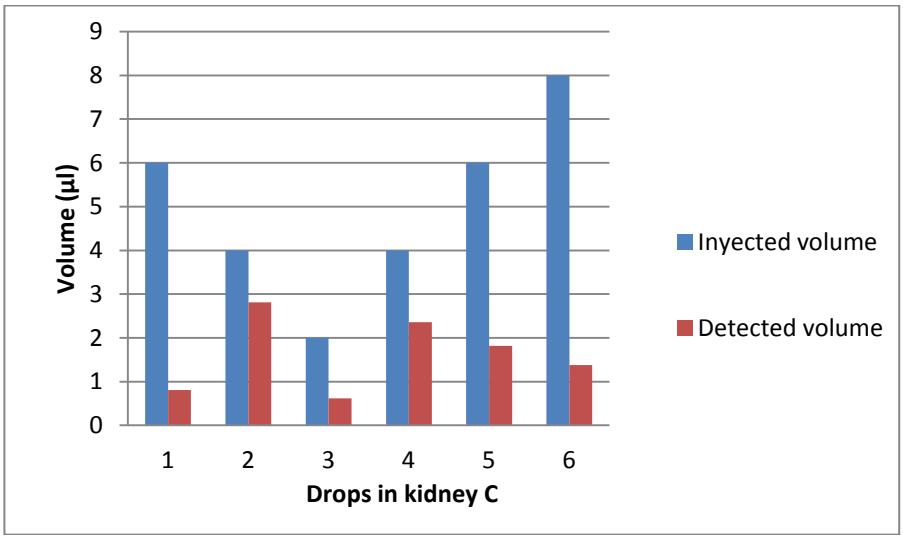

Figure 5.28. The graph compares the volume (µL) of the drops of water inserted (blue columns) versus the volume of ice detected (red columns) in kidney C. The values of the volumes are also showed in table 5.5

In tables 5.2, 5.3, 5.4 and 5.5 the data of the different drops in the kidneys A, B and C are showed. For tables 5.2 and 5.3 the number of the drop appears in the first column, in the same order as they were introduced in line inside the kidney. The next column indicates the volume of water inserted with the syringe. The next one shows the volume of ice detected, calculated from the VOIs. The following column shows the percentage of detection. Next column shows the average attenuation for each drop, in CT values. In the following column, the standard deviation of the attenuation values of the previous column. The last column indicates the number of voxels inside the VOI.

Kidney A						
Drop	Inyected volume (µl)	Detected volume (µl)	Percentage of detection (%)	Averaged attenuation (CT values)	Attenuation SD (CT)	Points (voxels)
1	2	0,28	14,00	0,90	0,14	2250
2	2	0,91	45,50	0,82	0,20	7273
3	4	0,82	20,50	0,80	0,19	6541
4	6	1,43	23,83	0,65	0,19	11426
5	8	1,73	21,63	0,77	0,20	13813
6	6	1,67	27,83	0,75	0,21	13377
7	4	0,91	22,75	0,71	0,18	7308
8	2	0,18	9,00	0,88	0,16	1424

Table 5.2. Relevant data of drops of water in kidney A calculated from the VOIs (volumes of interest)

Kidney B						
Drop	Inyected volume (µl)	Detected volume (µl)	Percentage of detection (%)	Averaged attenuation (CT values)	Attenuation SD (CT)	Points (voxels)
1	2	1,34	67,00	0,56	0,18	2250
2	2	1,38	69,00	0,65	0,20	7273
3	4	0,42	10,50	0,95	0,20	6541
4	6	0,77	12,83	0,86	0,21	11426

Table 5.3. Relevant data of drops of water in kidney B calculated from the VOIs (volumes of interest)

Kidney C						
VOIs	Inyected volume (µl)	Detected volume (µl)	Percentage of detection (%)	Averaged attenuation (CT values)	Attenuation SD (CT)	Points (voxels)
(a)	…	0,81	…	0,85	0,17	811
(b)	…	2,81	…	0,66	0,21	2810
(c)	…	0,62	…	0,70	0,20	617
(d)	…	1,10	…	0,82	0,24	1101
(e)	…	1,26	…	0,63	0,20	1263
(f)	…	0,57	…	0,79	0,19	573
(g)	…	1,25	…	0,91	0,14	1248
(h)	…	0,40	…	1,02	0,13	397
(i)	…	0,98	…	0,87	0,16	979

Table 5.4. Relevant data of drops of water in kidney C calculated from the VOIs (volumes of interest)

Kidney C				
VOIs	Drop	Inyected volume (µl)	Detected volume (µl)	Percentage of detection (%)
(a)	1	6	0,81	13,52
(b)	2	4	2,81	70,25
(c)	3	2	0,62	30,85
(d + e)	4	4	2,36	59,00
(f + g)	5	6	1,82	30,33
(h + i)	6	8	1,38	17,25

Table 5.5. Detected volumes and percentage of detection in kidney C after joining and reorganizing VOIs from table 5.4

5.2.5. Group 5: kidney loaded with a 60% v/v CPA solution at -20 °C, cooled slowly to -140 °C in vapors of liquid nitrogen and then warmed up to 5 °C.

In this group of experiments we show the capability of a layer of ice detection of 100 µm of thickness. Moreover, the kidney was imaged at some points during the warming process.

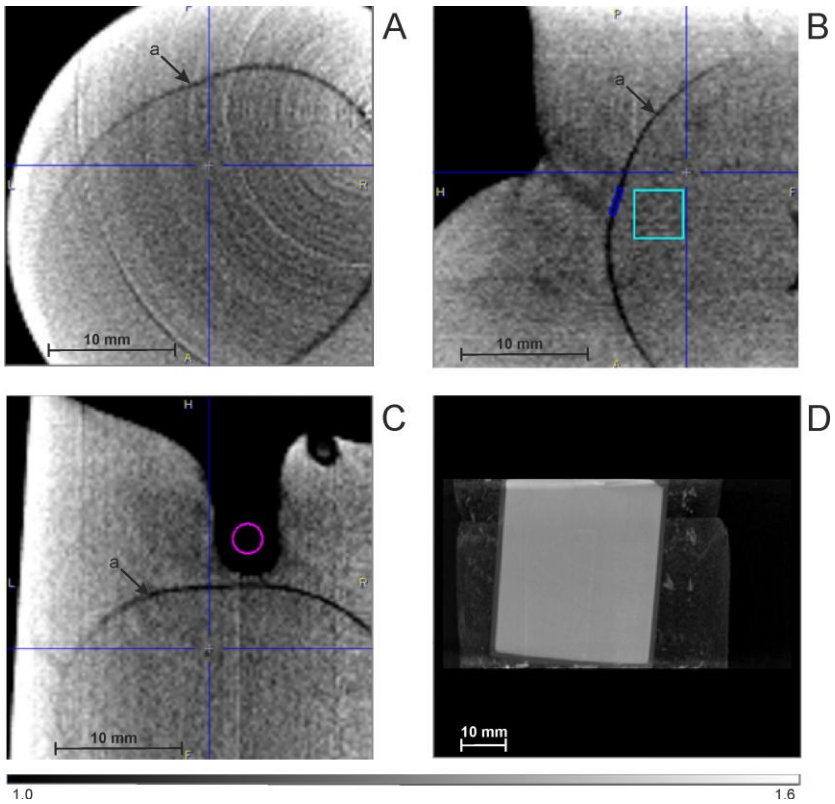

Figure 5.29. Image obtained at -130 °C. A layer of ice of 100 µm thickness can be seen around the kidney. 0.2 The image uses the gray scale and the spatial resolution is 200 µm

Fig.5.29 shows the image of the three views of the kidney at -130 °C. The image uses the gray scale. In Fig.5.29.A the outline of the kidney is observed in black (a), while the kidney and the solution outside it appear in gray. In order to find out what that layer around the kidney was, VOIs were applied

to measure the average CT values of the solution, air, ice and the layer, to compare values. Fig.5.29.B shows the VOIs of the solution inside the kidneys (light blue), and layer around the kidneys (blue). In the view of Fig.5.29.C is seen the VOI corresponding to air (pink). It is observed that the solution has vitrified with an irregular shape, showing a cavity in the middle of the solution. The container was not totally vertical while cooling into the vapors, and it seems some movements of the solution happened while increasing the viscosity. Fig.5.29.D shows a 3D image of the container, created by the CT scan. The average of the CT values were 0.6 +/- 0.2 CT for the layer, 0.7 +/- 0.1 CT for ice, 0.5 +/- 0.1 CT for air and 1.5 +/- 0.2 for the solution. We conclude that the layer around the kidney is ice and it has 0.1 mm of thickness. The explanation we have is the following: the kidney was immersed in the solution at -20 ^{o}C, we took it out and placed it in a pre-cooled plate to clean it, and immediately put it back into the solution. During the time that the kidney was in the atmosphere, around 3-4 minutes, the water in the air condensed and formed a tiny layer of ice around the kidney. The kidney was put it back at -20 ^{o}C and then cooled until -130 ^{o}C so the layer of ice remained around the kidney. That is why we can see the outline of the kidney, because this is the first time we have seen it in our images. However, we analyzed all the layers of the kidney and we did not have evidence of presence of other ice inside the kidney. One reason could be that, if there were some ice crystals, they would be smaller than 0.1 mm. Moreover, there is too much noise in the images. The voltage is 75 kV, the time of exposition is 1500 ms and the spatial resolution is 200 µm.

Then, we decreased the nitrogen flow until the kidney warmed up to -55 ^{o}C, and we imaged it. It must be taken into account that the temperature is measured outside the kidney's vial, so the temperature inside it was probably lower, since the thermal inertia of the solution and kidney are greater. The result of that image can be seen in Fig.5.30.

Fig.5.30 shows the image of the kidney at -55 ^{o}C and it uses the cold scale. We can observe that the layer of ice is still detected. We can see the same part of the layer (a) in the three views, Fig.5.30.A, Fig.5.30.B and Fig.5.30.C. We can also observe the fat of the kidney (b), in Fig.5.30.B and Fig.5.30.C. The solution is not yet vitrified but is still very viscous, as it can be

appreciated in Fig.5.30.B, since the surface is not totally horizontal yet. Although a different color can be observed inside the kidney, we cannot confirm whether there is ice or not inside it, due to the presence of noise and artifacts. This could be solved with a better and longer reconstruction of the image. The voltage is 75 kV, the time of exposition is 1500 ms and the spatial resolution is 200 µm.

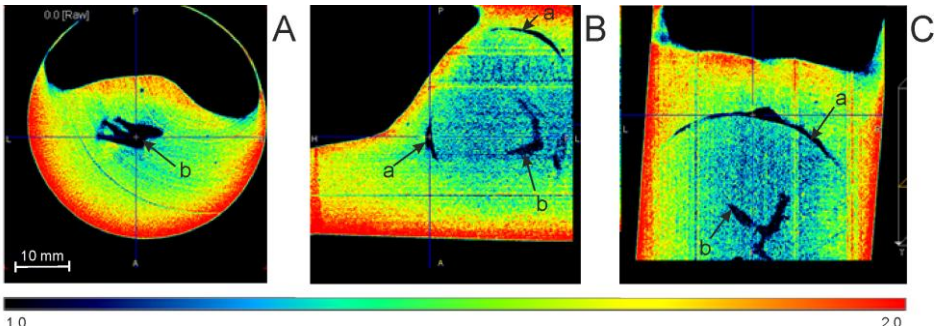

Figure 5.30. Image of the kidney at -55 ^{o}C. The layer of ice around the kidney has increased. The image uses the cold scale and the spatial resolution is 200 µm

Finally we took another image at around + 5 ^{o}C. At that temperature the layer of ice should have melt. The image can be seen in Fig.5.31, where the image uses the cold scale.

In Fig.5.31, we can still observe a small part of the layer of ice around the kidney (a). Although the temperature outside is +5 ^{o}C, the temperature of the kidney is probably lower, so that can be the reason why not all the layer of ice has disappeared. In Fig.5.31.A, the top outline of the kidney can be seen, since the solution is already liquid and it does not cover the kidney any more. In Fig.5.31.B, apart from the outline of the kidney (a), the presence of some fat can also be observed (b). Fig.5.31.B shows another view of the container, where part of the ice of layer is detected (a). Fig.5.31.D is a 3D image of the container at the region where the sample is. The voltage is 75 kV, the time of exposition is 500 ms and the spatial resolution is 200 µm.

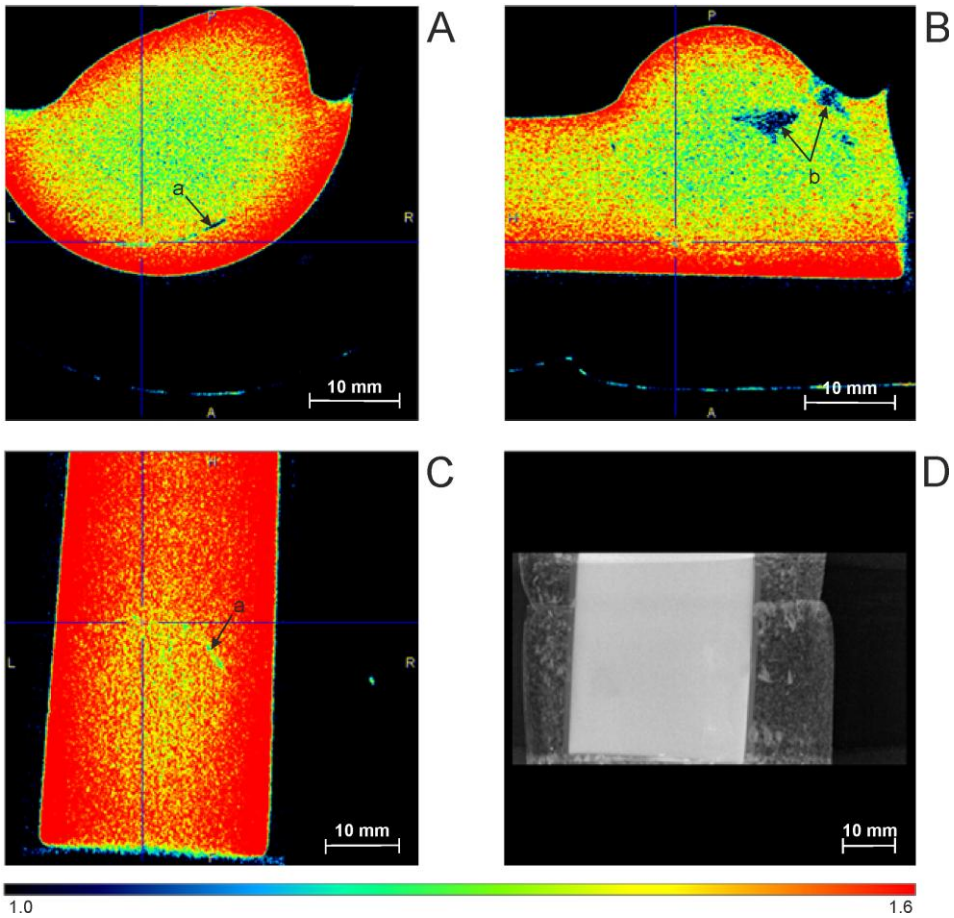

Figure 5.31. Image of the kidney at +5 °C. Some parts of the layer of ice around the kidney can be still be seen. The image uses the cold scale and the spatial resolution is 200 µm

5.3. Perfusion of a rabbit kidney with a Me_2SO solution, at 20 °C.

In this experiment we perfused a rabbit kidney with the equilibrium vitrification system described in section 4.7. The description of the experiment is in sub-section 4.7.5. The perfusion of the kidney begins with a 20% v/v Me_2SO solution, and it goes until a concentration of 70% v/v in 2 hours. The kidney was introduced in the container, previously loaded of

20% v/v Me_2SO, and imaged. The kidney was imaged again after an hour of the perfusion and a third time at the end of the perfusion process.

In Fig.5.32 the three images of the kidney were observed. The images use the cold scale from 0.0 to 2.3 CT values. The voltage is 65 kV, the time of exposition is 500 ms and the spatial resolution is 200 µm. For each measurement the image shows the circular CT bed, the container, the kidney and the input needle attached to the tap of the container. The darkest blue part inside the kidney corresponds to the fat of the kidney. Above the container cap it appears the input tube with the CPA solution. The output needle is not observed because it is placed behind the input needle. However the output tube can be observed at the right of the input tube, above the cap.

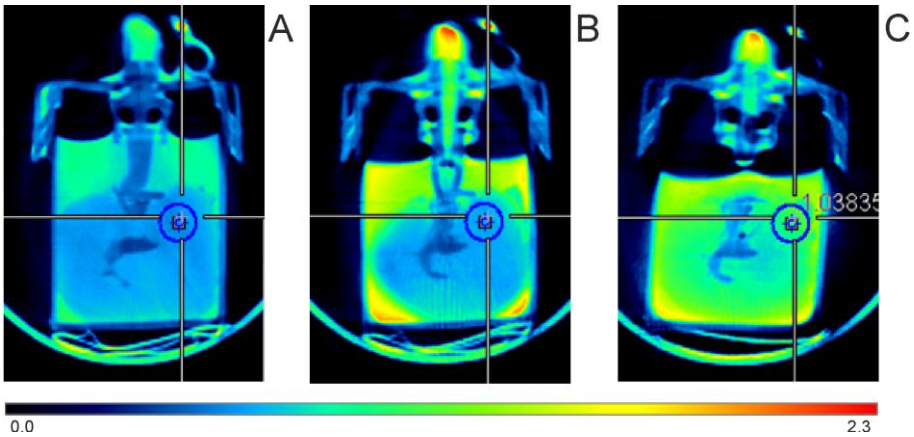

Figure 5.32. CT images of a rabbit kidney during perfusion with Me_2SO from 20% v/v to 70% v/v in 2h. The images are taken at the beginning of the perfusion (A), after 1h perfusion (B), and 3 h after the end of the process (C)

Fig.5.32.A shows the image of the kidney at the beginning of the perfusion. The kidney appears in a dark blue, which indicates a lower attenuation, and therefore a lower CPA concentration, than the solution around. This is because the solution around is 20% v/v Me_2SO. In Fig.5.32.B, the solution around is more concentrated, with a green yellow color. However the kidney shows a blue color, with a lighter blue than the image of Fig.5.32.A. After 1 hour of perfusion the concentration that the pumps send to the

container corresponds to 55% v/v Me_2SO, however, the kidney takes a time to equilibrate with the solution around. In Fig.5.32.C, the outer of the kidney shows the same color than the solution around, which means that the kidney was totally equilibrated with the solution around. However the core of the kidney shows a lighter blue color, with exception of the fat, which appears in the same color of Fig.5.32.A and Fig.5.33.B. It seems that the kidney was equilibrated topically at the end of the process.

We have also measured the X-ray attenuation value for the three images of Fig.5.32. The value has been measured locally at the same point for the three images, where the pointer marks. For Fig.5.32.A, the attenuation value was 0.58 CT values. In the case of Fig.5.32.B, this value increased to 0.66 and in the image of Fig.5.32.C, the value is 1.04 CT values. These values do not correspond to the values of the calibration curve of Fig.5.2. This experiment was performed previously to those of the calibration curve. After the perfusion experiment, the set up was improved and some technical modifications were made to the CT device. This experiment was not repeated after the calibration of the device because of technical difficulties of obtaining the organs and the proceeding of the whole experiment. However, the CT values measured at the same point of the kidney during perfusion show how the attenuation has increased during this process, showing a higher concentration inside the kidney as the process takes place. This proves this method could be an effective way to measure the time needed to a tissue to equilibrate with the CPA concentration that the pumps send in a certain time.

6. Conclusions

6.1. CPA concentration measurements.

According to the results of the CPA concentration measurements, we can affirm that Me_2SO concentrations can be measured in solutions and tissues by X-ray Computed Tomography techniques, by using low acceleration voltage. The images obtained show that X-ray attenuation is proportional to the Me_2SO concentration, which allows us to create calibration curves. In this way, for any sample imaged we are able to know its CPA concentration according to its X-ray attenuation value. The reproducibility of the samples has been proved by obtaining similar attenuation values for the same samples in different measurements.

Moreover, different Me_2SO solutions have been measured in different containers and volumes, from 200 µl up to 20 ml volumes. In all experiments, images obtained show an attenuation proportional to the CPA concentration, independently of the container or volume. However, there are some artifacts and noise that could be improved to obtain better quality in the images. These errors are related to the beam hardening effect, and consist on attenuation values not corresponding to the attenuation values of those vowels in the area around the boundary container. As we have explained in Chapter 3, the attenuation depends on the distance to the surface of the object penetrated by the beam, however this effect makes the relation between attenuation and material thickness not linear. The beam hardening effect could be minimized with filters and better image reconstruction software.

We have also proved the effect of the temperature on the CT measurements. The range of temperature we were interested in was below the glass transition temperature, usually below -120 ^{o}C in concentrated CPA solutions. To that end we have developed a cooling system to combine with the CT technology. Thanks to this system we have also proved that Me_2SO concentrations can be also detectable at cryogenic temperatures, specifically at -140 ^{o}C. The results show the attenuation is also proportional to the CPA concentration, although the attenuation values are slightly higher at low temperatures. In order to determine the CPA calibration at any temperature, calibration curves should be done at different temperatures. In this way the correlation factor for the temperature can be calculated and applied to the attenuation values of a sample at a particular temperature.

Lastly, experiments with tissues, in particular rabbit kidneys, show that CT technology may be applied to create CPA concentration maps to verify if tissues were equilibrated to the desired CPA concentration. In this way this technology could be used to improve protocols of cryopreservation of large tissues and organs.

6.2. Ice detection measurements.

The results obtained in the ice detection experiments prove that small volumes of ice can be detected inside Me_2SO solutions and tissues.

In the preliminary experiments, images show that water is detectable inside Me_2SO solutions, with much lower attenuation than the Me_2SO solutions. We performed different experiments to find out which minimum volumes of water we were able to detect. Results prove that volumes of water up to 1 µl, inside a capillary, in concentrated Me_2SO solutions, were detectable by the computed tomography technique. Moreover we performed the same experiments with capillaries inside tissues, rabbit kidneys in our case. The images proved that this technique was able to detect volumes up to 1 µl of water also inside tissues loaded with concentrated Me_2SO solutions.

Since ice is pure water, ice should be detected in Me_2SO solutions too. Although water and ice have different densities, those differences are not

representative especially if we assume that at our work energies the densities are not the limiting factor for the attenuation, as we expose in Chapter 3.

To validate this hypothesis, we performed experiments by inserting drops of water in kidneys loaded with concentrated Me_2SO solutions at -20 ^{o}C and then cooled to -196 ^{o}C. We wanted to produce small ice crystals inside the tissue. Images show the detection of all the drops of water in most cases. Thanks to the VOIs tool of the software of images analysis (PMOD), we are able to estimate the volumes of the detected drops. The results show a low percentage of detected volumes compared to inserted volumes. However, the method proves the ability to detect ice crystals inside tissue, which was our main aim, even though it is in a qualitative way. Another fact is that the expanding process of ice was not taken into account in the calculated volumes, although the proportion was kept for each drop in each experiment. The 3D image rendering tool also allows us to create 3D images of the kidneys where a spatial distribution of the ice drops is visualized.

To conclude, we are able to detect ice crystals in tissues loaded with Me_2SO solutions, although in a qualitative way and we can visualize the distribution of those ice crystals inside the tissue. However, several technical aspects can be improved, such as the precision of ice crystals volume and the noise of the images. There was also another problem detected associated with an uneven cooling of the CT bed. Since the insulating sleeve of the N_2 gas tube inside the CT bed was not exactly symmetric, a small gradient of temperature was created in the methacrylate CT bed. The temperature at different points of the CT bed was measured during the cooling process and we found a few degrees of difference among different sides of the CT bed. Due to the thermal expansion of the methacrylate, there was a contraction of the coolest side of the CT bed and it generates a movement of the bed during imaging. This causes some noise on the images too. After investigating different materials with a low thermal expansion coefficient, we found that a more appropriate material would be carbon fiber, and therefore the substitution of the actual CT bed by a carbon-fiber CT bed would solve noises associated to bed movements and improve the quality of the images, and therefore the information obtained by them.

One of the possible applications of the detection of ice by means of CT technology is the assessment of vitrified tissues. In this way, it would be possible to evaluate ice damages during the cooling and warming processes. This could be very interesting and useful since there are some evidences that during the warming process it is likely that the devitrification happens, and therefore more risk of ice formation.

6.3. Equilibrium vitrification.

One of the most interesting uses of the CT technology is its application to the equilibrium vitrification process to cryopreserve complex tissues and bulky organs. As we have explained, during this process we have to keep under control two parameters: the CPA concentration and the temperature, in order to keep the sample always above the liquidus curve avoiding ice formation.

We have developed an equilibrium vitrification system where the cooling agent is nitrogen gas pre-cooled with liquid nitrogen. The nitrogen gas is sent to the container where the sample is through a few tubes. The temperature is measured with a thermocouple and the elements to control the cooling or warming rate are two solenoid valves connected to the control software. If the sample needs to be cooled faster the valve of the pre-cooled nitrogen gas will open and if the sample needs to be warmed, the valve of the warm nitrogen gas will open.

In this way, we could say that the control of the temperature is simple. However the CPA concentration measurement is more difficult to control, especially in bigger samples or vascularised organs where the perfusion of the CPA solution is made by the vascular system. As we have seen in Chapter 2, the knowledge of the distribution inside the organ is essential to achieve a successful cryopreservation. With the equilibrium vitrification system we can control the CPA concentration which is sent to the samples, however, we do not know the time needed for the sample to equilibrate with that concentration. Applying the CT measurements technique, we could know the spatial CPA concentration in each point of the tissue or organ according to the calibration curve attenuation-CPA concentration. In this way, we can create a cooling and warming profile taking into account

the time needed for the sample to equilibrate with the CPA concentration which corresponds to each temperature.

Moreover, the use of the CT technique can be also applied to detect ice formation during the equilibrium vitrification process. In this way, if during the cooling process of the sample ice crystals are detected, it means that the organ did not achieve the CPA concentration needed according to that temperature, and therefore, the cooling rate was too fast. From that it is possible to adjust and tune the parameters necessary of the cooling and warming processes, as well as the CPA perfusion protocol. Thus the application of the CT technology will allow us to follow the CPA equilibrium curve very closely, avoiding the formation of ice in all points of the sample.

One of the main advantages of the CT technique is that it is a non invasive method, so there is no risk of structure changes in the sample. Moreover, it is a very flexible method that can be applied to any kind of sample, and in combination with the equilibrium vitrification system could be adjusted to create vitrification protocols according to different size and kind of sample.

The equilibrium vitrification technique has also some aspects to improve. Although we have proved that the system is able to achieve temperatures below -130 ^{o}C with our cooling system, at temperatures lower than -20 ^{o}C the solutions become too viscous and the pressure loss of the tubes will increase. We need to further study the response of the pumps under those situations. Moreover, the material resistance to those low temperatures during a long period of time must be studied too.

Regarding the CT technology, although the study presented here proves its ability to measure CPA concentration and detect ice formation in tissues, the technique can be improved with better reconstruction software and other technical parameters. In this way the artifacts and noise of the images would be minimized, and therefore a better quality of the images could be obtained. Thus, a better precision in the CT measurements would be achieved.

Figures and tables

Figures:

Tables:

References

1. R.K. Andjus, V. Rajevski, Resumption of heart beats after thawing from -196°C. (Experiments on isolated frog hearts.), Progr. Refrig. Sci. Technol. Proc. Int. Congr. Refrig.10th (1959) 632.

2. W.J. Armitage, S.C. Hall, C. Routledge, Recovery of Endothelial Function after Vitrification of Cornea at -110°C, Investigative Ophthalmology & Visual Science 43 (2002) 2160-2164.

3. F.G. Arnaud, B. Khirabadi, G.M. Fahy, Physiological evaluation of a rabbit kidney perfused with VS41A, Cryobiology 46 (2003) 289–294.

4. M.J. Ashwood-Smith, Viability of mouse bone marrow frozen to -79°C in the presence of dimethyl sulphoxide, J. Physiol. (London) 165 (1961a) 26P-27P.

5. X. Bai et al., Analysis of electromagnetic heating patterns inside a cryopreserved organ, J Biomed Eng 14 (1992) 459-466.

6. H.R. Bamer, Perfusion and freezing of the rat heart, in: Organ perfusion and preservation, J. C. Norman et al., Eds., (1968) 717-730, Appleton-Century-Crofts, New York.

7. E.A.J. Bateson et al., Permeation of Rabbit Common Carotid Arteries with Dimethyl Sulfoxide, Crybiology 31 (1994) 393-397.

8. Baudot et al., Towards whole sheep ovary cryopreservation, Cryobiology 55 (2007) 236–248.

9. M.J. Berger et al., XCOM: Photon Cross Section Database (version 1.5). [Online] Available: http://physics.nist.gov/xcom [Monday, 20-May-2013 13:01:50 EDT]. National Institute of Standards and Technology, Gaithersburg, MD (2010).

10. N.P. Bidault, B.E. Hammer, A. Hubel, Rapid MR Imaging of Cryoprotectant Permeation in an Engineered Dermal Replacement, Cryobiology 40 (2000) 13–26.

11. R.E. Billingham, P.B. Medawar, The freezing, drying and storage of mammalian skin. J. Exp. Biol.29 (1952) 454-468.

12. J.C. Bischof et al., Use of X-ray Tomography to Map Crystalline and Amorphous Phases in Frozen Biomaterials, Annals of Biomedical Engineering 35, (2007) 292–304.

13. A. Bonetti et al., Ultrastructural evaluation of human metaphase II oocytes after vitrification: closed versus open devices, Fertility and Sterility 3 (2011) 928-935.

14. P. Boutron, A. Kaufmann, Stability of the Amorphous State in the System Water- 1,2-Propanediol, Cryobiology 16 (1979) 557-568.

15. P. Boutron, P. Mehlt, Theoretical Prediction of Devitrification Tendency: Determination of Critical Warming Rates without Using Finite Expansions Cryobiology 27 (1990) 359-377.

16. K.G. Brockbank, Y.C. Song, Morphological analyses of ice-free and frozen cryopreserved heart valve explants, Journal of Heart Valve Disease 13 (2004) 297-301.B.

17. K.G.M. Brockbank et al., Comparison of heart valve cryopreservation and storage methods, Cryobiology 55 (2007) 342-343.

18. R.A. Brooks, G. Di Chiro, Beam Hardening in X-ray Reconstructive Tomography, Phys. Med. Biol. 21 (1976) 390-398.

19. G. Bryant, DSC Measurements of Cells Suspensions during Successive Freezing Runs: Implications for the Mechanisms of Intracellular Ice Formation, Cryobiology 32 (1995) 114-128.

20. P.J. Connaughton, F.J. Lewis, Use of glycerol and chloroform in heart preservation by freezing, Surg. Forum 12 (1961) 177-179.

21. B. Courbiere et al., Follicular viability and histological assessment after cryopreservation of whole sheep ovaries with vascular pedicle by vitrification, Fertility and Sterility 84 (2005) 1065-1071.

22. T.M. Ching, W.H. Slabaugh, X-ray diffraction analysis of ice crystals in coniferous pollen, Cryobiology 6, (1966) 321-327.

23. R.H. Dietzman et al. Long-term functional success following freezing of canine kidneys, Surgery 74 (1973) 181-189.

24. K.R. Diller, E.G. Cravalho, C.E. Huggins, An experimental study of freezing erythrocytes, Medical and Biological Engineering (1976) 321-326.

25. K.R. Diller, Modeling of bioheat transfer processes at high and low temperatures, in: Cho YI, Ed. Bioengineering Heat Transfer 22 (1992) 157-357, San Diego, CA: Academic Press.

26. I. Djerassi, A. Roy, A Method for Preservation of Viable Platelets: Combined Effects of Sugars and Dimethylsulf oxide, Blood 22 (1963) 703-717.

27. R.M. Dougherty, Use of dimethyl sulphoxide for preservation of tissue culture cells by freezing, Nature 193 (1962) 550-532.

28. B.C. Elford, Diffusion and distribution of water and added non-electrolytes in muscle, PhD thesis, University of London, 1969.

29. B.C. Elford, C.A. Walter, Effects of electrolyte composition and pH on the structure and function of smooth muscle cooled to −79 ^{o}C in unfrozen media, Cryobiology 9 (1972) 82–100.

30. S. Englich., Ch. Körber, G. Rau., An intracellular phase change in lymphocytes detected by cryomicroscopy and differential scanning calorimetry, Cryobiology 25 (1988): 511.

31. Eroglu et al., Successful Cryopreservation of Mouse Oocytes by Using Low Concentrations of Trehalose and Dimethylsulfoxide, Biology of Reproduction 80 (2009) 70-78.

32. S. Evans, Elecromagnetic rewarming: the effect of CPA concentration and radio source frequency on uniformity and efficiency of heating, Crobiology 40 (2000) 126-138.

33. G.M. Fahy et al., Vitrification as an Approach to Cryopreservation, Cryobiology 21 (1984) 407-426.

34. G.M. Fahy, D.I. Levy, S.E. Ali, Some Emerging Principles Underlying the Physical Properties, Biological Actions, and Utility of Vitrification Solutions, Cryobiology 24(1987), 196-213.

35. G.M. Fahy, J. Saur, R.J. Williams, Physical problems with the vitrification of large bological systems, Cryobiology 27 (1990) 66-74.

36. G.M. Fahy, S.A. Ali Cryopreservation of the Mammalian Kidney II. Demonstration of Immediate *ex Vivo* Function after Introduction and Removal of 7.5 *M* Cryoprotectant, Cryobiology 35 (1997) 114-131.

37. G.M. Fahy et al., Improved vitrification solutions based on the predictability of vitrification solution toxicity, Cryobiology 48 (2004), 22-35.

38. G.M. Fahy et al., Cryopreservation of organs by vitrification: perspectives and recent advances, Cryobiology 48 (2004)157-178.

39. G.M. Fahy et al., Physical and biological aspects of renal vitrification, Organogenesis 5:3 (2009) 167-175.

40. J. Farrant, Mechanism of cell damage during freezing and thawing and its prevention, Nature 205 (1965) 1284-1287.

41. M. Forsyth, D.R. MacFarlane, Recrystallization revisited, Cryo Lett.7 (1986) 367-378.

42. B.J. Fuller, A.L. Busza, E. Proctors, Studies on Cryoprotectant Equilibration in the Intact Rat Liver Using Nuclear Magnetic Resonance Spectroscopy: A Noninvasive Method to Assess Distribution of Dimethyl Sulfoxide in Tissues, Cryobiology 26(1989) 112-118.

43. F.M. Guttman et al., Survival of canine kidneys after treatment with dimethyl sulphoxide, freezing at -80°C and thawing by microwave illumination, Cryobiology 14 (1977) 559-567.

44. E .M. Guttman, N.Segal, J. Borzone. In: Organ Preservation II, D. E. Pegg and I.A. Jacobsen Eds., Cryopreservation of canine kidneys with dimethylsulphoxide: Further studies (1979) 184, Churchill Livingstone, Edinburgh.

45. Halasz et al., Whole organ preservation. II Freezing studies, Surgery 61 (1967) 417-21.

46. R. Hamilton, H.I. Holst, H.B. Lehr, Successful preservation of canine small intestine by freezing, Journal of Surgical Research 14 (1973) 313–318.

47. G.W.H. Höhne, W.F. Hemminger, H.-J. Flammersheim, *Differential Scanning Calorimetry*, 2nd Edition,Springer, Berlin-Heidelberg, 2003.

48. C. J. Hunt, M. J. Taylor, D. E. Pegg, Freeze-substitution and isothermal freeze-fixation studies to elucidate the pattern of ice formation in smooth muscle at 252 K (-21°C), Journal of Microscopy 125 (1982) 177-186.

49. C.J. Hunt, Studies on Cellular Structure and Ice Location in Frozen Organs and Tissues: The Use of Freeze-Substitution and Related Techniques, Crybiology 21, (1984) 385-402.

50. S.A. Isbell et al., Measurement of Cryoprotective Solvent Penetration into Intact Organ Tissues Using High-Field NMR Microimaging, Crybiology 35 (1997) 165-172.

51. I.A. Jacobsen, D.E. Pegg, Cryopreservation of Organs: A Review, Cryobiology 21 (1984) 377-384.

52. J.O.M. Karlsson, E.G. Cravalho, M. Toner, Intracellular ice formation: causes and consequences, Cryo Lett 14 (1993) 323-336.

53. J.O.M. Karlsson et al., Nucleation and Growth of Ice Crystals Inside Cultured Hepatocytes During Freezing in the Presence of Dimethyl Sulfoxide, Biophysical Journal 65 (1993) 2524-2536.

54. J.O.M. Karlsson, E.G. Cravalho, M. Toner, A model of diffusion-limited ice growth inside biological cells during freezing, JAppl Phys 75 (1994) 4442-4455.

55. J.O.M. Karlsson, M. Toner, Long-term storage of tissues by cryopreservation: critical issues, Biomaterials 17 (1996) 243-256.

56. J.O.M. Karlsson, A Theoretical Model of Intracellular Devitrification, Cryobiology 42 (2001) 154-169.

57. A.M. Jr. Karow, W. R Webb, J.B. Stapp, Preservation of hearts by freezing, Arch. Surg. Chicago, 91 (1965) 572-574.

58. A.M. Karow, Jr., M. Shlafer, Ultrastructure-Function Correlative Studies for Cardiac Cryopreservation. IV. Prethaw Ultrastructure of Myocardium Cooled Slowly ($\leq$ 2°C/min) or Rapidly ($\geq$ 70°C/sec) with or without Dimethyl Sulfoxide (DMSO), Cryobiology 12 (1975) 130-143.

59. B.S. Khirabadi, G.M. Fahy, Cryopreservation of the mammalian kidney I. Transplantation of Rabbit kidneys perfused with EC and RPS-2 at 2-4 ^{o}C, Cryobiology 31 (1994) 10-25.

60. B.S. Khirabadi et al., 100% survival of rabbit kidneys chilled to -32 ^{o}C after perfusion with 8 M cryoprotectant at -22 ^{o}C, Cryobiology 31 (1994) 597.

61. T.L. Kieft, T. Ruscetti, Molecular Sizes of Lichen Ice Nucleation Sites Determined by Gamma Radiation Inactivation Analysis, Crybiology 29, (1992) 407-413.

62. F.W. Kleinhans et al.annalys, Analysis of intracellular ice nucleation in *Xenopus* oocytes by differential scanning calorimetry, Cryobiology 52 (2006) 128-138.

63. G.F. Knoll, *Radiation detection and measurement*, 4th Edition, John Willey & Son, New York, 2010.

64. S. Kubota et al., The effect of freeze rate, duration of phase transition and warming rate on survival of frozen canine kidneys, Cryobiology 13 (1976) 455-462.

65. M. Kuwayama et al., Comparison of open and closed methods for vitrification of human embryos and the elimination of potential contamination, Reproductive BioMedicine Online 5 (2005) 608-614.

66. S.P. Leibo, J.J. McGracth, E.G. Cravalho, Microscopic Observation of Intracellular Ice Formation in Unfertilized Mouse Ova as a Function of Cooling Rate, Cryobiology 15 (1978) 257-271.

67. R.L. Levin, E.G. Cravalho, C.E. Huggings, Water transport in a cluster of closely packed erythrocytes at subzero temperatures, Cryobiology 14 (1977) 549-558.

68. K.C. Liu, J.K. Sherman, Ultrastructural Comparison of Freeze-Drying and Freeze-Substitution in Preservation of the Frozen State, Cryobiology 15 (1977) 382-386.

69. J.E. Lovelock, The Protective Action of Neutral Solutes against Haemolysis by Freezing and Thawing, Biochem. J.56 (1954) 265.

70. J.E. Lovelock, M.W. Bishop, Prevention of freezing damage to living cells by dimethyl sulphoxide, Nature 183(1959), 1394-1395.

71. B. Luyet, G. Rapatz, Devitrification of aqueous solutions, Bull. Amer. Phys. Soc.2 (1957) 342.

72. D.R. MacFarlane, Devitrification in Glass-Forming Aqueous Solutions, Cryobiology 23 (1986) 230-244.

73. J.J. MacGrath, Preservation of biological material by freezing and thawing, in: A. Shizter, R.C. Eberhart, Eds. , Heat Transfer in Medicine and Biology 2 (1985) 185-238, New York, Plenum Press.

74. A.P. MacKenzie, T.A. Kuster, B.J. Luyet, Freeze-Fixation at High Subzero Temperatures, Cryobiology 12 (1975) 427-439.

75. T.P. Marsland, S. Evans, D.E. Pegg, Dielectring measurements for the design on an electromagnetic rewarming system, Cryobiology 24 (1987) 311-323.

76. S.R. May, J.F. Wainwright, Optimum warming rates to maintain glucose metabolism in porcine skin cryopreserved by slow cooling, Cryobiology 22 (1985) 196–202.

77. P. Mazur, Cryobiology: the freezing of biological systems, Science 168 (1970) 939-949.

78. P. Mazur, J.A. Kemp, R. H. Miller, Survival of fetal rat pancreases frozen to -78 and -196 ^{o}, Proc. Natl. Acad. Sci. USA 73 (1976) 4105-4109.

79. P. Mazur, The role of intracellular freezing in the death of cells cooled at supraoptimal rates, Cryobiology 14 (1977) 251-272.

80. P. Mazur, Freezing of living cells: mechanisms and implications, Am. J. Physiol.247 (1984) C125-C142.

81. P. Mazur, K.W. Cole, Influence of cell concentration on the contribution of unfrozen fractions and salt concentration to the survival of slowly frozen human erythrocytes, Cryobiology 22 (1985) 509-536.

82. F. Migishima et al., Successful Cryopreservation of Mouse Ovaries by Vitrification, Biology of Reproduction 68(2003) 881–887.

83. S. Mori, J. Choi, J.C. Bischof, Intracellular ice formation and water transport during freezing of human dermal fibroblasts measured using differential scanning calorimetry, Cryobiology 63 (2011) 306-342.

84. K. Muldrew, L.E. McGann, Mechanisms of intracellular ice formation, Biophys. J. 57 (1990) 525-532.

85. K. Muldrew, L.E. McGann, The osmotic rupture hypothesis of intracellular freezing injury, Biophys J.66 (1994) 532-541.

86. S.P. Myers et al., Characterisation of Intracellular Ice Formation in *Drosophila Melanogaster* Embryos, Cryobiology 26 (1989) 472-484.

87. A. Olmo et al., Use of Electrical Impedance Spectroscopy (EIS) to Monitor Cryoprotectant Concentration in Cellular and Tissue Cryopreservation, Cryobiology 61 (2010) 392-392.

88. D.E. Pegg, Banking of cells, tissues, and organs at low temperatures, in: A.U. Smith (Ed.), Current Trends in Cryobiology, Plenum Press, New York, 1970, pp.153–180.

89. D.E. Pegg, M.C. Wusteman, Perfusion of rabbit kidneys with glycerol solutions at 5 ^{o}C, Cryobiology 14 (1977) 168–178.

90. D.E. Pegg, Ice Crystals in Tissues and Organs, in: David E. Pegg, Armand M. Karowjr. (Eds), The Biophysics of Organ Cryopreservation, Plenum Publishing Corporation, 1978, pp.117-136.

91. D.E. Pegg, The effect of cell concentration on the recovery of human erythrocytes after freezing and thawing in the presence of glycerol, Cryobiology 18 (1981)221-228.

92. D.E. Pegg, M.P. Diaper, Measurement of permeation of cryoprotectants in tissues by a gravimetric method, Cryobiology 31 (1994) 571.

93. D.E. Pegg, Immersion weighing as a method for monitoring the permeation of tissues by cryoprotectants, Cryobiology 53 (2006) 383.

94. D.E. Pegg, Monica C. Wusteman, Lihong Wang, Cryopreservation of articular cartilage. Part 1: Conventional cryopreservation methods, Cryobiology 52 (2006) 335–346.

95. D.E. Pegg et al., Cryopreservation of articular cartilage. Part 2: Mechanisms of cryoinjury, Cryobiology 52 (2006) 347–359.

96. D.E. Pegg, L. Wang, D. Vaughan Cryopreservation of articular cartilage. Part 3: The liquidus-tracking method, Cryobiology 52 (2006) 360–368.

97. D.E. Pegg et al., Further work on the cryopreservation of articular cartilage with particular reference to the liquidus tracking (LT) method, Cryobiology 55 (2007) 138-147.

98. D.E. Pegg, The relevance of ice crystal formation for the cryopreservation of tissues and organs, Cryobiology 60 (2010) S36-S44.

99. R.E. Pitt, Thermodynamics and intracellular ice formation, in: Steponkus P. Ed. Advances in Low-Temperature Biology (Vol 1), London, JAI Press, 1992, 63-99.

100. C. Polge, A.U. Smith, A.S. Parkes, Revival of Spermatozoa after Vitrification and Dehydration at Low Temperatures, Nature 164 (1949) 666.

101. W.F. Rall, G.M. Fahy, Ice-free cryopreservation of mouse embryos at -196 ^{o}C by vitrification, Nature 313 (1985) 573-575.

102. P.S. Rao, R.J. Alfidi, The environmental density artifacti: a beam hardening effect in computed tomography, Radiology 141 (1986) 223-227.

103. G. Rapatz, R. Keener, Effect of concentration of ethylene glycol on the recovery of frog hearts after freezing to low temperatures, Cryobiology 11 (1974) 571–572.

104. D.H. Rasmussen, A.P. Mackenzie, Phase Diagram for the System Water-DimethylSulfoxide, Nature 220 (1968) 1315-1317.

105. M.P. Robinson, D.E. Pegg, Rapid electromagnetic warming of cells and tissues, IEEE Trans. Biomed. Eng. 46 (1999) 1414-1425.

106. M.P. Robinson, M.C. Wusteman, L. Wang, D.E. Pegg, Electromagnetic re-warming of cryopreserved tissues: effect of choice of cryoprotectant and sample shape on uniformity of heating, Phys. Med. Biol. 47 (2002) 2311-2325.

107. B. Rubinsky, E.G. Cravalho, B. Micik, Thermal stresses in frozen organs, Cryobiology 17 (1980) 66-74.

108. B. Rubinsky et al., The process of freezing and the mechanisms of damage during hepatic surgery, Cryobiology 27 (1990) 85-97.

109. P.S. Ruggera, G.M. Fahy, Rapid and Uniform Electromagnetic Heating of Aqueous Cryoprotectant Solutions from Cryogenic Temperatures, Cryobiology 27 (1990) 46–78.

110. M. Salehnia, Autograph of Vitrified Mouse Ovaries Using Ethylene Glycol as Cryoprotectant, Exp. Anim. (2002) 509-512.

111. P.D. Schreuders, K.R. Diller, J.J. Beabam Jr., H.M. Paynter, An Analysis of coupled multicomponent diffusion in interstitial tissue, J. Biomech. Eng.116 (1994) 164-171.

112. J.A. Seibert, J.M. Boone. X-Ray Imaging Physics for Nuclear Medicine Technologists. Part 2: X-Ray Interactions and Image Formation. J. Nucl. Med. Technol 33 (2005) 3-18.

113. S. Seki a, F.W. Kleinhans, P. Mazur, Detection of intracellular ice formation in cells of the yeast Saccharomyces cerevisiae by differential scanning calorimetry, Cryobiology 57 (2008) 315–340.

114. S. Seki, P. Mazur, The dominance of warming rate over cooling rate in the survival of mouse oocytes subjected to a vitrification procedure, Cryobiology 59 (2009) 75–82.

115. M.W. Sheiwe, C. Körber, Quantitative Cryomicroscopic Analysis of Intracellular Freezing of Granulocytes without Cryoadditive, Cryobiology 24 (1987) 473-483.

116. G.J. Sherwood, J.R. Flower, Engineering aspects of equipment design for subzero organ preservation, in: D.E. Pegg (Ed.), Organ Preservation, Churchill Livingstone, London, 1973, pp.152–174.

117. M. Shlafer, A.M. Karow, Jr., Ultrastructure-function Correlative Studies for Cardiac Cryopreservation. III. Hearts Frozen to -10 ^{o}C and -17 ^{o}C With and Without Dimethyl Sulfoxide (DMSO), Cryobiology 9 (1972) 38-50.

118. A.U. Smith, M. J. Ashwood-Smith, M. R. Young, Some in vitro studies on rabbit cornea tissue. Exp. Eye Res.2 (1963) 71-87.

119. A.U. Smith, Problems in the resuscitation of mammals from body temperatures below 0 ^{o}C, Proceedings of the Royal Society Series B 147 (1957) 533–544.

120. A.U. Smith, The effects of glycerol and of freezing on mammalian organs, in: A.U. Smith (Ed.), Biological Effects of Freezing and Supercooling, Edward Arnold, London (1961) 247–269.

121. P.-W. So, B.J. Fuller, Hepatic Uptake of Solutes from the Preservation Solution during Hypothermic Storage: A 1H NMR Study in Rat Liver, Cryobiology 42 (2001) 307–313.

122. Y.C. Song et al., Vitreous cryopreservation maintains the function of vascular grafts, Nature Biotechnology 18 (2000) 296-299.

123. S.L. Stott, J.O.M. Karlsson, Visualization of intracellular ice formation using high-speed video cryomicroscopy, Cryobiology 58 (2009) 84–95.

124. M. Sugimoto et al., Development of infantile rat ovaries autotransplanted after cryopreservation by vitrification, Theriogenology 53 (2000) 1093–1103.

125. M.J. Taylor, A.L. Busza; A convenient, non-invasive method for measuring the kinetics of permeation of dimethyl sulfoxide into isolated corneas using NMR spectroscopy, Cryo-Letters 13 (1992) 273–282.

126. M. Toner, E.G. Cravalho, M. Karel, Thermodynamics and kinetics of intracellular ice formation during freezing of biological cells, J Appl Physic 67 (1990) 1582-1592 (erratum: 70 (1991) 4653).

127. G. Vajta et al., Open Pulled Straw (OPS) Vitrification: A New Way to Reduce Cryoinjuries of Bovine Ova and Embryos, Molecular Reproduction and development 51 (1998) 51-54.

128. C.A. Walter, S.C. Knight, J. Farrant, Ultrastructural Appearance of Freeze-Substituted Lymphocytes Frozen by Interrupting Rapid Cooling with a Period at -26 ^{o}C, Cryobiology 12 (1975) 103-109.

129. R.Y. Wang et al., Study on fish embryo responses to the treatment of cryoprotective chemicals using impedance spectroscopy, Eur Biophys Journal 35 (2006) 224–230.

130. B. Wowk et al., Vitrification Enhancement by Synthetic Ice Blocking Agents, Cryobiology 40 (2000) 228–236.

131. B. Wowk, Thermodynamic aspects of vitrification, Cryobiology 60 (2010) 11–22.

132. T. Yoshimori et al., Detection of the eutectic crystallization by impedance measurement, Cryobiology 55 (2007) 324–378.

133. T. Zhang et al., Development of a new rapid measurement technique for fish embryo membrane permeability studies using impedance spectroscopy, Theriogenology 66 (2006) 982–988.

Anexes

Publications in conferences.

Measurements of the concentration of cryoprotectant agents in organs by X-ray computed tomography (CT).

Ramón Risco[1], Marcin Balcerzyk[2], Ariadna Corral[1], Joaquín Cobos[2], Alberto Olmo[1], Francisco García-Arguello[2].

[1]CryoBioTech, Departamento de Física Aplicada III, Universidad de Sevilla, Camino de los Descubrimientos s/n, 41092 Sevilla.
[2]Centro Nacional de Aceleradores (CNA), Parque Tecnológico Cartuja 93, C/Thomas Alva Edison Nº 7, 41092 Sevilla.

Poster

Society for Cryobiology, CRYO 2010, Annual Meeting, Bristol, United Kingdom.

Measurement of CPA concentrations by means of Computed Tomography: theory and experiments.

Ramón Risco[1], Joaquín Cobos[2], Ariadna Corral[1], David Regalado[1], Marcin Balzerzyk[2].

[1]CryoBioTech, Departamento de Física Aplicada III, Universidad de Sevilla, Camino de los Descubrimientos s/n, 41092 Sevilla.
[2]Centro Nacional de Aceleradores (CNA), Parque Tecnológico Cartuja 93, C/Thomas Alva Edison Nº 7, 41092 Sevilla.

Talk

Society for Low Temperature Biology, Symposium 2011, Linnean Society, London, United Kingdom.

Application of X-Ray Computed Tomography to organ cryopreservation.

Ariadna Corral[1], Marcin Balcerzyk[2], Reyes López[1], Isabel Fernandez[2], Angel Parrado[2], Laura Fernández[2], Ramón Risco[1].

[1]CryoBioTech, Departamento de Física Aplicada III, Universidad de Sevilla, Camino de los Descubrimientos s/n, 41092 Sevilla.

[2]Centro Nacional de Aceleradores (CNA), Parque Tecnológico Cartuja 93, C/Thomas Alva Edison Nº 7, 41092 Sevilla.

Poster, Award Best Poster Prize
Advances in Low Temperature Biology, Society for Low Temperature Biology Conference 2012, Linnean Society, London, United Kingdom.

Adaptation of a commercial diathermy machine for radiofrequency warming of vitrified organs.
Brian Wowk[1] and Ariadna Corral[2]

[1]21st Century Medicine, Inc., Fontana, California 92336, U.S.A.
[2]CryoBioTech, Departamento de Física Aplicada III, Universidad de Sevilla, Camino de los Descubrimientos s/n, 41092 Sevilla.

Talk
Society for Cryobiology, CRYO 2013, 50th Annual Meeting, 28-31 July 2013, Washington, DC, United States.

Electromagnetic warming applied to organ preservation
Brian Wowk[1] and Ariadna Corral[2]

[1]21st Century Medicine, Inc., Fontana, California 92336, U.S.A.
[2]CryoBioTech, Departamento de Física Aplicada III, Universidad de Sevilla, Camino de los Descubrimientos s/n, 41092 Sevilla.

Talk
Advances in Low Temperature Biology, Society for Low Temperature Biology Conference 2013, 6-9 October 2013, Hannover, Germany.

Publications in journals.

Assessment of the cryoprotectant concentration inside a bulky organ for cryopreservation using X-ray computed tomography.

Ariadna Corral[1*], Marcin Balcerzyk[2*], Ángel Parrado-Gallego[2], Isabel Fernández-Gómez[2], David R. Lamprea[1,3], Alberto Olmo[1], Ramón Risco[1,4].

[1]Departamento de Física Aplicada III, Universidad de Sevilla, Camino de los Descubrimientos s/n, 41092 Sevilla, Spain.
[2]National Acelerators´ Center (Universidad de Sevilla – CSIC – Junta de Andalucía), Avenida Tomas Alva Edison 7, 41092 Sevilla, Spain.
[3]Insitut für Theoretische Physik, Universität Münster, Wilhelm-Klemm-Straße 9, D-48149 Münster, Germany.

Status: submitted to Cryobiology.

Use of X-Ray Computed Tomography for detection of ice formation applied to organ cryopreservation.

Ariadna Corral[1*], Marcin Balcerzyk[2*], Reyes López[1], Ángel Parrado-Gallego[2], Isabel Fernández-Gómez[2], Ramón Risco[1,3].

[1]Departamento de Física Aplicada III, Universidad de Sevilla, Camino de los Descubrimientos s/n, 41092 Sevilla, Spain.
[2]National Acelerators´ Center (Universidad de Sevilla – CSIC – Junta de Andalucía), Avenida Tomas Alva Edison 7, 41092 Sevilla, Spain.

Status: under preparation.

Patents.

Monitorización mediante TAC de procesos de preservación en frío y criopreservación de material biológico.

Oficina Española de Patentes y Marcas (Spanish Office of Patents and Designs) Número de Solicitud / Request Reference Number: P201300685, 18th July 2013.

Status: Patent pending.